

University of Crete  
Department of Physics



# Intense ultrashort TeraHertz pulses: Development and applications

by  
Jean-Michel Manceau

Thesis  
For the degree of Philosophical Doctorate in Physics

Heraklion, Greece  
October 2010





## Acknowledgments

I would like to acknowledge various people that have contributed to this work.

First, all my gratitude goes to my supervisor Stelios Tzortzakis. Without his determination and intransigence concerning the working method, none of this work would have been possible. Besides being a highly demanding supervisor, he has not forgotten to be a friendly and caring supervisor. I am glad and I feel privileged to have learnt my profession next to him. Thank you very much Stelio!

I am grateful to the two Michalis. M. Galanakis, whose talent with electronic and automation has constantly amazed me. His contribution to the good continuity of this work is invaluable. M. Loulakis who managed even through the critical time to provide us a laser chain running at its optimum. Both of them have also been witnesses of my dark working moods and quasi 100% of the time managed to get me out of them. Thanks a lot pedia!!

I also want to address many thanks to Maria Massaouti and Takis Loukakos. They have been my closest experimental collaborators. Thanks to their input, we have obtained plenty of interesting results. They have taught me a rigorous approach of experimental physics through which I gained maturity and confidence towards my work. Merci pedia ☺.

I would like to thank my colleagues D. Papazoglou, D. Abdollahpour, P. Panagiotopoulos, S. Suntsov and M. Bellec. Thanks to the weekly group meeting, we have been able to exchange a lot on our respective subject of research. They have all brought a lively interest in my work and they have answered many, many of my stupid questions. Thanks a lot guys!!! Many thanks also to D. Adamidou who organized the most impressive conference I have attended so far (COFIL 2010).

We had also many collaborators out of the united UNIS team. The group of Art conservation, with C. Fotakis, A. Nevin and K. Melessanaki, whose contribution has been determinant to give a good start to this thesis. I also want to thank C. Soukoulis, M. Kafesaki, N.H. Shen, N. Katsarakis and G. Kenanakis from the metamaterial group. We have developed a productive collaboration that led to very nice results. I also acknowledge the access to their FTIR spectrometer that allowed a lot of instructive measurements.

I want to thank all the people in the different laser labs (upstairs and downstairs) for their sympathy. Many, many thanks to R. Karali, L. Papadopoulou, M. Sfakianakis for the help with the administrative issues. I also want to thank the A Team of kyrie Michalis at the ground floor for all the

various metal pieces built along this thesis. Many thanks also to R. El Borgini for the various 3D designs and his will to teach me some Cretan expressions.

I was expecting while coming to the southern point of Europe to meet a lot of crazy people. Well, I was right! I am delighted that many of them have become very good friends of mine. Pedia, we had a lovely time on the beloved Crete and next to you I learned to enjoy simple moments of life. You have been a wonderful company and I thank you all.

Finally, all my love and thoughts goes to Kasia, my parents and my brother. Thanks for your support and love all way long.

## Table of contents

<b>CHAPTER I: INTRODUCTION .....</b>	<b>10</b>
<b>I.1/ Overview of terahertz science .....</b>	<b>12</b>
I.1.1 Definition and properties of THz radiation .....	12
I.1.2 Historical overview of THz sources.....	13
<b>I.2/ Principles of coherent THz pulse emission.....</b>	<b>15</b>
I.2.1 Emission from photoconductive antennas .....	15
I.2.2 Emission from optical rectification in nonlinear media .....	17
<b>I.3/ Principles of THz pulse detection.....</b>	<b>20</b>
I.3.1 Incoherent detection.....	20
a) Bolometer .....	20
b) Pyroelectric detector .....	21
c) Heterodyne detector .....	22
I.3.2 Coherent detection of THz pulses .....	23
a) Photoconductive sampling technique.....	23
b) Electro-optic sampling technique.....	23
<b>I.4/ THz Time Domain Spectroscopy .....</b>	<b>26</b>
I.4.1 Principles .....	26
I.4.2 Data Analysis.....	28
<b>I.5/ State of the art in table-top THz pulsed system.....</b>	<b>31</b>
I.5.1 Ultra broadband sources for spectroscopic applications.....	31
I.5.2 Technological developments for THz imaging applications .....	32
I.5.3 High peak power sources for non-linear applications .....	32
<b>I.6/ Thesis outline.....</b>	<b>34</b>
References .....	35
<b>CHAPTER II: GENERATION OF INTENSE BROADBAND THZ PULSES FROM FILAMENT IN AIR .....</b>	<b>38</b>
<b>II.1/ Introduction to the filamentation process.....</b>	<b>40</b>
II.1.1 Properties of ultrashort pulse nonlinear propagation.....	41
II.1.2 Properties of light filaments .....	46
<b>II.2/ THz Emission from filament in air.....</b>	<b>48</b>
II.2.1. THz emission from single color filament.....	48
a) Radial and conical emissions .....	48
b) On-axis emission.....	50
II.2.2. THz emission from two color filament.....	55
a) The genesis of a controversy .....	55
b) Coherent control of THz pulses polarization .....	57
II.2.3 Characterization of the source.....	60

a) Bandwidth .....	60
b) Beam size .....	61
c) Electric field strength .....	62
d) Angular diagram of emission.....	63
<b>II.3/ Chapter conclusions .....</b>	<b>64</b>
References .....	65
<b>CHAPTER III: OPTIMIZATION OF THZ PULSE EMISSION VIA FILAMENTATION TAILORING.....</b>	<b>68</b>
<b>III.1/ Introduction to filamentation tailoring .....</b>	<b>70</b>
<b>III.2/ THz pulse shortening from tailored fs filaments in air .....</b>	<b>71</b>
III.2.1 A Tailoring approach for the electron density control.....	71
III.2.2 The effect on the THz pulse emission.....	73
III.2.3 Measurement of the electron density.....	74
<b>III.3/ Strong terahertz emission enhancement via filament concatenation in air .....</b>	<b>77</b>
III.3.1 Extension of the plasma length using the concatenation effect .....	77
III.3.2 The effect on the THz pulse emission.....	79
III.3.3 A cross correlation effect.....	80
<b>III.4/ Terahertz polarization state control from tailored femtosecond filaments in air .....</b>	<b>82</b>
III.4.1 Effect of an extended plasma length on the THz polarization control .....	82
III.4.2 A Tailoring approach to circumvent the phase walk-off.....	83
III.4.3 Effect of an extended plasma length on the THz polarization state.....	86
<b>III.5/ Chapter conclusions .....</b>	<b>87</b>
References .....	89
<b>CHAPTER IV: TIME DOMAIN SPECTROSCOPY FOR THE ANALYSIS OF CULTURAL HERITAGE RELATED MATERIALS.....</b>	<b>91</b>
<b>IV.1/ Introduction to cultural heritage studies.....</b>	<b>93</b>
<b>IV.2/ Qualitative and quantitative analysis in transmission mode .....</b>	<b>94</b>
IV.2.1 Experimental approach and samples preparation .....	94
IV.2.2 Experimental results.....	96
<b>IV.3 / Analysis in reflection mode and imaging .....</b>	<b>98</b>
IV.3.1 Reflection mode.....	98
IV.3.2 Imaging.....	100
<b>IV.4/ Chapter conclusions.....</b>	<b>102</b>
References .....	103
<b>CHAPTER V: TIME DOMAIN SPECTROSCOPY FOR DYNAMICAL STUDIES OF METAMATERIAL.....</b>	<b>104</b>

<b>V.1/ Introduction to metamaterial science .....</b>	<b>106</b>
V.1.1 Historical overview.....	106
V.1.2 Negative $\epsilon$ and $\mu$ .....	107
a) Negative $\epsilon$ .....	107
b) Negative $\mu$ .....	108
<b>V.2/ Split Ring Resonator (SRR) all-optical switch.....</b>	<b>110</b>
V.2.1 SRR electrical response characterization.....	110
V.2.2 Dynamical control of the electrical response .....	112
a) SRR switch.....	112
b) Frequency shift and broadband phase plate.....	113
c) Simulations.....	114
<b>V.3/ Mode shifting.....</b>	<b>117</b>
V.3.1 eSRR design and fabrication .....	117
V.3.2 Experimental results.....	118
V.3.3 Simulations .....	119
<b>V.4/ Chapter conclusions .....</b>	<b>121</b>
References .....	122
<b>CHAPTER VI: APPLICATIONS OF AN INTENSE THZ SOURCE FOR THZ NONLINEAR OPTICS .....</b>	<b>124</b>
<b>VI.1/ Introduction.....</b>	<b>126</b>
<b>VI.2/ Excitation of phonons in semiconductors.....</b>	<b>127</b>
VI.2.1 Traditional approach for phonon excitation.....	127
VI.2.2 Coherent phonon excitation with THz radiation.....	129
a) Experimental approach and sample characterization.....	129
b) Coherent phonon .....	130
c) THz coupling to the semiconductor lattice.....	131
VI.2.2 Lattice deformation and incoherent phonon excitation .....	132
a) Lattice deformation .....	132
b) Incoherent phonon.....	134
<b>VI.3/ Nonlinearities in electro-optic crystal .....</b>	<b>136</b>
VI.3.1 Phonons generation .....	136
VI.3.2 THz pulse self-phase modulation .....	137
VI.3.3 Electro-optic distortions.....	139
<b>VI.4/ Scaling up the THz pulse energy .....</b>	<b>140</b>
<b>VI.5/ Chapter conclusions.....</b>	<b>143</b>
References .....	144
<b>CONCLUSIONS AND PERSPECTIVES.....</b>	<b>148</b>
<b>Conclusions.....</b>	<b>148</b>

<b>Perspectives .....</b>	<b>149</b>
references .....	151
<b>List of relevant publications.....</b>	<b>153</b>
<b>List of conferences.....</b>	<b>153</b>

## *Chapter I: Introduction*

<b>CHAPTER I: INTRODUCTION</b> .....	<b>10</b>
<b>I.1/ Overview of terahertz science</b> .....	<b>12</b>
I.1.1 Definition and properties of THz radiation .....	12
I.1.2 Historical overview of THz sources.....	13
<b>I.2/ Principles of coherent THz pulse emission</b> .....	<b>15</b>
I.2.1 Emission from photoconductive antennas .....	15
I.2.2 Emission from optical rectification in nonlinear media .....	17
<b>I.3/ Principles of THz pulse detection</b> .....	<b>20</b>
I.3.1 Incoherent detection.....	20
a) Bolometer .....	20
b) Pyroelectric detector .....	21
c) Heterodyne detector .....	22
I.3.2 Coherent detection of THz pulses .....	23
a) Photoconductive sampling technique.....	23
b) Electro-optic sampling technique.....	23
<b>I.4/ THz Time Domain Spectroscopy</b> .....	<b>26</b>
I.4.1 Principles .....	26
I.4.2 Data Analysis.....	28
<b>I.5/ State of the art in table-top THz pulsed system</b> .....	<b>31</b>
I.5.1 Ultra broadband sources for spectroscopic applications.....	31
I.5.2 Technological developments for THz imaging applications .....	32
I.5.3 High peak power sources for non-linear applications .....	32
<b>I.6/ Thesis outline</b> .....	<b>34</b>
References .....	35

# I.1/ Overview of terahertz science

## I.1.1 Definition and properties of THz radiation

Terahertz (THz) radiation is the electromagnetic radiation lying in a frequency interval from 0.1 to 30 THz. These frequencies correspond to a wavelength range from 3 mm to 10  $\mu\text{m}$  wavelength, a photon energy from 0.4 meV to 120 meV, or to an equivalent black body radiation with temperatures between 4 K to 1 200 K. Historically, THz technologies were used mainly within the astronomy community for studying the background of cosmic far-infrared radiation and by the laser-fusion community for the diagnostics of plasmas. Despite the interests brought by these communities, the THz band has remained one of the most untapped and least understood regions of the electromagnetic spectrum, compared to the relatively well developed science and technology in the microwave and optical frequencies. The so called “THz gap” resulted from the limits of the electron velocities which prevent electronic devices to operate above a few hundred GHz, and from thermal energies that limit the smallest electronic transitions useful for lasing, preventing solid-state lasers to operate below a few hundred THz.

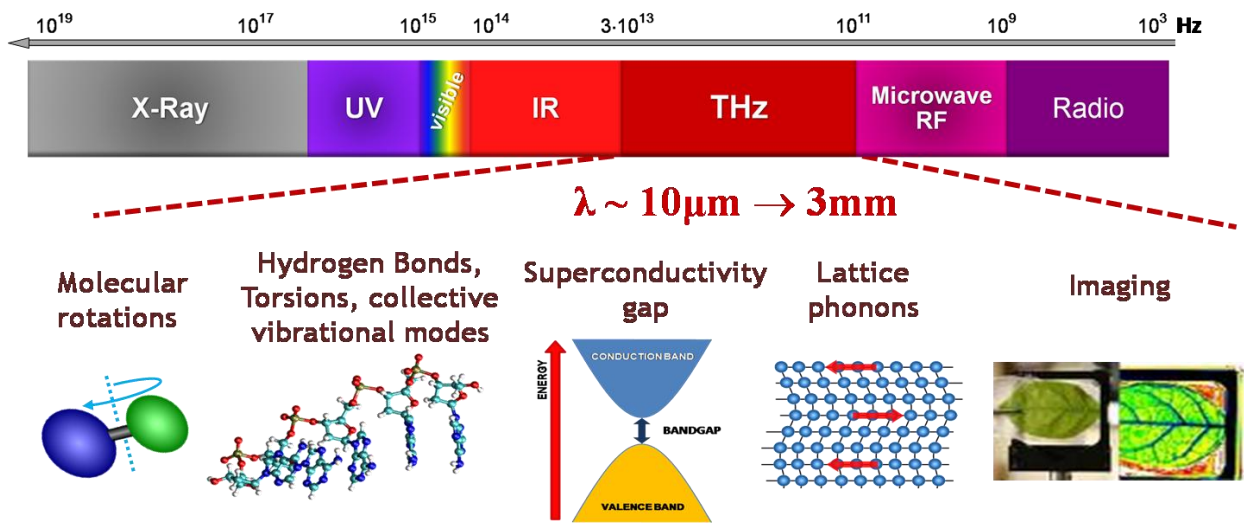


**Figure 1: The electromagnetic spectrum in frequency. The THz region is depicted in dark red and its potential applications and corresponding spectroscopic modes are presented (non-exhaustive list).**

The first demonstration of a coherent emission and detection of broadband THz pulses in the late 1980's allowed to routinely access this part of the EM spectrum [1]. Thus, the unique properties of this radiation have been revealed, suggesting the development of promising applications.

Firstly, THz waves have long wavelengths and thus they are less affected by Mie scattering. As a consequence various materials such as cloth, paper, wood, plastic and dry dielectrics are transparent to THz radiation. Secondly, THz waves have low photon energy which prevents them from

ionizing biological tissues. Furthermore, THz radiation is strongly absorbed by water which prevents it from penetrating the human body. These properties make THz radiation an excellent tool for imaging applications and non destructive screening [2-6]. Many molecules have strong absorption features in this frequency range, due to vibrational and rotational transitions. These transitions are specific to each molecule. Consequently, molecules exhibit fingerprints which allow their spectroscopic identification [7-9]. Furthermore, THz pulses can be detected coherently, by the sampling measurement of their electric field, giving a direct access to the amplitude and the phase of the radiation. These properties make THz radiation an excellent tool for the characterization of the absorption and dispersion of many materials [10-12]. Finally numerous solid state phenomena lie within the THz range. For example the band gaps of superconductors, the phonon modes of most semiconductors and crystals have frequencies in the THz regime [13-15]. Consequently, THz radiation is a promising tool for fundamental studies and deeper understanding of solid state phenomena.

### I.1.2 Historical overview of THz sources

After careful consideration of the existing literature, using the term ‘THz gap’ in order to describe this part of the electromagnetic spectrum is rather excessive. This popular term extensively used in the past decades should be restricted to the lack of coherent sources and technological applications. Heinrich Ruben’s publication on the ‘refraction of rays of great wavelength in rock salt, sylvine and fluorite’ is probably the first significant paper on longer wavelength radiation. In 1900 Rubens, using the reststrahlen spectrometer, obtained very accurate data that enabled Max Planck to write down the equation that is now called Planck’s radiation law. A succinct review of the technological development on Far Infra-Red (FIR) radiation through the last century can be found in [16]. As mentioned in the previous section, for many years THz radiation concerned mainly the astrophysics community. It can easily be understood as results from the NASA Cosmic Background Explorer and examination of the spectral energy distributions in observable galaxies, indicate that approximately half the luminosity of the universe and 98% of the photons released since the Big Bang appear at far-IR and sub-millimeter wavelengths (40 to 500  $\mu\text{m}$ ) [17]. The black body radiation from room temperature objects also lies within the THz range. Given the equivalent temperature, the world is effectively bathed in THz radiation.

All these THz sources are incoherent which considerably limit their use for technological applications. Nevertheless, tremendous efforts have been made in order to fill this gap. A non-exhaustive list of techniques used to generate Terahertz radiation is presented on Figure 2. The research activities in the THz field can be divided in two main categories. The first one is the Continuous Wave (CW) sources that produce narrow band THz radiation. A list of CW techniques is enumerated on the right hand side of Figure 2. A recent review on these techniques can be found in Ref. [18].

In the second category we find the broadband sources. These sources are based on the emission of ultrashort THz pulses. A list of techniques is enumerated on the left hand side of Figure 2. Historically, the most popular approaches in THz pulsed sources are based on photoconductive antennas and optical rectification techniques. They have been used in numerous laboratories around the world. In the following section, we will briefly review their principles in order to introduce the basic requirements needed for the THz time domain spectroscopy. The photonization of air was an emerging field at the beginning of this thesis and a very promising technique as exposed later in this chapter. Surface field emitters and free electron laser are much less popular techniques and they are beyond the scope of this thesis.

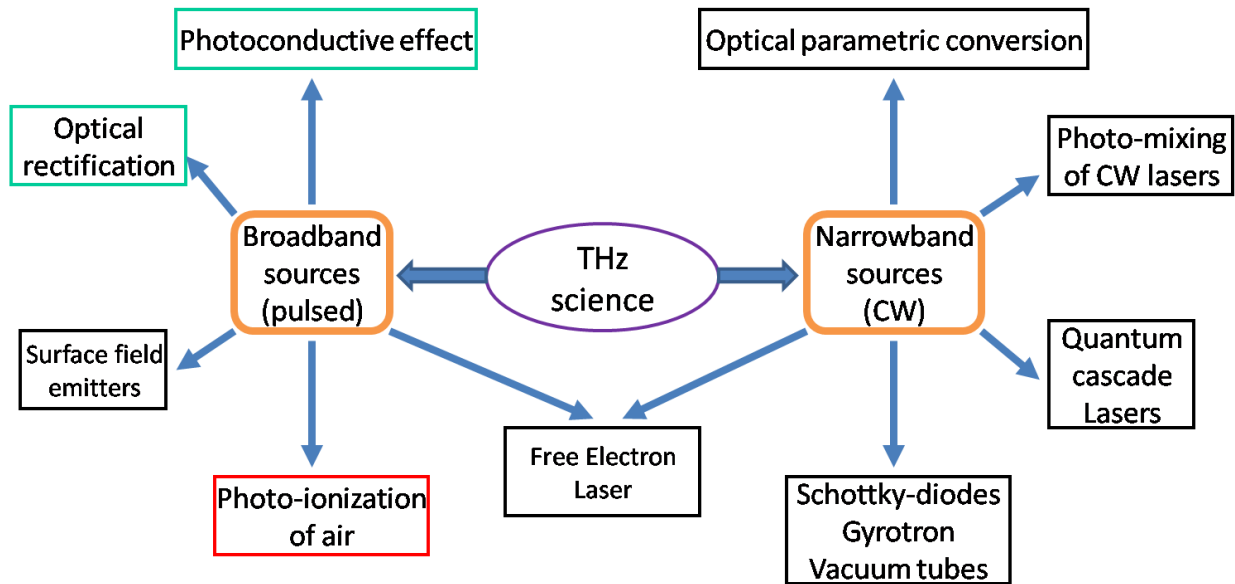
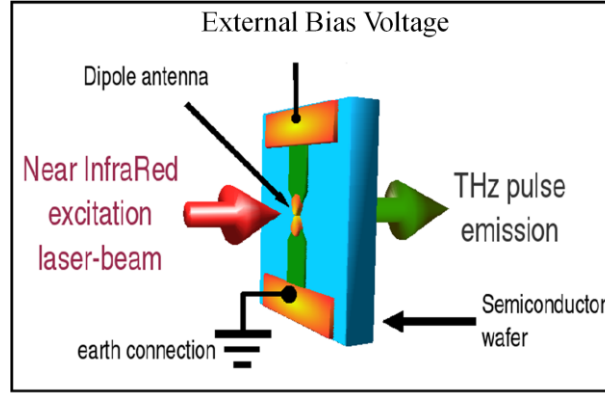


Figure 2: Non-exhaustive list of the different means to produce THz radiation.

## I.2/ Principles of coherent THz pulse emission

### I.2.1 Emission from photoconductive antennas

The photoconductive (PC) antenna is one of the most frequently used components for THz generation as well as detection. It generates and detects THz pulses by transient photocarriers induced with ultrafast laser pulses. Figure 3 illustrates a PC antenna and the concept of operation.



**Figure 3: Schematic representation of THz pulse emission from photoconductive antenna.**

A PC antenna consists of two metal electrodes that are deposited on a semi-insulating semiconductor substrate with a gap between these two electrodes. To generate THz pulses a voltage is applied across the electrodes. Since the substrate is semi-insulating, electric energy is stored in the gap area. Ultrafast laser pulses act like transient switches to open this reservoir of electric energy and release it in the form of THz pulses. Generally, the photon energy of the excitation optical pulse should be higher than the band gap of the substrate. Sometimes, multiphoton absorption could be used, and an excitation laser with lower photon energy can also generate free carriers. Free carriers are then driven by the bias field across the gap and produce a photocurrent. Since electrons usually have much higher mobility than holes, the contribution of holes can be ignored in most cases. The current density is then described as:

$$J(t) = N(t)e\mu E_b$$

where  $N$  is density of photocarriers,  $e$  denotes the elementary charge,  $\mu$  is the mobility of electron, and  $E_b$  is the bias electric field. The photocarrier density  $N$  is a function of time, whose format is determined by the laser pulse shape and the carrier lifetime. Since the photocurrent varies in time, it generates electromagnetic pulse, whose electric field is approximately:

$$E_{THz} = \frac{1}{4\pi\epsilon_0} \frac{A}{c^2 z} \frac{\partial J(t)}{\partial t} = \frac{Ae}{4\pi\epsilon_0 c^2 z} \frac{\partial N(t)}{\partial t} \mu E_b$$

where  $A$  is the area in the gap illuminated by the laser light,  $\epsilon_0$  is the vacuum permittivity,  $c$  is the speed in vacuum, and  $z$  is the distance between the field point and the THz source. To derive the second

equation, the field point is assumed located at normal to the PC antenna and the distance between the field point and the source is much larger than the dimension of the PC antenna. The energy of the THz pulse comes from the electric energy stored across the gap rather than the optical pulse energy. In principle, the pulse energy of THz radiation is not limited by the pulse energy of excitation laser and optical to THz quantum conversion efficiency greater than one is possible. However, the pulse energy of THz radiation has a very immediate relationship with the excitation laser pulse energy. In fact the excitation acts as a trigger to release the stored energy into THz radiation. The more photocarriers being generated, the more stored energy is converted into THz radiation. Under weak excitation condition, pulse energy of the THz wave is proportional to pulse energy of the excitation laser. In reality, linear relationships between the biased field and THz field, as well as between the excitation pulse energy and THz field, is only true under weak excitation and low bias field. When the substrate of the PC antenna is excited, it is no longer a semi-insulating material, but rather a conductive medium. As a result, the induced field screens the biased field, and the photo current is modified:

$$J(t) = \frac{\sigma(t)E_b}{\frac{\sigma(t)\eta_0}{1+n} + 1}$$

where  $\sigma$  is the conductivity of the substrate,  $\eta_0$  denotes the impedance of air, which is  $\eta_0 = 377\Omega$ , and  $n$  is the refractive index of the substrate. The substrate conductivity  $\sigma$  is induced by the excitation laser, and can be considered as  $\sigma \propto I_0$ , where  $I_0$  is the laser intensity. Combining the last two equations gives:

$$E_{THz} \propto \frac{d\sigma(t)}{dt} \frac{1}{\left[1 + \frac{\sigma(t)\eta_0}{1+n}\right]^2} \propto \frac{I_0}{(1 + kI_0)^2}$$

Here  $k = \kappa(t)\eta_0/(1+n)$ , where  $\kappa(t)$  denotes the ratio between  $\sigma(t)$  and  $I_0$ . The above equation clearly shows that when the excitation laser is strong enough, the impedance of the substrate becomes comparable to the air, and the THz field becomes saturating to the excitation laser power. Increasing the bias field also has a limitation, since a high electric field may cause dielectric breakdown in the substrate. Breakdown of a PC antenna in THz wave generation can be grouped into two categories: field induced breakdown and thermal induced breakdown. Field induced breakdown happens when the biased field is higher than the breakdown field of the semiconductor material (i.e.  $4 \times 10^5 \text{V/cm}$  for GaAs). It usually happens instantly with field-induced avalanche. Thermal induced breakdown is caused by heating of the substrate by photocurrent flow in the substrate (as well as photon absorption of the excitation laser). Heating of the substrate reduces its resistance, which leads to even higher current flow. The thermal induced breakdown is a slow process, and usually takes seconds to even minutes.

Performance of a PC antenna depends mainly on the following factors: the substrate material, the geometry of the active area, the geometry of antenna, and the excitation laser pulse. Materials with a short carrier lifetime, such as LT-GaAs or doped silicon, are usually selected as the substrate in order to increase the response speed of the PC antenna. The response speed is essential to generate and detect THz pulses containing high frequency components. Higher carrier mobility is also a desired attribute since it results in the high efficiency of THz wave generation. High dark resistance is required for the substrate in order to have sufficient breakdown voltage across the antenna. The active area of the PC antenna, which is the gap area with laser excitation, is another crucial aspect of a PC antenna, since that is the active area to generate and detect THz waves. Careful design of the field distribution in the gap can increase the breakdown field and allow the PC antenna to generate more intense THz pulses. Distribution of excitation light within the gap is also important. PC antennas with smaller gaps are more sensitive, especially when low excitation power is used. However, larger gaps allow higher excitation power and bias voltage to be applied on the PC antenna, thus generating higher power THz waves. Larger active area can also help to lower the screening effect. Shape of the antenna is crucial to optimize coupling of THz waves between the device and free space. In terms of frequency response, various antennas are divided into two groups: resonant and non-resonant antennas. The former has a resonant frequency, which emits THz waves around a certain central-frequency. The dipole-antenna is the most widely used resonant antenna, which emits THz waves with a central wavelength of  $\lambda_n = 2L/m$ . Here  $\lambda_n$  is wavelength in the substrate, and the response wavelength in the free space is  $\lambda = \lambda_n \times n$ , where  $n$  is refractive index of the substrate.  $L$  denotes the width of the antenna from one side of the anode to the other side of the cathode and  $m$  can be any positive integer. A non resonant antenna has a variable width, and leads to a broader frequency response range. Geometries of a non resonant antenna include bowtie, spiral, and logarithmic periodic antennas. Optics, such as hyper-hemispherical silicon lens is very often used to enhance the coupling efficiency.

### I.2.2 Emission from optical rectification in nonlinear media

Optical rectification is a second-order nonlinear optical effect. It is basically a difference-frequency generation with the frequency difference close to zero. Typically, femtosecond laser pulses are used to generate THz from Electro-Optic (EO) crystals via optical rectification. Because a femtosecond pulse is a broadband pulse (many frequency components), any two frequency components contribute to the difference-frequency generation, and the overall result is the weighted sum of all the contributions. One femtosecond laser pulse is enough to stimulate optical rectification radiation, which makes the experiment very simple (see Figure 4). Mathematically, the polarization  $P$  can be expanded into a power series of the electric field  $E$ :

$$P(\mathbf{r}, t) = (\chi)^1(\mathbf{r}, t)\mathbf{E}(\mathbf{r}, t) + (\chi)^2(\mathbf{r}, t):\mathbf{E}(\mathbf{r}, t)\mathbf{E}(\mathbf{r}, t) + (\chi)^3(\mathbf{r}, t):\mathbf{E}(\mathbf{r}, t)\mathbf{E}(\mathbf{r}, t)\mathbf{E}(\mathbf{r}, t)+\dots$$

Where  $\chi^{(n)}$  ( $\mathbf{r}, t$ ) is the  $n$ th-order nonlinear susceptibility tensor. Optical rectification comes from the second term of the above equation. If the incident light is plane wave, then  $\mathbf{E}$  can be expressed as:

$$\mathbf{E}(t) = \int_0^{+\infty} E(\omega) \exp(-i\omega t) d\omega + c. c \dots$$

By substituting the first equation into the second, the polarization for optical rectification is given by:

$$\begin{aligned} \mathbf{P}_{OR}^{(2)}(t) &= 2\chi^{(2)}: \int_0^{\infty} \int_0^{\infty} \mathbf{E}(\omega_1)\mathbf{E}^*(\omega_2)\exp[-i(\omega_1 - \omega_2)t] d\omega_1 d\omega_2, \\ &= 2\chi^{(2)}: \int_0^{\infty} \int_0^{\infty} \mathbf{E}(\omega + \Omega)\mathbf{E}^*(\omega)\exp[-i\Omega t] d\Omega d\omega, \end{aligned}$$

where  $\Omega$  is the frequency difference of two optical frequency components. In the far field, the radiated electric field  $E_r(t)$  is proportional to the second derivative of  $\mathbf{P}_{OR}^{(2)}(t)$  with respect to time  $t$ :

$$E_r(t) \propto \frac{\partial^2}{\partial t^2} \mathbf{P}_{OR}^{(2)}(t).$$

The susceptibility tensor  $\chi^{(2)}$  depends on the crystal structure. Given a crystal structure and incident light, the above equation can be used to calculate the far-field waveform of the radiation. Many factors, such as materials, crystal orientation, thickness, absorption and dispersion, diffraction, phase matching, and saturation, affect the radiation efficiency, waveform, and frequency distribution. Phase matching is the most important factor for a nonlinear process such as THz generation from optical rectification. Only when phase matching is satisfied, all three waves participating in the optical rectification process can keep in phase and lead to maximum energy conversion along the light propagation. Phase mismatch leads to a phase walk off while propagating. The coherence length is defined by the interaction length when the phase change reaches  $\pi$ :

$$\delta k L_c = \pi.$$

Where  $\delta k = k_{01} - k_{02} - k_{THz}$ . To generate THz efficiently from a bulk crystal, the thickness of the crystal cannot be selected longer than the coherence length in order to avoid conversion cancellation due to phase mismatch. This means phase matching is satisfied in THz wave generation when the group velocity of the optical beam equals phase velocity of the THz beam. Since the optical pulse has a much higher frequency than the THz pulse, the THz pulse only sees the profile of the optical pulse rather than the oscillations. To have maximum energy conversion, the optical pulse should have a constant temporal delay according to the THz pulse along the entire interaction length.

According to the excitation wavelength and properties of the nonlinear material, optical rectification can happen under three different conditions. If the photo energy of the excitation beam is

higher than the band gap of the nonlinear material, the optical beam will be absorbed within a fairly short distance. In this case, usually phase matching is not very important, since the interaction range is much shorter than the coherence length. Even with a short absorption distance, there is typically strong THz generation due to a resonating enhanced nonlinear process. When the photon energy is less than the band gap of the nonlinear material, the excitation laser is able to propagate through the nonlinear crystal for a long distance. THz generation is also different with different phase matching conditions. If phase matching is satisfied in optical rectification, the generated THz field will continually increase along the entire length of the nonlinear crystal. Therefore, strong THz wave generation is expected. If phase matching is not satisfied, generated THz waves will be canceled after each coherence length and THz radiation efficiency will be low. Only THz waves generated within a very short range close to both surfaces of the nonlinear crystal may not have been fully canceled due to velocity mismatch between the optical and THz pulse. In this case, two THz pulses with reverse polarity may be observed. When selecting nonlinear crystals for THz wave generation, three major factors need to be considered: nonlinearity of the material, absorption of both optical and THz waves in the material, and the coherence length of the optical rectification process. For instance, ZnTe crystals satisfy the previous criteria and are one of the most favorable to generate THz waves excited by fs laser pulses with central wavelength around 800 nm. To obtain maximum conversion efficiency from pump light to THz radiation, it is important to select proper crystal cutting and orientation. ZnTe is a zinc blende crystal, and the only nonzero tensor elements are  $\chi_{14} = \chi_{25} = \chi_{36}$ . When only normal incidence is considered, the THz field generated from a (110) orientation crystal is:

$$|E_{\text{THz}}| \propto d_{14}E^2[\sin^2\theta(1 + 3\cos^2\theta)]^{1/2} \text{ with } \Phi = \arctan(2 \cos \theta).$$

Here  $\theta$  denotes the angle between laser polarization and the reference axis in the crystal, and  $\Phi$  is the angle between THz wave polarization and the reference axis.

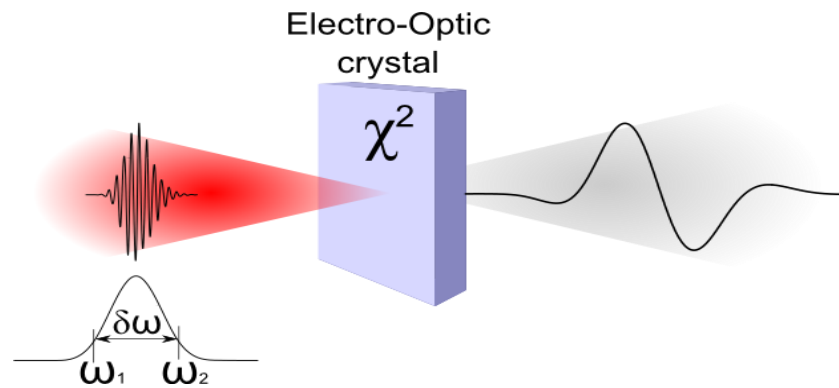


**Figure 4: Schematic representation of optical rectification technique.**

## I.3/ Principles of THz pulse detection

### I.3.1 Incoherent detection

#### a) Bolometer

A bolometer is a device that measures the energy of an incident electromagnetic radiation. It consists of an absorptive element (e.g. a thin layer of metal) connected to a heat sink (a body of constant temperature) via a thermal link. Hence, any radiation incident on the absorptive element raises its temperature above that of the heat sink. The temperature change can be then measured directly or via an attached thermometer. In the case when the absorber and the thermometer are joined in the same material, a polarized current  $I_p$  goes through the absorber, generating a polarized tension  $V_p$ . Thus, when a radiation is absorbed, the resistance of the absorber is modified, implying a proportional change in the tension  $V_p$  (see Figure 5 ).This change is then amplified and measured.

Today, most bolometers use semiconductor or superconductor absorptive elements rather than metals. Potentially, bolometers can be used to measure radiation energy of any frequency. Nevertheless, for most wavelength ranges there are other methods of detection that are more sensitive. For THz wavelengths, bolometers are the most sensitive detectors and have therefore been widely used in the astronomy field. To achieve the best sensitivity, they must be cooled down to a fraction of a degree above absolute zero (typically from 50 mK to 300 mK). Bolometers are directly sensitive to the energy left inside the absorber. For this reason they can be used not only for ionizing particles and photons, but also for non-ionizing particles, any sort of radiation, and even to search for unknown forms of mass or energy (like dark matter). This lack of discrimination can also represent a serious drawback. Bolometers are very slow to respond and slow to reset (i.e., return to thermal equilibrium with the environment). Furthermore, they are bulky and quite difficult to manipulate since, they need cryogenic cooling. Consequently, bolometers have not been chosen to be our detection approach.

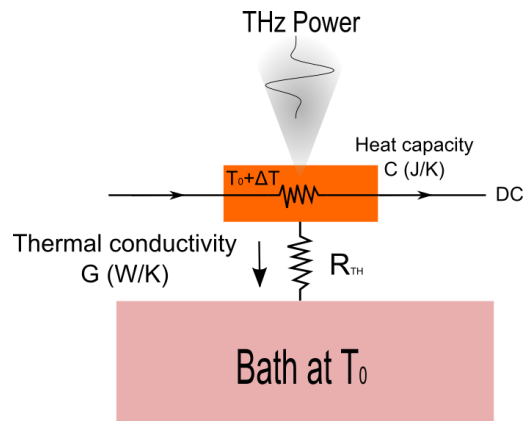
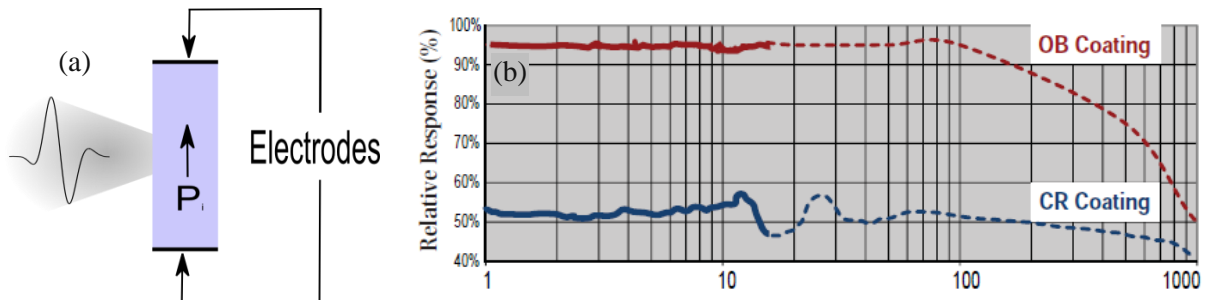


Figure 5: Schematic representation of a bolometric measurement.

### b) Pyroelectric detector

The pyroelectricity is the ability of certain anisotropic materials to generate an electrical voltage when they are heated or cooled. Pyroelectricity can be seen as one of the side of a triangle with three vertices representing the three types of energy present in the material: mechanical energy, thermal energy and electrical energy. The side connecting the thermal and electric energies represents the pyroelectric effect. The side connecting the electrical and mechanical energies represents the piezoelectric effect. Finally, the side linking mechanical and thermal energies represents the thermo-electric effect of Peltier, Seebeck and Thomson. Below a temperature  $T_c$  known as the Curie point, ferroelectric materials such as Lithium Tantalate, exhibit a large spontaneous electrical polarization. If the temperature of such a material is altered, for example by incident radiation, its polarization is then changed. This change in polarization may be observed as an electrical signal if electrodes are placed on opposite faces of a thin slice of the material to form a capacitor. The sensor will only produce an electrical output signal when the temperature changes; that is, when the level of incident radiation changes. This process is independent of the wavelength of the incident radiation and hence pyroelectric sensors have a flat response over a very wide spectral range.

Nowadays, pyroelectric detectors in the THz region can easily be found on the market. They are compact, with a relatively low cost and their responsivity is undergoing constant improvement [19]. During my thesis, we have used a pyroelectric detector based on a Lithium Tantalate ( $\text{LiTaO}_3$ ) crystal of  $2 \text{ mm}^2$  surface. The relative spectral response of our detector, which is flat from 30 to 3 THz and dropping for longer wavelengths, is presented on Figure 6. The measured signal has to be chopped at low frequency (around 10 Hz) and can be directly read on an oscilloscope. The energy of the measured THz pulse can be then extracted considering the calibration factor ( $1.46 \times 10^5 \text{ V/W}$ ) and the number of measured pulses per second. Nevertheless, precautions must be taken into the claimed values of THz pulse energy, since pyroelectric detectors are very often uncalibrated at low frequencies (0.1 to 3THz) [20].



**Figure 6: (a) Schematic representation of a pyroelectric detector. (b) Relative spectral response of our pyroelectric detector.**

c) Heterodyne detector

The heterodyne detection is a method of detecting radiation by non-linear mixing with radiation of a reference frequency. It is commonly used in telecommunications and astronomy for detecting and analyzing signals. The radiation in question is most commonly either radio waves or light. The reference radiation is known as the local oscillator. The signal and the local oscillator are superimposed in a mixer. The mixer, which is commonly a (photo-)diode, has a non-linear response to the amplitude, that is, at least part of the output is proportional to the square of the input.

Let the electric field of the received signal be:

$$E_{sig} \cos(\omega_{sig}t + \varphi)$$

and that of the local oscillator be:

$$E_{LO} \cos(\omega_{LO}t)$$

For simplicity, assume that the output  $I$  of the detector is proportional to the square of the amplitude:

$$I \propto (E_{sig} \cos(\omega_{sig}t + \varphi) + E_{LO} \cos(\omega_{LO}t))^2$$

The development of the above equation gives an output which has high frequency ( $2\omega_{sig}$  and  $2\omega_{LO}$ ) components, a beating component ( $\omega_{sig}-\omega_{LO}$ ), as well as constant components. In heterodyne detection, the high frequency components and usually the constant components are filtered out, leaving the intermediate (beat) frequency which is then measured with a Schottky diode. Such diode has a very low direct threshold voltage and a very short switching time. This allows the detection of GHz signal. The amplitude of the measured beating component is proportional to the amplitude of the signal radiation.

During this thesis, we have used a customized heterodyne detector operating at a frequency of 440 GHz. A detailed schematic of the detector is presented on Figure 7. A review on THz heterodyne detection and its various applications can be found in [21].

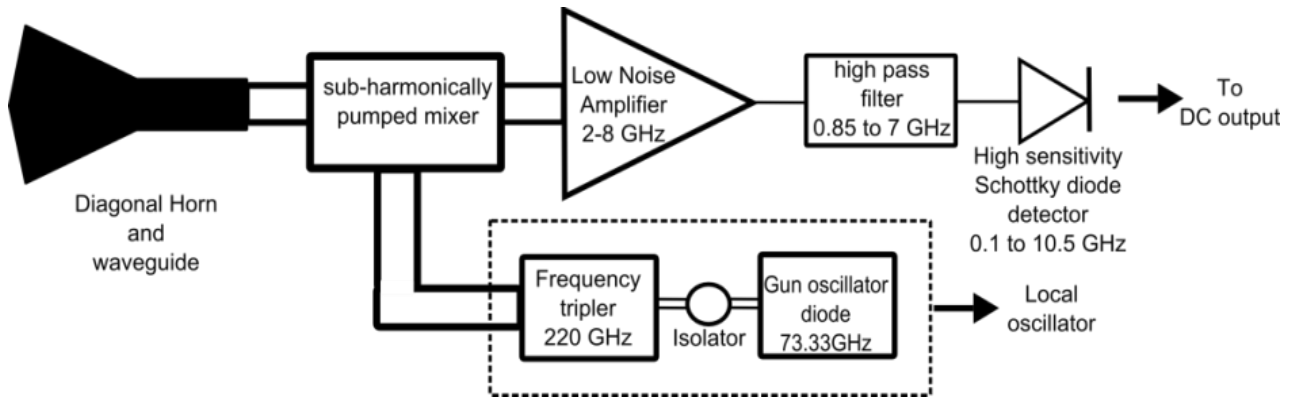


**Figure 7: Schematic representation of our heterodyne detector at 0.44 THz.**

## I.3.2 Coherent detection of THz pulses

### a) Photoconductive sampling technique

Using a PC antenna as a THz detector is quite similar to use it as a THz emitter. The only major difference is that as a detector, its two electrodes are connected to a current sensor rather than a power supply. By controlling the time delay between the THz pulse and the optical probe pulse, the electric field across the strip line of the PC antenna at any given point in time can be sampled by the optical probe pulse which serves to generate transient photocarriers in the substrate at that specific time. Since the THz pulses and laser pulses remain for a certain time delay, the photoinduced carriers see a steady electric field, and are driven by this field to form a current between the two electrodes. The THz field induced current is:

$$\bar{J} = \bar{N}e\mu E(\tau)$$

Here  $\bar{N}$  denotes the average electron density, and  $\tau$  is the temporal delay between probe pulse and the THz pulse. By scanning the temporal delay, the THz pulse waveform as a function of  $\tau$  is recorded. Typically the period of the THz oscillation is about 1 picosecond (ps), and the THz pulses are a sub cycle to a few cycles of oscillation. As shown in the above equation, the detection of THz pulses directly records its field rather than its intensity. The measurement records not only amplitude, but also phase information of the THz pulse, which gives access to various parameters as we will see later in this chapter.

### b) Electro-optic sampling technique

As in the photoconductive sampling technique, electro-optic sampling is also a pump-probe technique. Coming from the same source, the pump and probe pulses have a defined temporal relationship. Propagating along an optical delay line, the probe pulse samples the THz pulse and records its electric field as a function of the time delay. More specifically, electro-optic (EO) sampling can be considered as a reciprocal process of the optical rectification. In EO sampling, the THz field is measured by modulating a probe beam inside an EO crystal, where it changes the polarization ellipsoid of the refractive index of the EO crystal. The linearly polarized probe beam co-propagates inside the crystal with the THz beam (pump), and its phase is modulated by the refractive index change induced by the electric field of the THz pulse. The existence of the THz field changes the birefringence of the EO crystal, i.e. causing the refractive index difference for polarizations along different axes of the crystal. This polarization change is converted to intensity change by an analyzer, for example a Wollaston prism. Usually a pair of balanced photodiodes is used to suppress the common laser noise while the signal is

doubled. For a zinc blade crystal, such as ZnTe, when an electric field is applied, its ellipsoid of the refractive index is:

$$\frac{x^2 + y^2 + z^2}{n_0^2} + 2\gamma_{41}E_x yz + 2\gamma_{41}E_y zx + 2\gamma_{41}E_z xy = 1 ,$$

where  $n_0$  is refractive index of the crystal without electric field,  $x, y, z$  are coordinate units of the ellipsoid, and  $E_x, E_y, E_z$  are applied electric field along corresponding axes, respectively.  $\gamma_{41}$  is EO coefficient of the crystal. A phase delay  $\Gamma$  can be calculated according to change of the refractive index:

$$\Gamma = \frac{2\pi d}{\lambda} \Delta n_0 ,$$

where  $n_0$  is refractive index of the crystal without electric field,  $x, y, z$  are coordinate units of the ellipsoid, and  $E_x, E_y, E_z$  are applied electric field along corresponding axes, respectively.  $\gamma_{41}$  is the EO coefficient of the crystal. A phase delay  $\Gamma$  can be calculated according to the change of the refractive index:

$$\Gamma = \frac{\pi d n_0^3 \gamma_{41} E}{\lambda} \sqrt{1 + 3\sin^2 \Phi} .$$

There exits two common methods to measure phase delay of the probe laser beam. They are cross and balanced measurements. The latter one gives higher signal and directly measures the field of the THz field, while the former method is simpler in experimental setup. Figure 8 shows the concept of balanced measurement. A linearly polarized probe beam is modified to elliptical polarization through the EO process. A quarter-wave plate is used to bias the polarization of the probe beam, which can be put either in front of or after the EO crystal. An analyzer is used to split the biased probe beam into s and p polarization components. A pair of balanced photo detectors is used to measure the difference in the s and p polarization components. When no THz field is applied, s and p polarization components will have the same intensity after the analyzer; therefore, the balanced detector gives no signal. The presence of a THz electric field changes the polarization of the probe beam, generating a measurable signal in the balance detector. The signal of the balanced detector is:

$$S = I_0 \sin 2\Phi \sin \Gamma ,$$

where  $I_0$  is the intensity of the probe laser and  $\Phi$  is the angle between the probe beam polarization and the long axis of the ellipsoid induced by the THz field. The above equation indicates that, in a balanced measurement, the signal is linearly proportional to the electric field of the THz radiation under relatively low electric field values. At higher level of electric field, the linear proportionality does not hold anymore, as we will see in the last chapter of this thesis. A cross measurement is similar to balanced measurement except there is no quarter-wave-plate. The analyzer is set cross-polarized to the polarizer located before the EO crystal. Probe beam leaking through the analyzer is detected using a single optical detector. Without THz field, in principle, probe beam does not leak through the analyzer and the recorded

signal is 0. If a THz field is applied to modify the polarization of the probe beam, the leaked signal will become larger.

It is worth noticing that the above discussion on EO sampling is based on the steady electric field assumption. For a transient electric field such as a THz pulse, phase matching should be considered. Being the reciprocal process of optical rectification, EO sampling shares the same phase-matching condition. Two main factors limit the bandwidth of THz radiation in optical rectification and EO sampling: the pulse duration of the excitation laser pulse and phase matching conditions. Another factor that may not be as important as the previous two, but also limits the useful spectrum is Longitudinal Optical (LO) phonon absorption; it burns holes in the broad spectrum.

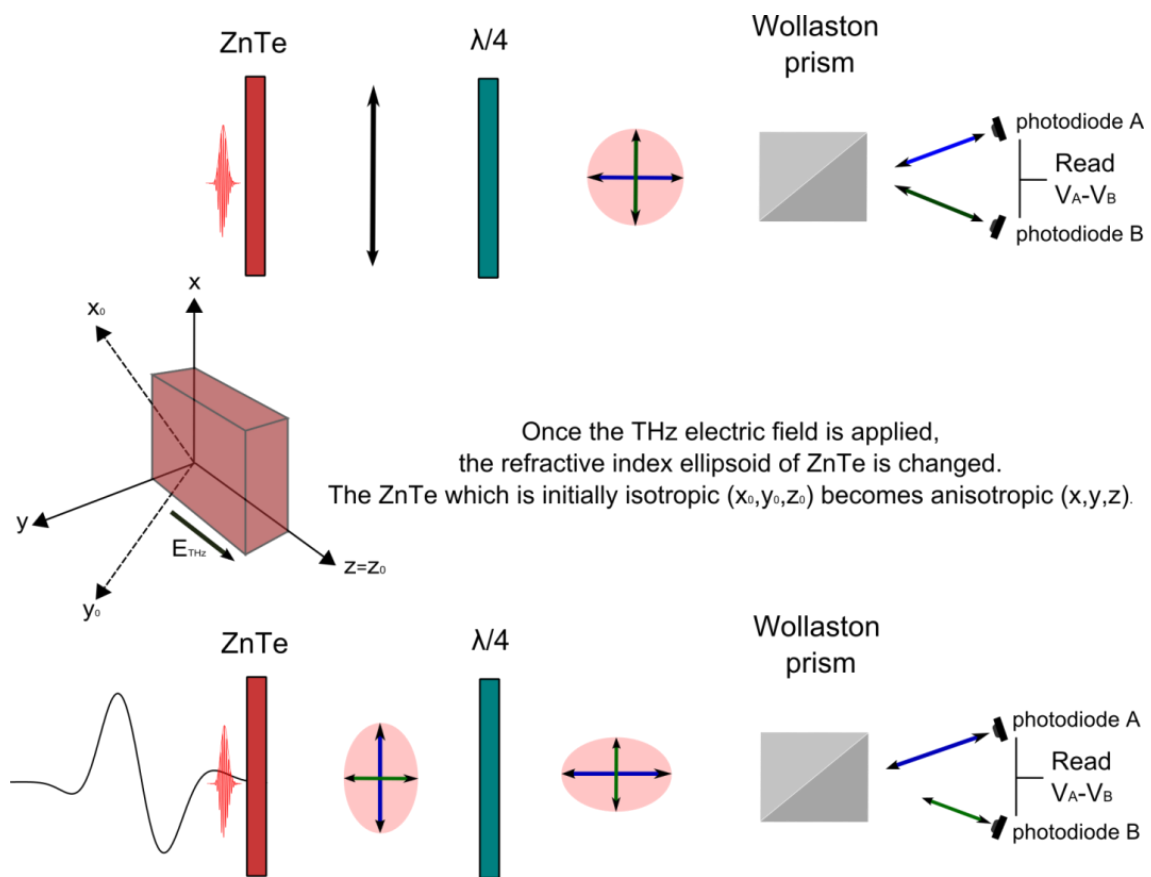


**Figure 8: Schematic representation of a balanced electro-optic set-up.**

## I.4/ THz Time Domain Spectroscopy

### I.4.1 Principles

In the previous paragraph, the classic approaches to emit and measure coherent THz pulses have been introduced. In the following, are presented the basic requirements in order to build a THz time domain spectrometer. The spectrometer is based on a pump-probe technique, which means that an initial laser pulse is separated in two arms. Using a dielectric beam splitter (R10%; T90%), we separate the laser into a pump beam containing most of the energy and a weaker probe beam which will be used to measure the emitted THz pulses. Once the THz pulses are emitted (e.g. from a 0.5mm thick [110] ZnTe crystal), a set of 4 parabolic mirrors is used to collect, collimate, focus and bring the THz beam to the detection crystal as depicted in figure 9(a). A high resistivity silicon wafer ( $10^4\Omega\cdot\text{cm}^{-1}$ ) (0.5 mm thick) is used to stop the remaining optical light. The silicon wafer is transparent to THz radiation and presents a flat transmission over the whole THz frequency range. To illustrate this point, the transmission of different materials has been measured using a commercial Fourier-Transform Infra-Red (FTIR) spectrometer (BRUKER IFS 66v/s). In Figure 9(b), one can see that only the low-density polyethylene (LDPE) and the silicon show a flat response in this range. The Teflon and the polystyrene exhibit full absorption after 6 THz. Furthermore, the LDPE does not fully block all the optical light which is undesired. Thus, the best filter appears to be the high resistivity silicon wafer from which losses are induced by Fresnel reflection at the surface due to its relatively high index in the THz range.

In the experimental setup the other arm takes a fraction of the initial laser pulse energy, which is used to probe the THz field using electro-optic sampling. The probe beam passes through an optical delay line which is mounted on a step motor. The motor has micrometer size step resolution, or fs time resolution. The sampling reconstruction of the THz electric field is achieved as explained in the previous section. We have used a pellicle beam splitter ( $\sim 5\mu\text{m}$  thick), to introduce the optical beam in a collinear way with the THz beam. Such material is commonly used as it is transparent in the THz range. A balanced arrangement was used to measure the induced phase delay on the probe beam. We have also built our own balanced photodiodes setup, which offers equivalent performance to the commercially available detectors. Finally, a purged gas chamber was installed in our THz spectrometer. This component is absolutely essential in order to correctly measure the emitted THz pulses, since THz radiation is strongly absorbed by the water vapor molecules present in air [22].

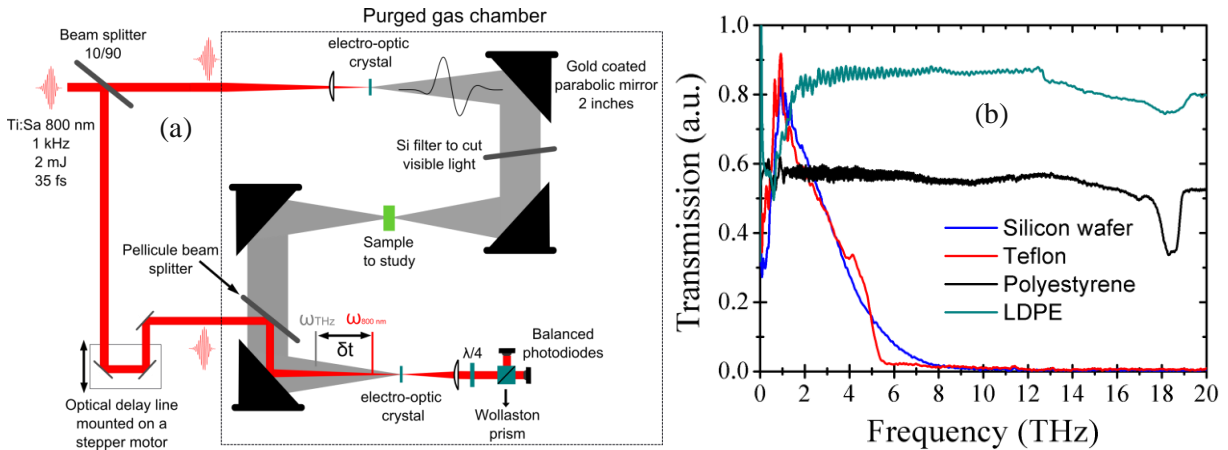


**Figure 9: (a) Schematic representation of our THz time domain spectrometer. (b) FT-IR transmission spectra of various filters transparent to THz and blocking optical light.**

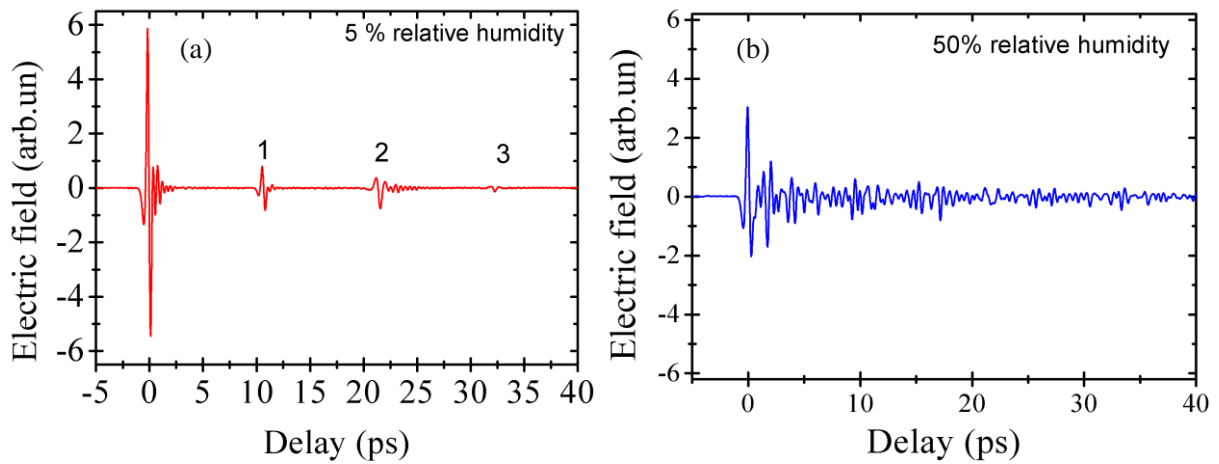


**Figure 10: Measured THz electric fields for different levels of relative humidity. (a) 5% RH, (b) 50% RH.**

Consequently, we have built a simple Plexiglas chamber which is continuously purged with dry air (0% relative humidity). This dry air comes from a purge gas generator that removes the water vapor of normal air. Then, the purged air is injected into the Plexiglas chamber of the THz spectrometer. With this approach it is possible to reach acceptable levels of humidity, around 2 to 5 %, in less than ten minutes of purge. An example of time domain traces obtained at different levels of Relative Humidity (RH) is presented in Figure 10. When the spectrometer has been purged with dry air, one is able to observe various echoes on the recorded time trace. Echo number 1 corresponds to the internal reflection occurring within the silicon wafer filter, while the echoes number 2 and 3 correspond to the internal reflection of the two main pulses within the detection crystal. These different echoes are not observable in the case of the propagation in a normal laboratory atmosphere. Such effect can seriously affect the interpretation of the measurements.

## I.4.2 Data Analysis

As mentioned previously, in a pulsed THz system, the waveform of the THz pulse  $E(t)$  represents the temporal evolution of the pulse electric field. The Fourier transform of the temporal waveform  $E(t)$  gives the spectral distribution of the THz pulse in the frequency domain. The THz field in the frequency domain is in principle a complex value containing both amplitude and phase information:

$$\tilde{E}(\omega) \equiv A(\omega)e^{-i\Phi(\omega)} = \int dt E(t)e^{-i\omega t}$$

A classic example of a time domain electric field recorded with our spectrometer is presented in Figure 11 (a). The emission was obtained from optical rectification within a 0.5 mm ZnTe crystal of a laser pulse at 800 nm, with 300  $\mu\text{J}$  energy and 35 fs pulse duration. The amplitude of its Fourier transform is presented in Figure 11 (b). The spectral resolution of a THz-TDS measurement,  $\delta\omega$ , is determined by the temporal scanning range  $T$ . The frequency range of the spectrometer is limited by the response of the THz source and detector, while mathematically the spectrum is significant within a bandwidth  $\Delta\Omega$ , which is related to the temporal sampling interval  $\delta t$ . In general the bandwidth and spectral resolution of a THz-TDS are given by:

$$\delta\omega = \frac{2\pi}{T} \quad , \quad \Delta\Omega = \frac{2\pi}{\delta t}$$

When a fast Fourier transform is used, the spectrum is symmetric around  $\Omega=0$ . Therefore, the frequency range spans from  $-1/(2\Omega)$  to  $1/(2\Omega)$ . In order to have a smooth calculated THz spectrum, the 0 padding technique may be applied. The 0 padding method adds several 0 values on one side or both sides of the THz waveform [22]. Padding with 0's mathematically increases the temporal scanning range  $T$ , and thus gives more data points in the THz spectrum. However, padding with 0's does not provide any additional information and does not improve the spectral resolution.

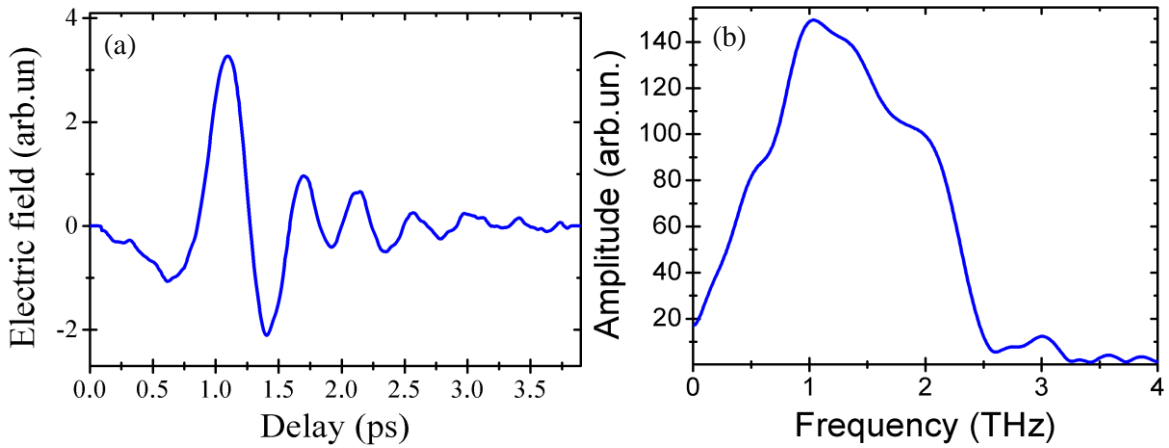


**Figure 11: (a) Measured THz electric field (Emission ZnTe 0.5 mm/ Detection ZnTe 1 mm). (b) THz pulse spectral amplitude.**

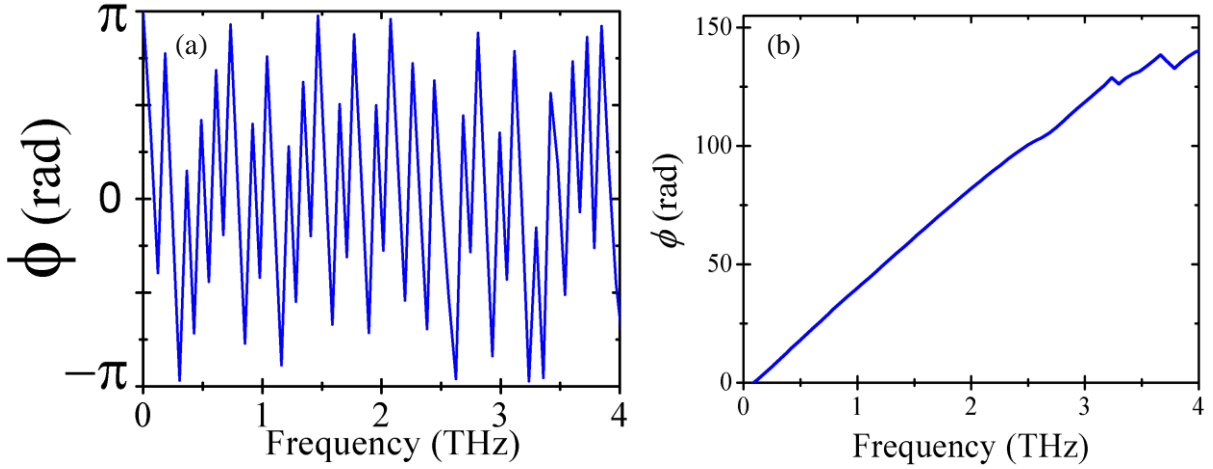


**Figure 12: (a) THz pulse spectral wrapped phase. (b) THz pulse spectral unwrapped phase.**

Because the phase is determined using the arctan, it can only be determined in the range  $(-\pi, \pi)$ , resulting in a saw tooth behavior with increasing frequency as depicted in Figure 12(a). The discontinuities should be removed to facilitate later calculations and for ease of visualization by adding  $2\pi$  at each point of discontinuity. Hence the phase is smoothed to a continuously increasing function without loss of information. This process is known as phase unwrapping (Figure 12(b)).

To measure the spectral response of a target, one should first record the THz waveform of a reference sample, i.e. free space. The THz waveform of the reference sample is called the reference waveform. The THz waveform transmitted through the target is called the signal waveform. Fourier transform of the reference and signal waveforms gives the reference spectrum,  $A_R(\omega)e^{-i\Phi_R(\omega)}$  and the signal spectrum,  $A_S(\omega)e^{-i\Phi_S(\omega)}$ , respectively [23]. The spectral properties of a sample of known thickness  $d$  can be extracted by comparing the signal spectrum with the reference spectrum.

The absorption coefficient is expressed as:

$$\alpha = -\frac{1}{d} \ln \left( \frac{A_R(\omega)}{A_S(\omega)} * T \right),$$

where  $T$  is the Fresnel reflection coefficient for normal incidence:  $T = \frac{(n(\omega)+1)^2}{4n(\omega)}$ .

And the refractive index  $n$  is equal to:

$$n = 1 + \frac{[\Phi_S(\omega) - \Phi_R(\omega)]c}{d\omega}.$$

Then we know, that the complex permittivity is related to the complex refractive index by the following expression:

$$\begin{aligned} \hat{\epsilon} &= \hat{n}^2, \\ \hat{n} &= n + ik, \end{aligned}$$

and where  $k$  is the extinction coefficient equal to:

$$k = \frac{\lambda\alpha}{4\pi} = \frac{c\alpha}{2\omega}.$$

Hence, the real and imaginary part of the permittivity can be extracted and defined as function of the frequency:

$$\begin{aligned}\varepsilon' &= n^2 - k^2, \\ \varepsilon'' &= 2nk.\end{aligned}$$

To illustrate this, we have used 5 different samples and recorded the THz electric field transmitted through them. Thus, we are able to define their respective index of refraction, absorption coefficient as well as their dielectric constant. We had at our disposition, two semiconductors samples of known thicknesses (SI-GaAs and a LT-GaAs), two glass samples (quartz and fused silica) as well as one polymer. In order to gain considerable amount of time in the treatment of the measured data, we have developed a Matlab code that automatically extracts the respective sample parameters. The results are presented in Figure 14 and are in really good agreement with the previously reported values [11]. Furthermore, the unidentified polymer sample seems to be a polyethylene sample according to the extracted mean refractive index of 1.66 and a mean real dielectric constant of 2.9 which are similar to the one reported in [10].

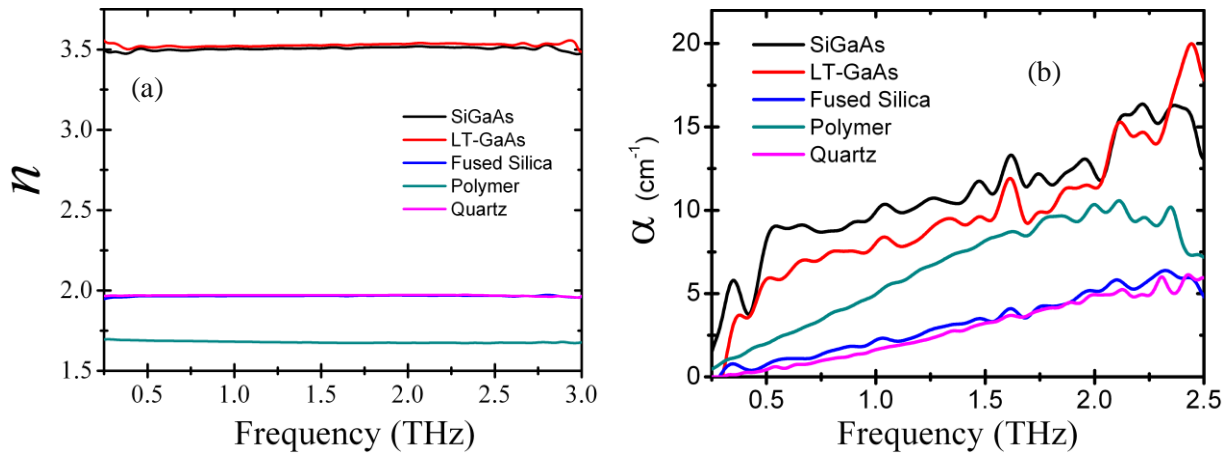


**Figure 13: (a) Calculated refractive indexes and (b) Coefficient of absorption.**

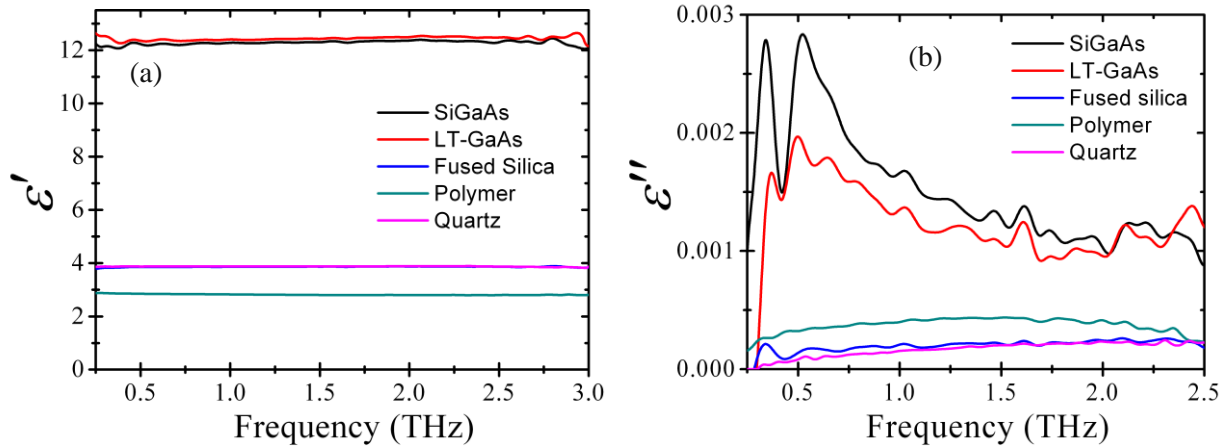


**Figure 14: (c) Real part of permittivity (d) Imaginary part of permittivity. These are the calculated values for different materials.**

The approach described above for material parameters extraction is not valid for thin films and do not take into account the potential Fabry-Perot etalon effect occurring in material with thickness close to the used wavelength. A more accurate iterative approach is presented in [24].

## I.5/ State of the art in table-top THz pulsed system

So far, the basic requirements for THz time domain spectroscopy and its applications have been presented. In order to put this thesis into perspective, it is important to review the state of the art in the field at the beginning of this work. From the literature, three trends in the development of pulsed THz science have been identified.

### I.5.1 Ultra broadband sources for spectroscopic applications

The emission and detection of coherent THz pulses using electro-optic crystals is highly dependent on the crystal thickness as well as the initial laser pulse duration. In the example presented in the previous section, the useful spectral bandwidth extended from 0.25 to 3 THz. The emitted and detected THz bandwidth can be greatly improved while using much thinner crystals and shorter laser pulse durations. For example in [25], using 30  $\mu\text{m}$  thick ZnTe emitter, 27  $\mu\text{m}$  thick ZnTe sensor with an initial pulse duration of 12 fs at 800 nm, the authors demonstrated the coherent measurement of free-space broadband radiation spanning from 100 GHz to over 30 THz. Another example of an ultra broadband source has been reported in [26]. In this article, the emitting and detecting GaSe crystals were respectively 20  $\mu\text{m}$  and 30  $\mu\text{m}$  thick. Using initial laser pulse duration of 10 fs a 40 THz 3dB bandwidth has been demonstrated. Furthermore the central frequencies of the bands were shown to be tunable in the

frequency interval between 14 and 31 THz via the tilt of the detection crystal with respect to normal incidence position.

### I.5.2 Technological developments for THz imaging applications

Imaging with THz pulses requires scanning in three dimensions, including space (2-D) and time (1-D), thus it is usually very time consuming. The raster scanning technique [5] has been largely improved with the introduction of 2-D Focal Plane THz Wave Imaging [27]. This method which is similar to a traditional optical imaging system, directly images the THz wave transmission or reflection from the target onto an extended THz wave sensor. The THz wave image of the target is simultaneously recorded using the extended sensor. Since no scanning is required, 2D THz wave image highly reduces the acquisition time. The extended THz wave sensor could be THz wave detector array, such as pyroelectric detector array, micro-bolometer array, heterodyne detector array or an EO crystal with sufficient aperture. Another technological development that improved the acquisition speed of THz systems is the detection of the THz waveform using a single laser pulse [28]. With this approach, the THz waveform is evaluated either by the spatial or spectral distribution of the probe pulse. The single laser pulse detection technique provides a significant reduction in the acquisition time and greatly extends the applicability of THz systems in situations where the sample is moving. These two techniques, in combination with the time of flight information available while recording the entire THz waveform, have made the real-time two-dimensional THz tomography of moving objects a reality [29]. Furthermore, various approaches have been used in order to obtain a sub-wavelength resolution based on near-field techniques. A detailed review can be found in [30].

### I.5.3 High peak power sources for non-linear applications

THz pulsed techniques were first developed for systems employing high-repetition-rate (i.e. 100 MHz) fs pulse lasers. However, soon after the technique was adapted to low-repetition-rate amplified laser systems (with pulse energies typically in the  $\mu\text{J}$ – $\text{mJ}$  range) in order to gain access to higher THz pulse energies. Upon tight focusing of the THz radiation, electric fields of hundreds of  $\text{kV}\cdot\text{cm}^{-1}$  could potentially be obtained, which would be sufficient to access physical phenomena in a regime where they depend nonlinearly on the electric field. Moreover, at higher level of energy, THz pump/THz-probe experiments would become a reality. The two techniques previously described in this chapter, systematically lead to saturation at certain level of laser input energy. Consequently one approach to increase the yielded THz pulse energy is to extend the size of the emitter [31, 32].

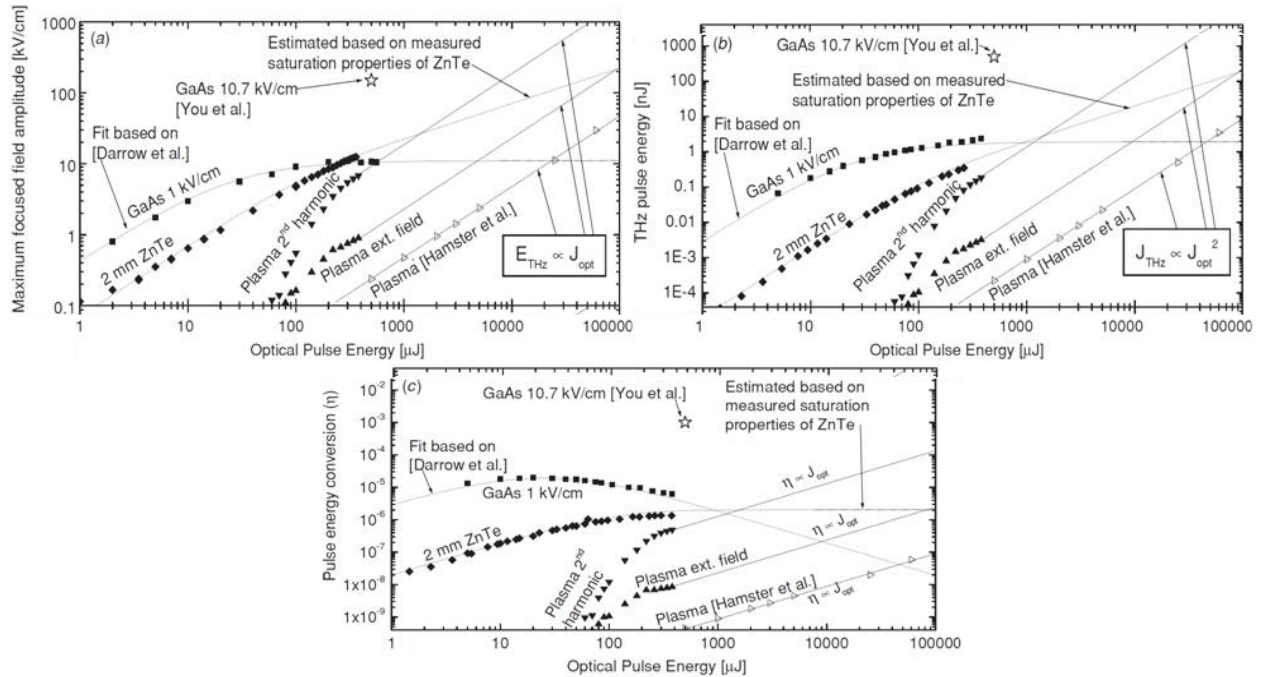


**Figure 15: Comparison of (a) the focused peak electric field, (b) the THz-pulse energy and (c) the energy conversion efficiency for different THz emission approaches (Ref. [33]).**

Nevertheless, for both techniques, scaling-up the size of the emitter does not resolve the problem of damage threshold occurring in materials. A very different class of THz emitters which are suitable for use with amplifier laser systems is based on laser-generated plasmas [34, 35]. The basic concept of these emitters is to focus a short high-energy laser pulse in a gaseous medium and form a plasma filament. If one now manages to achieve a net polarization within the plasma, the time-dependent macroscopic dipole-moment will lead to the emission of THz radiation. Such THz source appeared to be one of the most promising in terms of yielded THz energy [33]. The projection for higher input laser pulse energy (see Figure 15) clearly suggested that plasma 2nd harmonic source should reach the level of μJ per pulse.

## I.6/ Thesis outline.

The work in this thesis, which was performed between October 2006 and May 2010, is focused on the development and applications of a Laser-driven THz secondary source. At the start of this period, pulsed THz system, typically used MHz repetition rate lasers in combination with photoconductive antennas or electro-optical crystals. The yielded THz pulse energy was relatively small, limiting applications of THz science to imaging and spectroscopy. A promising alternative to reach higher THz peak power is to use the plasma based source as presented in the previous section. Furthermore, this approach, which was quasi-unexplored at the beginning of my thesis, is in accordance with the field of expertise within our research group. Consequently, this thesis has been orientated towards the development, the optimization and the use of a plasma based source.

The remainder of this thesis is therefore organized as follows. Chapter II presents a review on the laser filamentation process and the different ways filaments emit THz radiation. Also in the same chapter we present our results and contributions to the field, which have brought valuable information to the understanding of the physical phenomena involved in the emission of THz pulses from filaments. Finally, the attributes of our THz source are described. Chapter III discusses the optimization of our THz source. Using filamentation tailoring approaches, we have demonstrated various ways to optimize the emission of THz pulses. Our innovative work includes the demonstration of THz pulse shortening, THz pulse energy enhancement as well as the control of the THz pulse polarization state spanning from linear to fully circular.

The last three chapters of this thesis illustrate various applications of our intense ultrashort THz pulse source. Chapter IV discusses the application of THz pulse system to the diagnosis of cultural heritage materials. Spectroscopic data obtained in transmission and reflection are presented. The imaging potential of the technique is also demonstrated. Chapter V presents our studies on Metamaterials operating at THz frequencies. Emphasis is given on the dynamical capabilities of such materials, with the demonstration of frequency tunable devices, phase control, as well as the switching between electric resonances. Chapter VI describes our recent experiments on non-linear phenomena using our intense ultrashort THz pulses. Franz-Keldysh effect, direct phonon excitation, THz self-phase modulation and electro-optic distortions, are demonstrated. Finally, chapter VII summarizes the results, and gives perspectives for further work.

## References

1. Fattinger, C. and D. Grischkowsky, Terahertz beams. *Applied Physics Letters*, 1989. 54(6): p. 490-492.
2. Woodward, R.M., et al., Terahertz pulse imaging of ex vivo basal cell carcinoma. *Journal of Investigative Dermatology*, 2003. 120(1): p. 72-78.
3. Federici, J.F., et al., THz imaging and sensing for security applications - explosives, weapons and drugs. *Semiconductor Science and Technology*, 2005. 20(7): p. S266-S280.
4. Fitzgerald, A.J., B.E. Cole, and P.F. Taday, Nondestructive analysis of tablet coating thicknesses using terahertz pulsed imaging. *Journal of Pharmaceutical Sciences*, 2005. 94(1): p. 177-183.
5. Hu, B.B. and M.C. Nuss, Imaging with terahertz waves. *Optics Letters*, 1995. 20(16): p. 1716-&.
6. Kawase, K., et al., Non-destructive terahertz imaging of illicit drugs using spectral fingerprints. *Opt. Express*, 2003. 11(20): p. 2549-2554.
7. Walther, M., et al., Collective vibrational modes in biological molecules investigated by terahertz time-domain spectroscopy. *Biopolymers*, 2002. 67(4-5): p. 310-313.
8. Fischer, B.M., M. Walther, and P.U. Jepsen, Far-infrared vibrational modes of DNA components studied by terahertz time-domain spectroscopy. *Physics in Medicine and Biology*, 2002. 47(21): p. 3807-3814.
9. Markelz, A.G., A. Roitberg, and E.J. Heilweil, Pulsed terahertz spectroscopy of DNA, bovine serum albumin and collagen between 0.1 and 2.0 THz. *Chemical Physics Letters*, 2000. 320(1-2): p. 42-48.
10. Jin, Y.S., G.J. Kim, and S.G. Jeon, Terahertz dielectric properties of polymers. *Journal of the Korean Physical Society*, 2006. 49(2): p. 513-517.
11. Grischkowsky, D., et al., Far-infrared time-domain spectroscopy with terahertz beams of dielectrics and semiconductors. *J. Opt. Soc. Am. B*, 1990. 7(10): p. 2006-2015.
12. Beard, M.C., G.M. Turner, and C.A. Schmuttenmaer, Transient photoconductivity in GaAs as measured by time-resolved terahertz spectroscopy. *Physical Review B*, 2000. 62(23): p. 15764-15777.
13. Ozyuzer, L., et al., Emission of coherent THz radiation from superconductors. *Science*, 2007. 318(5854): p. 1291-1293.
14. Dekorsy, T., et al., THz electromagnetic emission by coherent infrared-active phonons. *Physical Review B*, 1996. 53(7): p. 4005-4014.
15. Kreisler, A.J. and A. Gaugue, Recent progress in high-temperature superconductor bolometric detectors: from the mid-infrared to the far-infrared (THz) range. *Superconductor Science & Technology*, 2000. 13(8): p. 1235-1245.
16. Kimmitt, M.F., *Reststrahlen to T-Rays – 100 Years of Terahertz Radiation*. *Journal of Biological Physics*, 2003. 29(2): p. 77-85.
17. Leisawitz, D., et al. Far-IR/submillimeter space interferometry: scientific motivation and technology requirements. in *Aerospace Conference*, 2001, IEEE Proceedings. 2001.
18. Tonouchi, M., Cutting-edge terahertz technology. *Nat Photon*, 2007. 1(2): p. 97-105.
19. Dooley, D., Sensitivity of broadband pyroelectric terahertz detectors continues to improve. *Laser Focus World*. 46(5): p. 49-53.

20. Gutschwager, B., et al., Calculable blackbody radiation as a source for the determination of the spectral responsivity of THz detectors. *Metrologia*, 2009. 46(4): p. S165-S169.
21. Siegel, P.H., Terahertz technology. *Ieee Transactions on Microwave Theory and Techniques*, 2002. 50(3): p. 910-928.
22. Exter, M.v., C. Fattinger, and D. Grischkowsky, Terahertz time-domain spectroscopy of water vapor. *Opt. Lett.*, 1989. 14(20): p. 1128-1130.
23. *Terahertz Spectroscopy: Principles and Applications*. 2008.
24. Duvillaret, L., F. Garet, and J.L. Coutaz, A reliable method for extraction of material parameters in terahertz time-domain spectroscopy. *IEEE Journal of Selected Topics in Quantum Electronics*, 1996. 2(3): p. 739-746.
25. Han, P.Y. and X.C. Zhang, Coherent, broadband midinfrared terahertz beam sensors. *Applied Physics Letters*, 1998. 73(21): p. 3049-3051.
26. Kubler, C., et al., Ultrabroadband detection of multi-terahertz field transients with GaSe electro-optic sensors: Approaching the near infrared. *Applied Physics Letters*, 2004. 85(16): p. 3360-3362.
27. Wu, Q., T.D. Hewitt, and X.C. Zhang, Two-dimensional electro-optic imaging of THz beams. *Applied Physics Letters*, 1996. 69(8): p. 1026-1028.
28. Jiang, Z.P. and X.C. Zhang, Single-shot spatiotemporal terahertz field imaging. *Optics Letters*, 1998. 23(14): p. 1114-1116.
29. Yasuda, T., et al., Real-time two-dimensional terahertz tomography of moving objects. *Optics Communications*, 2006. 267(1): p. 128-136.
30. Zhang, X.-C. and J. Xu, *Introduction to THz Wave Photonics*. 2010, Springer.
31. You, D., et al., Generation of high-power sub-single-cycle 500-fs electromagnetic pulses. *Opt. Lett.*, 1993. 18(4): p. 290-292.
32. Löffler, T., et al., Large-area electro-optic ZnTe terahertz emitters. *Opt. Express*, 2005. 13(14): p. 5353-5362.
33. Löffler, T., et al., Comparative performance of terahertz emitters in amplifier-laser-based systems. *Semiconductor Science and Technology*, 2005. 20(7): p. S134-S141.
34. Cook, D.J. and R.M. Hochstrasser, Intense terahertz pulses by four-wave rectification in air. *Opt. Lett.*, 2000. 25(16): p. 1210-1212.
35. Hamster, H., et al., Subpicosecond, electromagnetic pulses from intense laser-plasma interaction. *Physical Review Letters*, 1993. 71(17): p. 2725.



*Chapter II: Generation of intense broadband  
THz pulses from filament in air*

<b>CHAPTER II: GENERATION OF INTENSE BROADBAND THZ PULSES FROM FILAMENT IN AIR .....</b>	<b>38</b>
<b>II.1/ Introduction to the filamentation process.....</b>	<b>40</b>
II.1.1 Properties of ultrashort pulse nonlinear propagation.....	41
II.1.2 Properties of light filaments .....	46
<b>II.2/ THz Emission from filament in air.....</b>	<b>48</b>
II.2.1. THz emission from single color filament.....	48
a) Radial and conical emissions .....	48
b) On-axis emission.....	50
II.2.2. THz emission from two color filament.....	55
a) The genesis of a controversy.....	55
b) Coherent control of THz pulses polarization .....	57
II.2.3 Characterization of the source.....	60
a) Bandwidth .....	60
b) Beam size .....	61
c) Electric field strength .....	62
d) Angular diagram of emission.....	63
<b>II.3/ Chapter conclusions .....</b>	<b>64</b>
References .....	65

## II.1/ Introduction to the filamentation process

The propagation of electromagnetic pulses has been the subject of intense research in fundamental and applied physics. Thanks to the appearance of chirped pulse amplified laser systems in 1985 [1], the laser peak intensities have been tremendously enhanced. Since, various non-linear phenomena, which occur during the propagation of high intensity ultrashort laser pulses in air, have been observed. One of the most impressive, and unusual, phenomenon is the so-called filamentation. The first experimental observation of femtosecond laser filamentation was reported in 1995 [2]. The results indicated the presence of a self-trapped laser beam, induced by non-linearities, which persisted over a long distances in air. The formation of filaments can be described as a self-action process in which an ultrashort laser pulse, with sufficient power, undergoes strong spatial and temporal reshaping as it propagates in a transparent medium. This results in the propagation of the beam with a very narrow waist which remains almost constant over many Rayleigh lengths, leaving ionized channels in its wake. This phenomenon appears for input powers close to or above a critical value,  $P_{cr}$ . It is the result of a competition involving linear and highly nonlinear effects, such as the optical Kerr effect, defocusing due to plasma created by optical field ionization, nonlinear losses, dispersion and others [3].

The following section presents the principles of ultrashort laser pulse nonlinear propagation and enlightens various properties of light filaments reported in the literature.

## II.1.1 Properties of ultrashort pulse nonlinear propagation

The physical origin of the formation of filaments in air is today well understood. Even though many physical effects play a role in the nonlinear propagation of intense laser beams, the filamentation process of its formation can be described by the action of two main nonlinear physical effects. On one hand, the optical Kerr effect acts against diffraction and tends to focus the beam on itself. On the other hand during self-focusing, the beam intensity becomes higher and reaches levels that are sufficient to ionize the surrounding gas. This ionization effect reduces the local refractive index of the medium and leads to beam defocusing. The dynamical equilibrium between these two phenomena results in the formation of a filament as schematically represented in Figure 16.

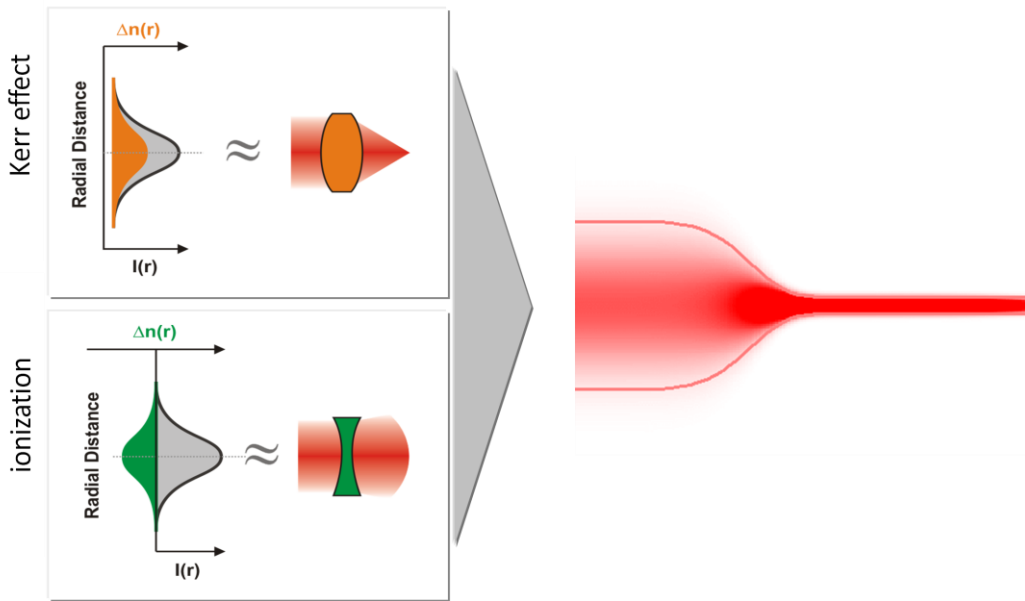


**Figure 16: Schematic representation of filamentation.**

The origin of self-focusing is related with the nature of the refractive index. In the presence of a strong laser field, the refractive index of air (as well as for any transparent medium) is not only dependent on the frequency of the laser field, but also on its spatio-temporal intensity distribution according to the following relation:

$$n = n_0 + n_2 I(r, t) .$$

Since the intensity of a Gaussian beam is higher at the center, an effect of curvature occurs on the wavefront, which is equivalent to a positive focusing lens. This effect is schematically represented in Figure 16. The key parameter for self-focusing is the so-called critical power. The phenomenon will only occur if the input power goes over this threshold. For a Gaussian beam, the critical power is expressed as:

$$P_{cr} \equiv \frac{3.77\lambda_0^2}{8\pi n_0 n_2} .$$

During the self-focusing process, the intensity ( $\text{W}/\text{cm}^2$ ) dramatically increases to the point where it will be possible to ionize the medium. Multiphoton ionization (MPI) is the first process to occur and its rate scales as  $I^k$ , where  $k$ , the number of simultaneously absorbed photons, is approximately equal to 8 for air, at a laser wavelength 800 nm. At higher intensities, tunnel ionization occurs where an electron escapes through the barrier formed by the electromagnetic field and the Coulomb potential. The direct effect of this plasma formation is a local reduction of the refractive index. This effect acts as a negative defocusing lens, preventing the beam from collapsing. The index variation due to the plasma is expressed as:

$$n \approx n_0 - \frac{\rho(r, t)}{2\rho_c}$$

Filamentation can thus be seen as a direct competition between these two phenomena. This inherently led to the concept of intensity clamping, which is the intensity that cannot be exceeded within the filament:

$$I \sim \left( \frac{2n_2\rho_c}{\sigma_K t_p \rho_{at}} \right)^{K-1}$$

Typically for a pulse duration of 100 fs and a wavelength of 800 nm,  $I \sim 1.8 \times 10^{13} \text{ W}/\text{cm}^2$

However, this description of filamentation is rather succinct and it would be too simplistic and inaccurate to describe filamentation using such a qualitative approach. Phenomena such as self-phase modulation (SPM), self-steepening and losses related to multiphoton absorption and to plasma absorption are taking part with a lower impact on the process of filamentation. For this reason a full numerical model for pulse propagation has been developed through the years and offers a deeper insight into the filamentation process [3]. The first numerical simulations started with a minimal model which described the phenomena mentioned above. From Maxwell equations and the equations describing the medium, a vector wave-equation governing the evolution of the laser pulse in a transparent nonlinear medium can be deduced:

$$\nabla^2 \mathbf{E} - \nabla(\nabla \cdot \mathbf{E}) - \frac{1}{c^2} \frac{\partial^2}{\partial t^2} \int_{-\infty}^t n^2(\mathbf{r}, t - t') \mathbf{E}(t') dt' = \mu_0 \left( \frac{\partial^2 \mathbf{P}_{nl}}{\partial t^2} + \frac{\partial \mathbf{J}_p}{\partial t} \right)$$

Considering the laser field as linearly polarized, the electric field can be decomposed into a carrier wave and an envelope:

$$\mathbf{E}(x, y, z, t) = \frac{1}{2} \mathcal{E}(x, y, z, t) \exp[i(kz - \omega_0 t)] \mathbf{e}_x + c. c.,$$

where  $z$  is the direction of propagation,  $k$  and  $\omega_0$  the central wavenumber and frequency of the laser pulse respectively. By neglecting the vectorial operator and using the reference frame of the pulse, a scalar equation of nonlinear Schrodinger type is obtained:

$$\frac{\partial \mathcal{E}}{\partial z} = \frac{i}{2k} \Delta_{\perp} \mathcal{E} + ik_0 n_2 |\mathcal{E}|^2 \mathcal{E} - i \frac{k_0}{2n_0} \frac{\rho}{\rho_c} \mathcal{E},$$

where  $\Delta_{\perp}$  denotes the diffraction in the transverse plane

$$\Delta_{\perp} \equiv \frac{\partial^2}{\partial x^2} + \frac{\partial^2}{\partial y^2}.$$

The second term which describes the Kerr effect has been derived from the nonlinear polarization expression:

$$\mathbf{P}_{\text{nl}} \equiv \varepsilon_0 \chi^{(3)} |\mathbf{E}|^2 \mathbf{E}, \quad \text{where } \chi^{(3)} = \frac{4\varepsilon_0 c n_2 n_0^2}{3}.$$

And the third term describes the plasma defocusing and is obtained from:

$$\frac{\partial \mathbf{J}_p}{\partial t} = -\frac{e^2}{m_e} \rho \mathbf{E}.$$

This equation must be solved simultaneously with the equation that describes the evolution of the electron density generated by photoionization:

$$\frac{\partial \rho}{\partial t} = \sigma_K |\mathcal{E}|^{2K} \rho_{\text{at}}.$$

As mentioned previously, this model remains minimal and has been subject of further development. The other contributing effects have been added as sources to this first model, resulting in a more accurate description of the laser pulse propagation. The fully developed model takes into account the group velocity dispersion and the Raman contribution for the laser pulse propagation. Plasma and multiphoton absorption, as well as avalanche and recombination effects are also considered for the generation of electrons.

$$\frac{\partial \mathcal{E}}{\partial z} = \frac{i}{2k} \left( \frac{\partial^2}{\partial x^2} + \frac{\partial^2}{\partial y^2} \right) \mathcal{E} - i \frac{k''}{2} \frac{\partial^2 \mathcal{E}}{\partial t^2} + N(|\mathcal{E}|^2, \rho) \mathcal{E}.$$

The first term remains the same and relates to the diffraction in the transversal plane. The second term accounts for group velocity dispersion with  $k'' = \partial^2 k / \partial \omega^2 |_{\omega_0}$ .

The other terms added in the equations are grouped under:

$$N(|\mathcal{E}|^2, \rho) = N_{\text{kerr}}(|\mathcal{E}|^2) + N_{\text{plasma}}(\rho) + N_{\text{MPA}}(|\mathcal{E}|^2),$$

with the Kerr term equal to:

$$N_{\text{kerr}}(|\mathcal{E}|^2) = ik_0 n_2 (1 - \alpha) |\mathcal{E}(x, y, z, t)|^2 + ik_0 n_2 \alpha \int_{-\infty}^t \mathcal{R}(t - \tau) |\mathcal{E}(x, y, z, \tau)|^2 d\tau.$$

The above equation is split into an instantaneous component, which describes the electronic response in the polarization, and a delayed component of fraction  $\alpha$ , which describes stimulated Raman scattering characterized by the function  $\mathcal{R}$ .

The plasma term is expressed by the following equation:

$$N_{\text{plasma}}(\rho) = -\frac{\sigma}{2} (1 + i\omega_0 \tau_c) \rho,$$

where the real part represents the plasma absorption and the imaginary part describes the plasma defocusing effect. The evolution of electron density used in the above equation is expressed as:

$$\frac{\partial \rho}{\partial t} = \sigma_K |\mathcal{E}|^{2K} (\rho_{at} - \rho) + \frac{\sigma}{U_i} \rho |\mathcal{E}|^2 - a\rho^2.$$

This equation describes the generation of plasma by multiphoton ionization at a rate of  $\sigma_K |\mathcal{E}|^{2K}$  and avalanche at a rate of  $\frac{\sigma}{U_i} \rho |\mathcal{E}|^2$ . The last term accounts for plasma recombination where an electron is captured by the ion. The last term added into the propagation model, accounts for energy absorption due to multiphoton ionization:

$$N_{MPA}(|\mathcal{E}|^2) = -\frac{\beta_K}{2} |\mathcal{E}|^{2K-2} \left[ 1 - \frac{\rho}{\rho_{at}} \right].$$

The coefficient  $\beta_K = K\hbar\omega_0\rho_{at}\sigma_K$  is related to the multiphoton ionization coefficient.

To start the propagation initial conditions must be given. The most commonly use input pulses are Gaussians. The input beams are modeled by collimated or focused Gaussian profiles with a peak input intensity  $I_0$ , a transverse waist  $\omega_0$ , an input peak power  $P_{in} = \pi\omega_0^2 I_0/2$  and an energy  $E_{in} = P_{in}t_p\sqrt{\pi/2}$ :

$$\mathcal{E}(x, y, t, 0) = \sqrt{I_0} \exp \left[ -\frac{x^2 + y^2}{\omega_0^2} - i\frac{kr^2}{2f} - \frac{t^2}{t_p^2} - iCt^2 \right],$$

where a chirp  $C$  can be added to the pulse, as well as the curvature in case of focusing conditions.

Once the initial conditions are set, the laser pulse propagation can be calculated with the model presented above. Typically, analysis of the calculations offers a direct view on diverse parameters such as the beam transverse dimension along the propagation axis. The intensity and the generated density of electrons along the propagation axis can also be plotted as well as the fluence as presented in Figure 17. The pulse duration at different positions along the propagation axis can also be obtained as presented on Figure 18. A detailed review on the femtosecond laser filamentation can be found in [3].

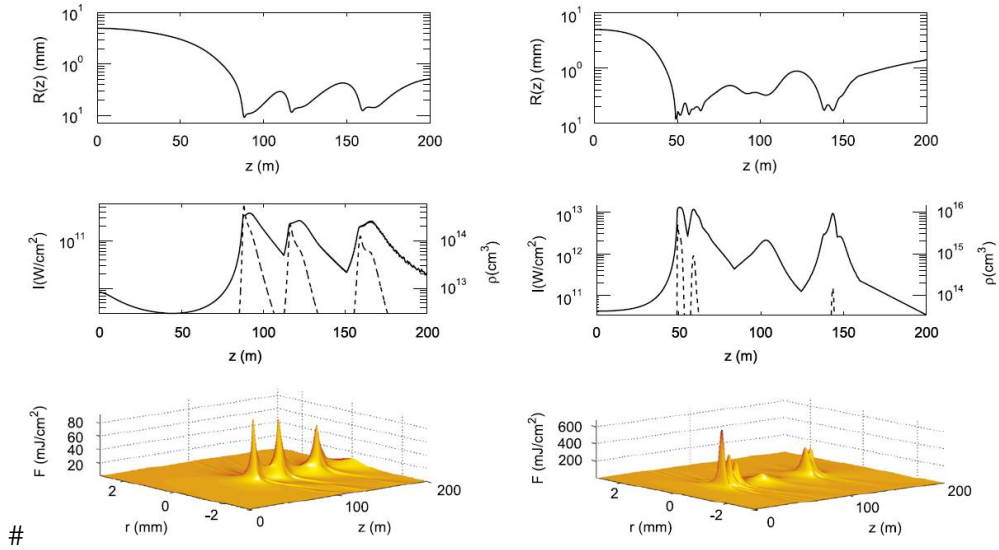


**Figure 17: Propagation of a collimated beam (diameter of 1 cm) in air for an ultraviolet laser pulse (first column:  $\lambda = 248$  nm,  $\tau_{FWHM} = 100$  fs, 1 mJ) and for an infrared laser pulse (second column:  $\lambda = 800$  nm,  $\tau_{FWHM} = 100$  fs, 3 mJ). The initial power of the pulse is slightly larger than the critical power for self-focusing  $P_{cr}^{UV} = 0.12$  GW,  $P_{cr}^R = 3.2$  GW. The beam radius  $R(z)$ , the maximum intensity (solid curve, left axis), the density of free electrons on-axis (dashed curve, right axis) and the fluence distribution are plotted as a function of the propagation distance. (Ref. [3]).**

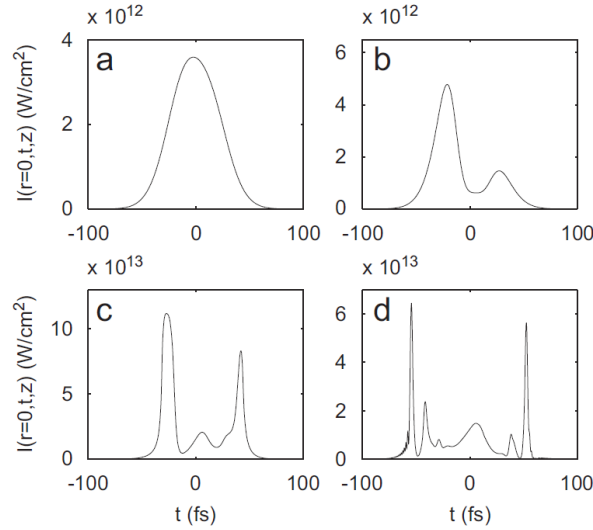


**Figure 18: Pulse temporal profile at successive propagation distances during filamentation. (a) The initial pulse. (b) The pulse splits into two when it propagates beyond the nonlinear focus. (c) The substructures are shortened and stiffened. (d) Shortening and stiffening are reinforced and accentuated during the propagation in the form of a filament. (Ref. [3]).**

## II.1.2 Properties of light filaments

A light filament has properties that are directly observable with the naked eye. One of the most impressive is the colored conical emission that accompanies it. A CCD image taken in our laboratory is shown in Figure 19. Even though the blue rings are not visible on this picture, the radial ordering of the rings is inverted to diffraction, with the red ring inside and the blue ring outside. Several theories have been offered to explain this emission [4].



**Figure 19: CCD picture of a filament conical emission obtained in our laboratory.**

Another visible attribute of filamentation is the fluorescence from electrons. The CCD image in Figure 20, which was taken in our laboratory, shows luminescence which is the result of molecule being ionized by the laser field. It has been used for characterization of plasma filaments.



**Figure 20: CCD picture of a filament fluorescence taken in our laboratory.**

Furthermore, properties such as X-wave formation have been observed through the use of an imaging spectrometer (see Figure 21). Such waves are stationary solution to the paraxial propagation equation that may propagate without experiencing diffraction and dispersion over long distances. Their name comes from the fact that they exhibit a conical energy flux with an “X” shaped intensity tail in both the near field ( $r, t$ ) and far-field ( $\theta, \lambda$ ). An example of such a far-field angular spectrum, obtained in our laboratory [5], is shown in Figure 6.

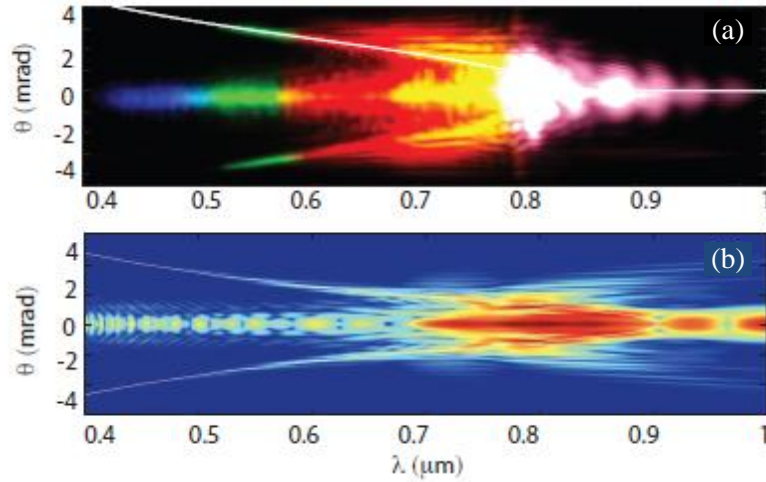


**Figure 21: (a) Measured ( $\theta$ ;  $\lambda$ ) spectra of filaments in air generated using a 10 m lens. (b) Shows the numerically calculated spectrum for the experimental settings of (a) (Ref. [5]).**

This phenomenon may also be responsible for the filamentation process in the absence of plasma formation. It was demonstrated that the sub-diffraction propagation can be sustained with the X-shaped energy flux refilling the intense core along the propagation [5].

Filamentation exhibits other interesting properties that can find potential applications in other fields of optics. For example, it has been observed experimentally, that during the filamentation process, the laser pulse experiences substantial shortening down to 5.7 fs from an initial pulse duration of 43 fs [6]. Some calculations even demonstrate the possibility to shorten the pulse length to a single optical cycle [7]. The production of intense single cycle optical pulses is of great importance in order to produce attosecond pulses from high-order harmonic generation in the far UV.

As a consequence of the strong temporal reshaping of the pulse within the filament, a spectral broadening is observable leading to the production of the so-called white light continuum, which extends up to the infrared [8, 9]. Another impressive property of filaments is their capacity to propagate over hundreds of meters, once the correct input parameters are selected [10]. Consequently, the last two enumerated properties makes filamentation an attractive tool for LIDAR atmosphere analysis [11]. Another impressive property of filaments is their capability to trigger and guide electric discharges [12], which may offer the ability to trigger lightning from the sky.

It is also important to note that filaments can occur in condensed media. They occur with the same properties as filaments in air but with reduced dimensions. For example, only 1  $\mu\text{J}$  is necessary in order to form a filament in a transparent solid such as fused silica. The diameter of this filament is about 30 times smaller than a filament created in gases [13]. In this case the ionization of electrons in air is replaced with electrons being excited from the valence to the conduction band. This filamentation process in solids can lead to a permanent refractive index changes in the bulk of glasses without damage and has already been used for the writing of waveguides or gratings [14].

Finally, a couple of techniques used for the characterization of a filament dimensions. The first technique is based on the measurement of the electric conductivity of air, in the presence of a filament [15]. This technique can be easily implemented and gives a good indication of the length of the filament. Another technique, called *in-line holography*, allows the measurement of the diameter of a filament and gives an accurate estimation of the electron density [16]. Though this technique cannot resolve very long filamentary structure, it can be combined with the conductivity technique for a precise diagnosis of filaments.

## II.2/ THz Emission from filament in air

Plasma strings formed by high intensity ultrashort laser pulses have received considerable attention in the last 20 years as novel sources for radiation. The measured radiations include high harmonics of the fundamental laser pulses, soft and hard X-rays, as well as THz radiation on the low frequency side of the electromagnetic spectrum. The first experimental demonstration of THz emission from laser-plasma interaction was performed in 1993 [17]. Seven years later, two important experimental results made a significant contribution to the field of THz emission from filament. The common point of these two publications is the dramatic improvement in the strength of this THz radiation. This was achieved by introducing a transverse asymmetry on the electric field in the plasma. First a DC bias voltage of few ten's kV/cm was applied in the vicinity of the plasma, which increased the power of the source by at least one order of magnitude [18]. The other approach introduced a second harmonic crystal into the path of the fundamental laser beam to partially double its frequency [19]. The latter technique has become, by far, the most popular and is often named as the dual-color filamentation technique

Consequently, before reviewing and entering in details on the generation mechanism of THz radiation from plasma strings, it is important to already divide the field in two sections. One is the THz emission from single color filamentation process, and the other is the emission of THz from two-color filaments. We will see in the following sections, that depending on the approach, the spatial properties of the emission can differ and, more importantly, the strength of these two sources is different by orders of magnitude.

### II.2.1. THz emission from single color filament

#### a) Radial and conical emissions

As mention in the introduction, the first demonstration of THz emission by laser-plasma interaction was reported approximately 20 years ago [17]. The emission was interpreted as being the result of a longitudinal photocurrent generated by the separation of ions and electrons in the wake of the laser front pulse. This separation of charges is due to the presence of ponderomotive forces. At a later stage, an alternative interpretation was proposed [20]. There it was suggested that the longitudinal current formed in the wake of the filament is the result of the radiation pressure induced

by the laser pulse. Consequently the electrons oscillate at the plasma frequency (plasma frequency formula) and generate the transient current which radiates the EM pulses. In the same work, simulations predicted the emission of THz radiation in a narrow cone perpendicular to the plasma axis. Experimental measurements of such emission was reported a year later [21]. Using an heterodyne detector operating at 94 GHz, the emission was shown to be constant along the filamentary structure. Furthermore, it was demonstrated that the emitted radiation is coherent, since once a second source was added and appropriately delayed in time; the emitted radiation was enhanced by a factor 4. It is also important to note here that this technique offered a new non-invasive approach to detect air ionization, and has been used as a diagnostic tool in various publications [22, 23].

However, the interpretation of this phenomenon has been the subject of debate and later it was shown that the THz radiation originates from the ponderomotive forces[24]. In this paper the authors showed that the radial emission is possible as long as a Cherenkov-like condition is satisfied. This means that the ionization front has superluminal Fourier components. Evidence of superluminal propagation in filaments has been reported in [22]. More recently the presence of an emission pattern consisting of a hollow cone radiation in the forward direction was reported [25]. The strength of the emitted field is by one order of magnitude higher than the radially emitted field. Furthermore, the polarization of this radiation is independent of the laser polarization. The radiation is radially polarized, which means it lies within a plane defined by the propagation axis,  $z$ , and the detector. This observation definitely invalidated the mechanism proposed in [20], since emission from a cloud of free electrons oscillating at the plasma frequency should keep the initial polarization of the laser pulse. The same group developed a theoretical model in order to explain both, the radial and the conical emission of THz. This model is presented as a Cherenkov-like process, of a dipole electric current moving in the trail of the laser pulse ionization front. The similarities to the Cherenkov emission lie in the fact that the emission is confined on the surface of a cone along the propagation direction, it is radially polarized and the source size is much smaller than the emitted wavelength. Nevertheless, the emission differs from the Cherenkov process for two reasons. First, the ponderomotive forces separate the charges but the wake of the filament remains neutral. The moving source is in this case a dipole-like structure. Second, the dipole structure moves exactly at the speed of light. Consequently, it would not radiate within an infinite plasma string. The radiation occurs because of the finite length of the filament, which also controls the opening angle ( $\theta$ ) of the emitted cone pattern. Starting from the calculation of longitudinal current formed in the wake of a filament by ponderomotive forces and using recent results on finite orbit length on the Cherenkov emission of a charge particle [26], the authors were able to derive the energy spectral density of the emitted electromagnetic radiation in units of solid angle. It is expressed as following:

$$\frac{d^2W}{d\omega d\Omega} = \frac{cr^2}{\pi\mu_0} |\beta_\omega|^2 = \frac{|j_z(\omega)|^2}{4\pi\epsilon_0 c} \frac{\rho_0^4 \sin^2 \theta}{(1 - \cos \theta)^2} \sin^2 \left( \frac{L\omega}{2c} (1 - \cos \theta) \right).$$

In this process, the THz emitted energy has been shown to follow the square of the laser pulse energy. The central frequency of the emission corresponds to the plasma frequency and has a broad low frequency tail decreasing as  $\omega^{-2}$ . Furthermore, in this model, the radial emission of THz reported earlier, simply becomes a lobe of the emitted pattern. The cone of emission constitute the main lobes, while the perpendicular emission is a subsidiary lobe. The opening angle of the main lobe of emission is dependent on the following relation  $\theta \approx \sqrt{\lambda/L}$ . For more details about calculations, I invite the reader to consult the following review [27]. Consequently, at the beginning of my thesis, the state of knowledge concerning the THz emission from a single color filament can be resumed with the schematic presented on Figure 22.

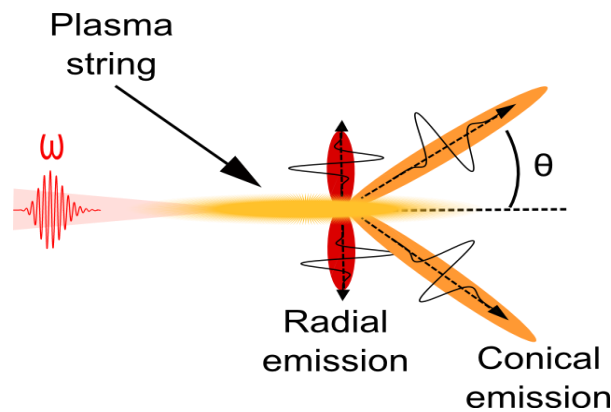


**Figure 22: Schematic representation of the THz emission from a single color filament**

#### b) On-axis emission

In the previous section, a review of the existing theoretical and experimental work on THz emission from a single color filament was presented. Nevertheless, shortly after the report of the Cherenkov-like emission model, a complementary publication appeared in the literature. In this paper, the authors reported the measurement of elliptically polarized THz pulses from a single color filamentation scheme [28]. Using a time domain approach and a short distance focusing length, the authors demonstrated that the polarization from a short and single color filament does not follow a radial polarization as presented in the model of D'amico et.al. This report only concentrates on the polarization analysis, which does not clearly identify the origin of the reported emission.

Furthermore, a recent theoretical report [29] mentioned that the contribution from a transverse ionization electric current can be much larger than the electric current driven by the usual ponderomotive forces. This effect is due to two factors. Firstly, the average degree of ionization decreases with distance from the centre of the laser pulse in the transverse direction. Secondly, the electrons obtain a negative velocity after the laser pulse passes. This leads to an asymmetry in the spatial distribution of electrons creating a transient transversal electrical current. This theoretical approach has similarities with one of the models which describe the THz emission from a two-color filament that will be presented in the next section. Both models attribute the generation process to the

creation of a transverse electrical current, which in the case of the two-color filament is due to the ellipticity of the fundamental laser beam leading to an asymmetry of the ionized field [30].

Even though recent results [28] have been presented in a controversial manner, from literature it would be expected to experimentally observe the existence of different types of emissions having different spatial properties. Consequently, we led our own investigation and measured the angular diagram of emission from a single color filament.

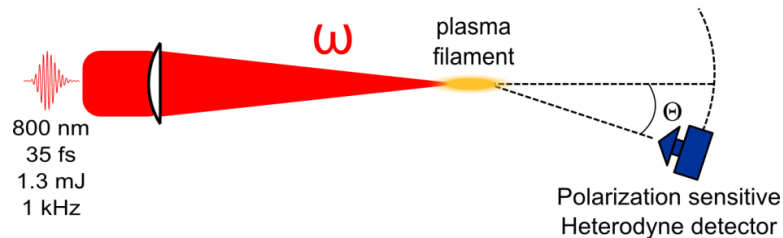


**Figure 23: experimental approach for measurement of THz angular diagram of emission from a single color filament**

As presented in Figure 23, a laser beam was focused in normal atmospheric conditions with a 200 mm positive lens. Hence a single color filament was produced and using the heterodyne detector described in the introductory chapter, we realized the spatial mapping of the THz emission.

Figure 24 presents the data measured while focusing 2mJ of laser power in air. One can clearly see the existence of a conical emission with an opening angle of 40 degrees and an on-axis emission which is 6 times larger than the conical one in the other plane of polarization. It is important to note here, that the on-axis emission has only been obtained when a half-wave plate was introduced in the path of the laser beam Figure 24(a). The optical axis of the wave-plate was aligned with the laser beam polarization, hence leaving its polarization unchanged. Once this half-wave plate was removed, we could only observe the conical emission from the single color filament, Figure 24(b). Using the model described in [25], we calculated the expected length of the filament at a frequency of 0.44 THz and an opening angle,  $\theta$ , of 20 degrees. Simulations, which are presented in Figure 25(a), indicate that the expected filament length should be 4.5 mm. The actual plasma string size was measured using a plasma conductivity technique [15]. This technique will be described in more details in the following chapter.

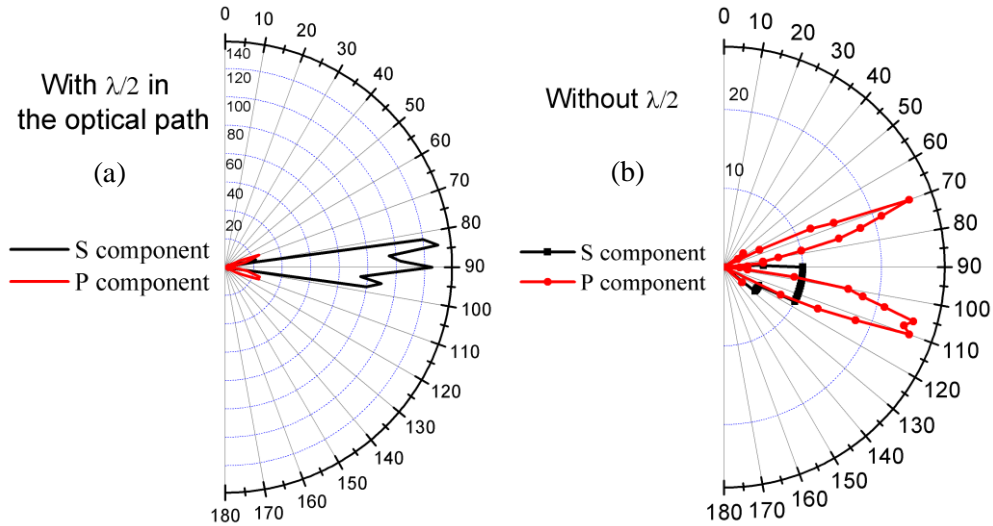


**Figure 24: Measured THz angular emission from single color filament, (a) with a half-wave plate in the optical path, (b) without a half-wave plate in the optical path.**

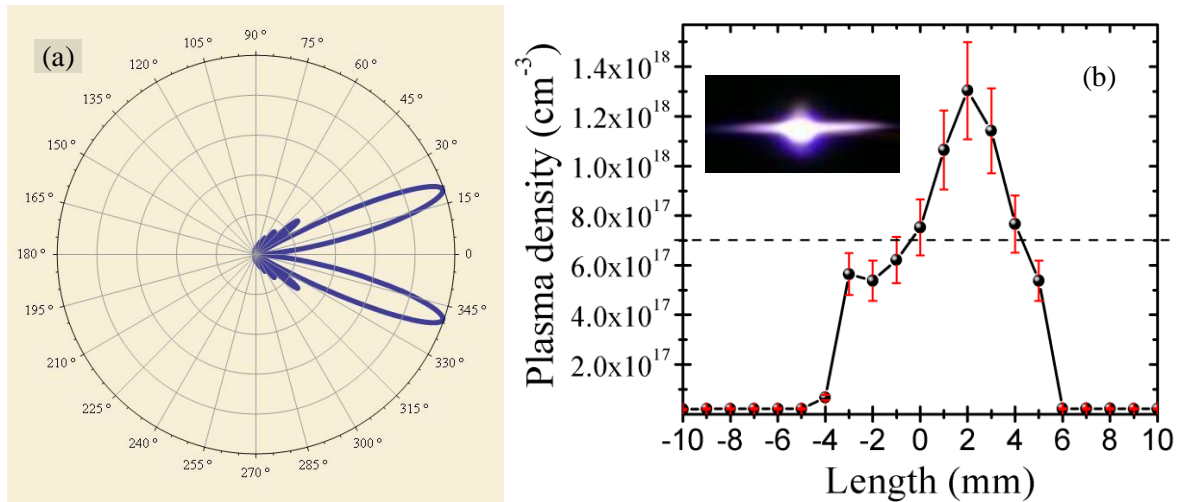


**Figure 25: (a) Calculated diagram of emission based on model equation of D'Amico et al. (b) Measured electron density of a single color filament, with input laser pulse energy of 2 mJ at 800 nm and 35 fs. The inset shows a CCD picture of the filament fluorescence taken with conventional photographic camera.**

The result is plotted in Figure 25(b) where a CCD image of the filament is also presented in an inset. The first observation from Figure 25(b) is that the measured plasma length of around 1 cm does not match the calculated one. More interestingly, a closer look at the CCD image, with an integrated scale, shows that a length of 4.5 mm corresponds to the plasma string fluorescence. Consequently, if one relates this length to the measured plasma string density over this distance, it corresponds to an estimated level of electron density above  $7.5 \times 10^{17} \text{ cm}^{-3}$ . At such a level of electron density, the plasma string may simply act as a mirror for the THz [31, 32], which in turn may have prevented the authors of [25] to measure on-axis emission at 94 GHz. Our observations would also

directly explain why the authors of [28] observed an elliptically polarized THz radiation after collecting the emission from a single filament with a pair of parabolic mirrors.

The on-axis emission must be the result of a transient transversal current that is either caused by ponderomotive forces or an asymmetry in the ionizing field. It is important to remind here, that the on-axis emission was only measured with the presence of a half-wave plate before the focusing lens. This gives another insight into the photocurrent nature of this emission, since the insertion of a birefringent element within the optical path may result in the formation of a transversal asymmetry within the ionized field [29]. This should lead to an on-axis emission of THz pulses, in a similar manner to the emission from a 2-color filament. Using our time domain electro-optic setup, we have recorded the THz emitted electric field from both approaches (see Figure 26). Aside from the fact than a two-color filament yields more THz power, striking similarities are observed between the two techniques. For both levels of input laser energy, the shapes of the recorded electric fields are similar. Furthermore, as the level of input laser energy is decreased, the polarity of the pulse looks inverted, a phenomenon which occurs for both approaches.

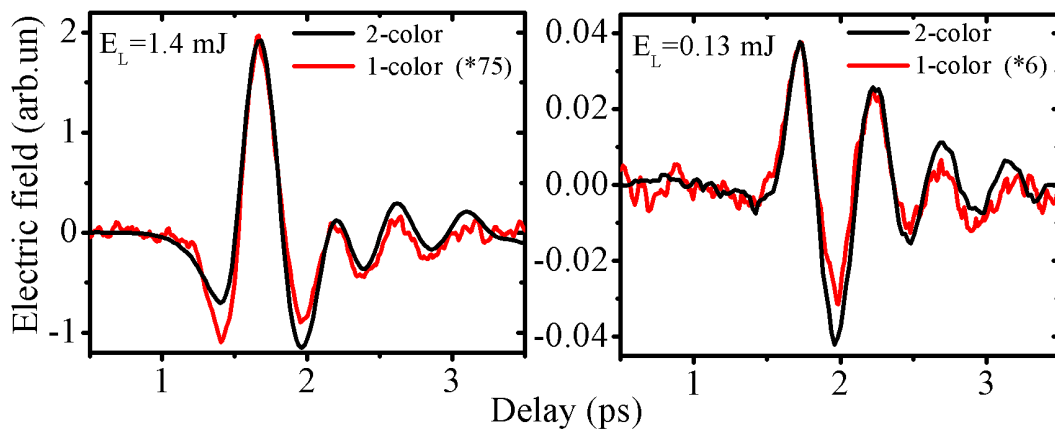


**Figure 26: Measured THz electric field for both single and 2 color filamentation approaches at two different level of input laser pulse energy.**

Finally, the measured electric field from a single color filament cannot originate from the conical emission. Indeed, if one considers the opening angle of emission ( $\theta = 20^\circ$ ) and the focal length of the collecting optic (100 mm), the conical emission can simply not be collected by the 2 inches diameter parabolic mirror.

In conclusion, in this section we have shown the existence of an on-axis THz emission from a single color-filament. This emission is much stronger than the well documented Cherenkov like emission. It results from a transverse photocurrent which has been shown theoretically to emerge from an asymmetry in the ionization field. An updated schematic of the angular diagram of radiation from a single color-filament is presented in Figure 27.

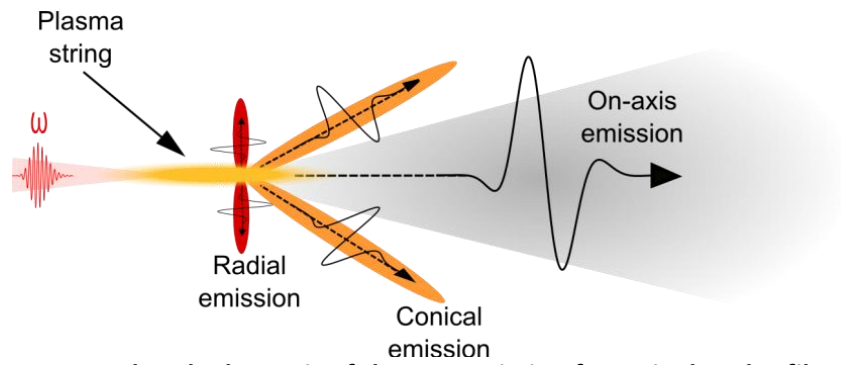


**Figure 27: Updated schematic of the THz emission from single color filament.**

## II.2.2. THz emission from two color filament

### a) The genesis of a controversy

As presented in the previous section, a debate concerning the emission from a single color filament animated the community throughout the years. Another debate which has been even stronger was raised about the two color filament approach. The first report of the use of a two color scheme is dated from 2000 [19]. In this report, the authors used rather low input laser pulse energy of 150  $\mu\text{J}$ , for 65 fs pulse duration at 800 nm. After focusing the fundamental beam, they placed a  $\beta$ -Barium Borate ( $\beta$ -BBO) crystal (100 $\mu\text{m}$  thick) in the beam path, in order to partially double it in frequency, as presented in Figure 28. An intuitive view of the experimental setup suggests that a third order nonlinear phenomenon known as four-wave mixing (FWM) is responsible for the emission. By changing the phase dependence between the two laser fields, the yielded THz output was found to follow a cosine function as the phase between  $\omega$  and  $2\omega$  is tuned. Nevertheless, in the same article the authors measured the THz output dependence on the intensity of  $\omega$  and  $2\omega$ . From a four-wave mixing approach, the yielded THz energy should quadratically follow the intensity of the fundamental pulse. A discrepancy was found since the THz energy follows the cube of the intensity, suggesting the existence of another process leading to this hyperpolarizability.

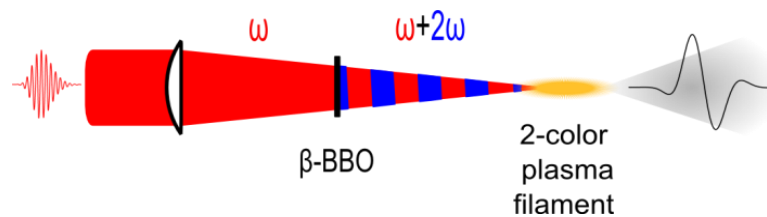


**Figure 28: Experimental approach of two-color filamentation**

Despite the promises foreseen by the first experimental result, this source has been neglected for some years. It was re-investigated four years later in 2004 by Kress et al [33]. Once the authors modeled the emitted THz with the four wave mixing approach, they found a discrepancy of 2 orders of magnitude using the third order susceptibility of the air for the calculation. Consequently the THz yielded with this approach was compared with the THz yielded once they applied a DC voltage in the vicinity of the plasma [18]. For both cases, the THz radiation starts to be generated for the same input laser pulse energy of 35  $\mu\text{J}$  with a 100 mm focal length. This laser energy level corresponds to an intensity of  $1.5 \times 10^{13} \text{ W/cm}^2$  which is the ionization threshold of air [34]. This work demonstrated the existence of ionization threshold dependence for the generation of THz and triggered a debate within the community.

Two more important publications reinforce the confusion regarding the nature of this emission. The first demonstration of a direct coherent control on the emitted THz from plasma in air [35], is clearly attributed to the emission from a four wave mixing process. In this paper, the two laser fields were separated before being recombined. In this way they could directly control the polarization

of  $\omega$  and  $2\omega$ , and the main components of the third order tensor responsible for the emission were identified. The authors clearly demonstrated that the phase between  $\omega$  and  $2\omega$  follows a cosine function as predicted from the equation of THz emission through FWM:

$$E_{THz}(t) \propto \chi^{(3)} E_{2\omega}(t) E_{\omega}^*(t) E_{\omega}^*(t) \cos(\varphi).$$

The dependence on the relative laser pulses energy (below 200  $\mu\text{J}$ ) was investigated. At relatively low laser pulse input power, the THz emission was shown to increase linearly with 800 nm pulse intensity and followed the square root of the 400 nm beam intensity, as predicted from the following equation:

$$E_{THz}(t) \propto \chi^{(3)} \sqrt{I_{2\omega} I_{\omega}} \cos(\varphi).$$

A year after the report on coherent control on the THz generation from plasma in ambient air, a new model was developed. This model states that for appropriate phase between the  $\omega$  and  $2\omega$ , the synthesized laser electric field formed will be asymmetric and strip off the free electrons towards the same direction. Hence, a net transverse plasma current is formed which radiates frequencies in the THz range. For this model the synthesized laser field is:

$$E_L(t) = E_{\omega} \cos \omega t + E_{2\omega} \cos(2\omega t + \theta).$$

Once the electrons are ionized, the external laser electric field accelerates them at a velocity of:

$$v(t) = -(e/m_e) \int_{t'}^t E_L(t) dt.$$

The electrons do not only oscillate with the laser electric field, but they also experience a drift at the above velocity, with an initial velocity equal to 0:

$$v_d(t') = \frac{eE_{\omega} \sin(\omega t')}{m_e \omega} + \frac{eE_{2\omega} \sin(2\omega t' + \theta)}{2m_e \omega}.$$

Consequently at a phase equal to  $\pi/2$ , the symmetry is broken and a net current is formed. This current can be calculated with the following equation:

$$J_{\perp}(t) = \int_{t_0}^t e v_e(t, t') N_e(t) dt',$$

where  $N_e$  is the electron density calculated from the ionization rate equation. Finally the THz radiated field can be derived from the electron current density:

$$E_{THz} \propto \frac{dJ_{\perp}(t)}{dt} = e \frac{dN_e(t)}{dt} v_d(t).$$

This 1-D photocurrent model is in radical contrast with the FWM model. Indeed, it requires a relative phase of  $\pi/2$  for the maximum THz emission, while it needs to be equal to 0 in the case of FWM. Since the experimental data illustrate either one or the other phase dependence, the community has not been able to agree on a definite model. This doubt, which partially remains, is due to a historical mistake made within the field. Indeed, all the reported experiments have been made with

polarization sensitive detectors, which, as we will see in the next section, have considerably limited the possibility to fully characterize the phenomenon responsible for the emission.

### b) Coherent control of THz pulses polarization

Part of the doubt concerning the main mechanism behind the emission of THz pulses from two-color filament has been clarified recently. Two publications have demonstrated that the polarization of the emitted THz radiation can be controlled through the trajectory of the new born electrons within the two-color plasma field [30, 36]. In both reports, a full ( $2\pi$ ) rotation of the THz pulse polarization was achieved while keeping the amplitude of the THz pulses constant. These interesting results were obtained via the direct control on the phase between the  $\omega$  and  $2\omega$  laser fields, either through the positioning of the BBO crystal along the laser propagation axis  $z$  [30] or using an accurate attosecond phase controller [36]. According to [36], the rotation of the THz polarization is only possible when at least one the laser fields is elliptically polarized. In a classic arrangement like in [30], where there is no possibility to play on each laser beam polarization, the ellipticity is gained by the fundamental laser beam within the frequency doubling crystal. The model developed in [30] is in the continuity of the 1-D photocurrent model, except that a new dimension is brought to the analysis. In the first photocurrent model, the field projection on the  $x$ -axis has been considered as the driving field for THz generation. According to the authors of [30], it is rather the  $y$  component, which is generated by the birefringence in the BBO, that liberates the ionized electrons. They are then drifted along the  $x$  axis to other directions in the transverse plan. This literally means that the phase of the synthesized two-color laser field controls the direction of the new born electron, which in turn influences the polarization of the emitted THz pulses as presented on Figure 29. In this model, only the initial laser field equation differs since it considers a new projection on the  $y$  axis:

$$E_L(t) = E_\omega(t)(\cos(\omega t + \Gamma) \cos \alpha \hat{x}' + \cos(\omega t \sin \alpha \hat{y}')) + E_{2\omega}(t) \cos(2\omega t + \varphi)(\cos \alpha \hat{x} + \sin \alpha \hat{y}).$$

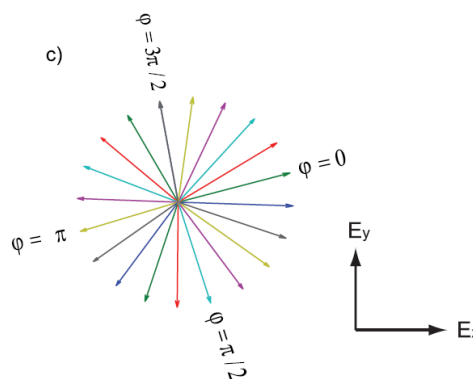


**Figure 29: Calculation of the electrons trajectory dependence on the synthesized field phase. (Ref. [30]).**

Based on the results of the above studies, we were expecting to achieve similar THz polarization control when changing the two-color filament medium gas pressure. The change of

pressure will induce a wavelength dependent change of the refractive index, which in turn will affect the phase of the synthesized laser field. Thus, a direct coherent control on the emitted THz pulse polarization will be achieved. In the past, some studies have been performed exploring the effect that different gas species, at various pressures, have on the THz emission [37-40]. Though, no one had studied in detail the possible control this can offer on the THz polarization properties.

To gain control on the filament surrounding gas pressure and obtain a complementary proof of the photocurrent nature of the THz emission, we have built a gas cell as presented in Figure 30.

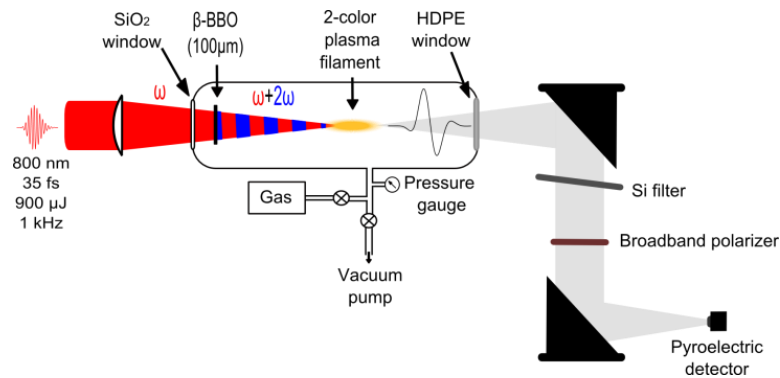


**Figure 30: Experimental approach for the pressure study.**

The gas cell is made out of a fused silica plate of 2 mm thickness as the input window; the rear window consists of a 3mm thick high density polyethylene (HDPE). The transmission property of the rear window has been measured using an FTIR spectrometer. This HDPE window shows a cut-off frequency at 20 THz as presented in Figure 31. The emitted THz radiation is collected and refocused onto a broadband (0.1 to 30 THz) thermal pyroelectric detector, with a pair of parabolic mirrors through non purged air. An extra silicon wafer with 1 mm thickness was placed between the two parabolas to cut the small fraction of remaining optical light. A broadband THz polarizer is used to conduct the polarization analysis with constant degree of polarization (>99.5%) over a broad frequency range (0.1-20 THz).

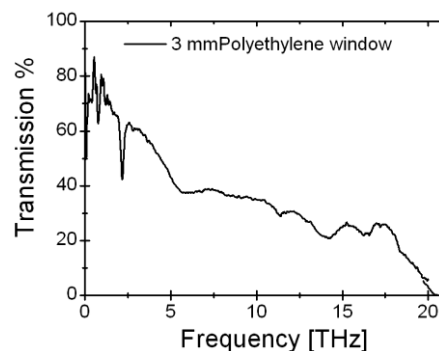


**Figure 31: Transmission spectrum of the gas cell exit window (polyethylene) recorded with FTIR.**

With the above described experimental arrangement, we performed a systematic study for nitrogen over a pressure range spanning from 10 mbar to 1 bar and for input laser energy of 240 μJ.

At this level of laser energy, the plasma string remains relatively short and the phase walk-off occurring in the plasma channel can be neglected. The results are presented in Figure 32.

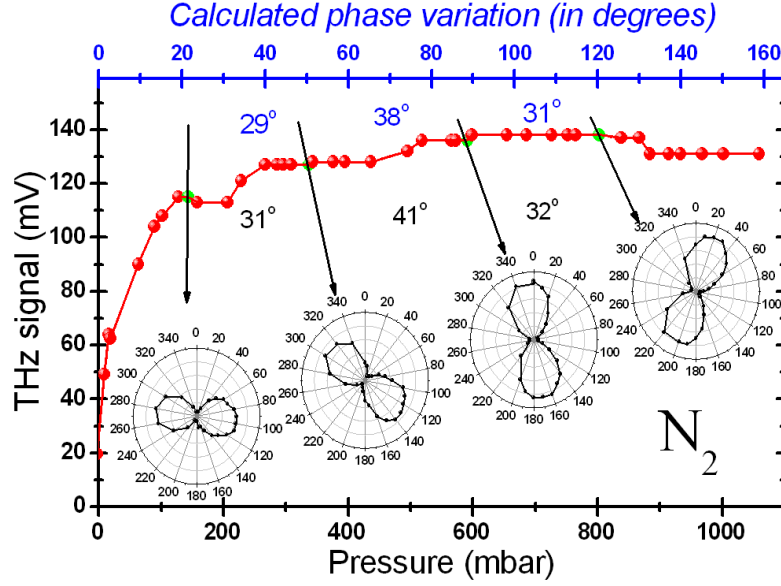


**Figure 32: Detected THz power as function of nitrogen gas pressure (Dots and black curve) and THz pulse polarization state at different pressure levels. The upper axis (blue colored) represents the calculated phase variation.**

First, one can notice that the emission of THz pulses can be divided in two distinct regimes. There is a first regime for pressure below 100 mbar where the THz radiation increases linearly with the gas density. In this low pressure regime, as it was already reported in [37], the gas medium is fully ionized while the degree of plasma defocusing is relatively low. On the other hand, at gas pressures higher than 100mbar, the plasma defocusing becomes dominant [37] and the total emission of THz is relatively constant over the whole pressure range. More importantly, the polarization measurements of the emitted THz pulse show a  $\pi/2$  polarization rotation over 650 mbar of the gas medium pressure with quasi constant THz power and linear pulse polarization. As we mentioned previously the change of the surrounding gas pressure systematically leads to a change of the relative dispersion between the two laser fields. In turn, this change in refractive index leads to a change in the relative phase between  $\omega$  and  $2\omega$ ,  $\Delta\varphi = \omega d(n_\omega - n_{2\omega})/c$ . Thus, one can accurately predict the change in the dispersion using the pressure dependent Sellmeier equation [41]:

$$n^2(\lambda) - 1 = \left( \frac{B_1\lambda^2}{\lambda^2 - C_1} + \frac{B_2\lambda^2}{\lambda^2 - C_2} + \frac{B_3\lambda^2}{\lambda^2 - C_3} \right) \frac{P}{P_0} \cdot \frac{T_0}{T}.$$

The Sellmeier coefficients used for the calculations can be found in [42]. Knowing the phase variation induced by the pressure change, we related it with the state of polarization of the THz pulse at different pressure. As one can see from Figure 32, the estimated phase variation (blue figures) is in good agreement with the rotation angle of the THz pulse. Furthermore, one could expect that the phase variation varies with the gas species, and consequently expect a bigger polarization rotation

over the same pressure range as the atomic number of the gas increases. It is also important to note that the results differ once we used higher laser pulse energy. This is mainly due to an extension of the filament length, where the phase walk-off becomes non-negligible. A detailed study of the drawbacks and advantages linked to this plasma string extension is presented in the next chapter.

### II.2.3 Characterization of the source

Using our time domain spectroscopy in combination with our various detectors, we have characterized the THz radiation emitted from a 2-color filament. The achievable bandwidth, electric field strength and size of the focused beam are presented.

#### a) Bandwidth

Using different electro-optic crystals, we have measured the emitted electric field. Using a 1 mm thick ZnTe crystal, a useful bandwidth extending up to 3 THz has been measured as presented in Figure 33. The measured bandwidth is similar to the one reported in the previous chapter and based on the emission from a ZnTe crystal. Nevertheless, using a thinner electro-optic crystal, 100  $\mu\text{m}$  GaP, frequencies up to 7 THz have been measured (see Figure 33). This improvement of bandwidth is considerable and clearly demonstrates the inherent bandwidth limitation of a thick detection crystal.

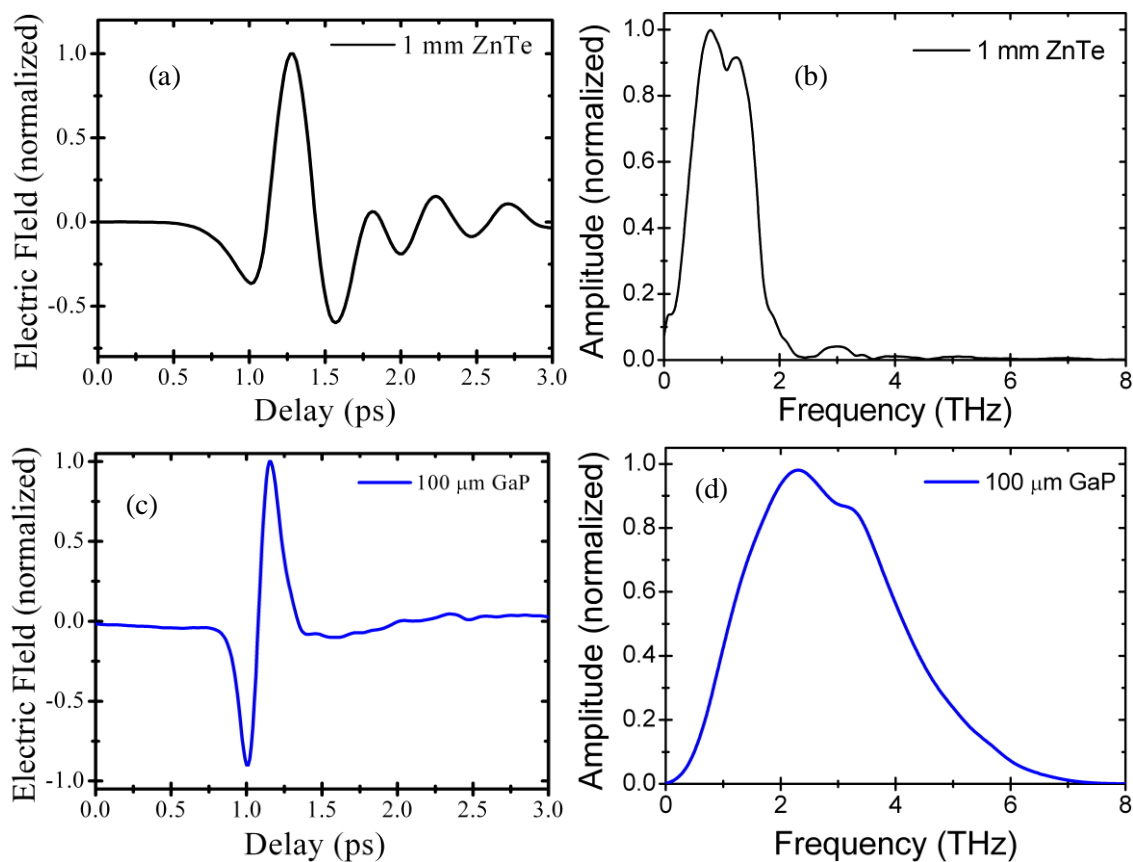


**Figure 33: (a) Measured THz electric field and (b) its Fourier transform for a 1 mm ZnTe crystal. (c) Measured THz electric field and (d) its Fourier transform for a 100  $\mu\text{m}$  GaP.**

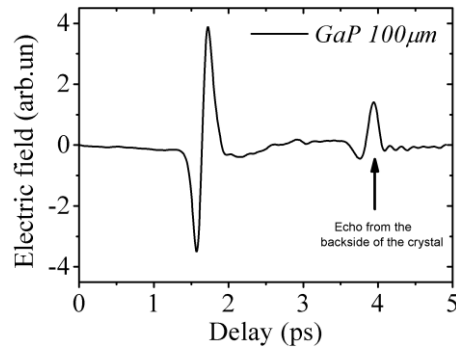


**Figure 34: Extended time domain trace for 100  $\mu\text{m}$  GaP detecting crystal.**

A first echo of the THz pulse, which aroused from Fabry-Perot internal reflection within the GaP crystal, can be seen once we extended the time window measurement (Figure 34). This constitutes a serious drawback if one wants to use this crystal for spectroscopic measurements. A solution in order to circumvent this effect consists of contacting the detection crystal to a thicker crystal cut along a neutral axis (e.g. [101]). As presented above, the measured THz electric field depends on the crystal used for the measurement. In order to get a real view of the emitted field other experimental techniques could have been subject of investigation. First, the THz pulse duration, could have been measured more accurately, using a classic Michelson interferometer. The drawback of this approach is that only the convolution of the THz field envelope is obtained instead of its electric field. Thus, one loses the phase information. Another approach that has been developed in the last couple of years, is based on the cross term mixing within a second plasma string [43]. This technique allows recording the electric field of the THz radiation and will be discussed in more details at the end of this thesis. This technique demonstrates that the THz bandwidth of pulses emitted from 2-color filaments extend all over the THz range (from 0.3 to 30 THz).

#### b) Beam size

Using a knife edge technique, we have been able to obtain an estimate of THz beam diameter at the focus of a parabolic mirror. The experimental approach consists of a razor blade scanned across the focused THz beam. Our pyroelectric detector was used to measure the THz power.

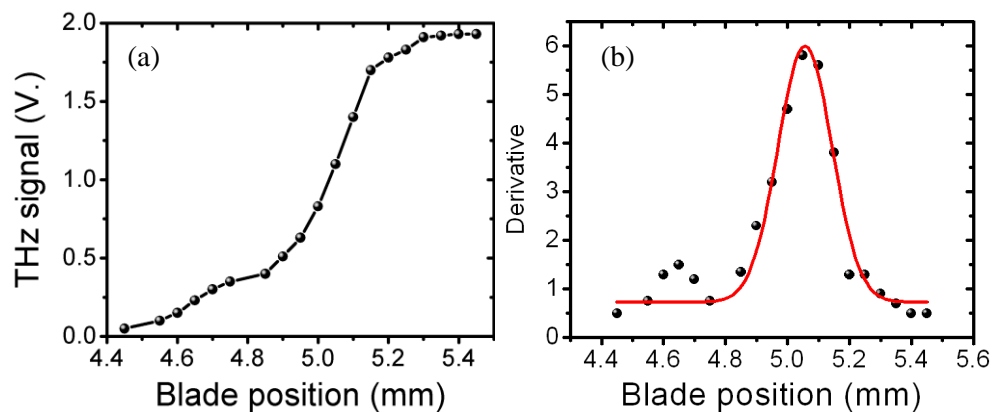


**Figure 35: (a) Measured THz signal using knife edge technique and (b) its derivative.**

Figure 35(a) presents the experimental results. In order to obtain the beam profile from the knife-edge measurement, one needs to derivate the measured data. Figure 35(b) shows the result of the derivation. Assuming a Gaussian pulse, the extracted full width half maximum (FWHM) from the fitting is equal to 205  $\mu\text{m}$ . This size corresponds to a diffraction limited spot for a THz spectrum pointing at 1.7 THz, which is in good agreement with the spectra presented above. The  $1/e^2$  diameter is equal to 435  $\mu\text{m}$  according to the measurement. Furthermore, the size of the collimated beam after the first parabolic mirror has been estimated to be equal to 40 mm.

### c) Electric field strength

An estimation of the THz peak electric field can be directly deduced from the time domain trace, the measured energy and the estimation of the focused beam diameter using the following formula [44]:

$$E_{THz} = \sqrt{\frac{\eta_0 W}{\pi w_1^2 \int g^2(t) dt}} .$$

$W$  is the THz pulse energy,  $w_1$  is the measured beam waist and  $g(t)$  is the temporal shape of the THz electric field with peak value normalized to 1.  $\eta_0$  is the free space impedance (377  $\Omega$ ). Using our pyroelectric detector, we have measured a THz pulse energy of 78 nJ for an input laser pulse energy of 1.35 mJ. Using the estimated THz beam waist as well as the calculated integral of the electric field temporal shape (Figure 33(a)), we arrive to an estimated electric field of 130 kV/cm. Such a value is too high compared to the one reported in [37], for a measurement with a 1 mm thick ZnTe. The problem lies in the fact that the pyroelectric detector measures the power over the whole bandwidth, while the electro-optic sampling measurement with the ZnTe crystal only resolves a part of the bandwidth. To obtain a more accurate value of the electric field, the energy of the beam has been measured while inserting a Teflon filter in the THz beam path. Teflon has a cut-off frequency at 5 THz, which matches the spectrum of the recorded THz pulse with the ZnTe. Using such a filter, we measured a THz pulse energy of 8.5 nJ, which in turn gives a THz electric field of 42 kV/cm. This value is closer to the one reported in [37]. Using the time trace measured with the thin GaP crystal (Figure 33(a)) and the full bandwidth measurement of the energy, the THz electric field is estimated to be equal to 202 kV/cm. This time, the estimated value of the electric field is smaller than the one reported from a similar approach [45].

Another approach for the estimation of the THz peak electric field is to directly use the modulation value of the probe beam, which has been recorded with the electro-optic detector [46]. The formula shown below relates the measured modulation of the probe with the phase shift and the THz electric field:

$$\frac{A - B}{A + B} = \frac{2\pi}{\lambda} n_0^3 r_{41} E_{THz} L ,$$

where A and B stand for the values measured on each photodiodes at the THz electric field peak.  $n_0$  is the refractive index of the crystal at  $\lambda=800$  nm, L is its thickness and  $r_{41}$  is the electro-optic coefficient of the crystal. The value for the most popular crystals used in the field are available in [47]. For the 1 mm ZnTe crystal we have an estimated electric field of 36 kV/cm, which is close to our previous estimation. For the GaP crystal, the estimated electric field value is equal to 175 kV/cm. For comparison, the electric field presented in chapter I and emitted from a 0.5 mm ZnTe crystal was estimated to be equal to 1.5 kV/cm, using the direct estimation from the balanced detection.

#### d) Angular diagram of emission

Finally and in a similar approach to the one presented in the previous section for the single color filamentation, we have also measured the angular diagram of emission from a 2-color filament (see Figure 36). The input laser pulse energy was equal to 1.5 mJ. The heterodyne detector was placed at 10 cm from the end of the filamentary structure. The spatial mapping of the emission clearly shows that most of the radiation is released on-axis. This result further confirms that the 2-color emission is emitted from a transversal photocurrent rather than a longitudinal current which shows a conical shape of emission.

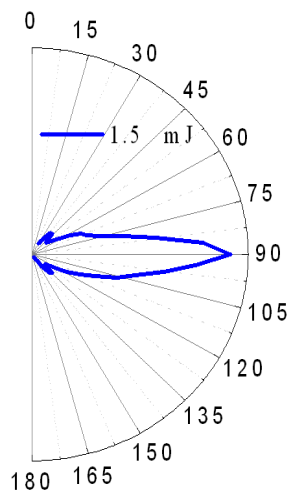


**Figure 36: Angular diagram of emission from a two-color filament approach with 1.5 mJ input pulse energy.**

In conclusion, we have shown in this section a new proof of the photocurrent nature of the 2-color filament generation process. Furthermore using the various measurement tools at our disposition, we have characterized the main attributes of the source. It is, in accordance with the literature, one of the most powerful table-top THz sources.

## II.3/ Chapter conclusions

In this chapter, the existing literature concerning the THz emission from filaments has been presented. Our experimental data have shown, for the first time to our knowledge, the existence of an on-axis emission from a single-color filament. Few experimental evidences let us presume that a transient transversal photocurrent within the plasma string is responsible for this emission. We have also explored in details the THz emission from a two-color filament. In accordance with recent publications [30, 36], we have shown that the polarization of the emitted THz pulses is controlled by the relative phase between the two laser fields [48]. Furthermore, the 2-color filament source has been characterized. At high level of input laser energy, the strength of the 2-color source is by 2 orders of magnitude higher than the single color one. In comparison with the experimental data from chapter I, it is clear that the strength and the bandwidth of the 2-color source overcome by far the one of the optical rectification. Finally, few experimental observations have suggested that the source can be optimized further. Thus, in the following chapter, we present our investigations concerning the effect of filamentation tailoring on the emission of THz pulses.

## References

1. D. Strickland and G. Mourou, "Compression of amplified chirped optical pulses," *Optics Communications* 56, 219-221 (1985).
2. A. Braun, G. Korn, X. Liu, D. Du, J. Squier, and G. Mourou, "Self-channeling of high-peak-power femtosecond laser-pulses in air," *Optics Letters* 20, 73-75 (1995).
3. A. Couairon and A. Mysyrowicz, "Femtosecond filamentation in transparent media," *Physics Reports-Review Section of Physics Letters* 441, 47-189 (2007).
4. D. Aumiler, T. Ban, and G. Pichler, "Femtosecond laser-induced cone emission in dense cesium vapor," *Phys. Rev. A* 71, 6 (2005).
5. D. Faccio, A. Averchi, A. Lotti, P. Di Trapani, A. Couairon, D. Papazoglou, and S. Tzortzakis, "Ultrashort laser pulse filamentation from spontaneous XWave formation in air," *Opt. Express* 16, 1565-1570 (2008).
6. C. P. Hauri, W. Kornelis, F. W. Helbing, A. Heinrich, A. Couairon, A. Mysyrowicz, J. Biegert, and U. Keller, "Generation of intense, carrier-envelope phase-locked few-cycle laser pulses through filamentation," *Applied Physics B: Lasers and Optics* 79, 673-677 (2004).
7. A. Couairon, M. Franco, A. Mysyrowicz, J. Biegert, and U. Keller, "Pulse self-compression to the single-cycle limit by filamentation in a gas with a pressure gradient," *Opt. Lett.* 30, 2657-2659 (2005).
8. P. Rairoux, H. Schillinger, S. Niedermeier, M. Rodriguez, F. Ronneberger, R. Sauerbrey, B. Stein, D. Waite, C. Wedekind, H. Wille, L. Wöste, and C. Ziener, "Remote sensing of the atmosphere using ultrashort laser pulses," *Applied Physics B: Lasers and Optics* 71, 573-580 (2000).
9. J. Kasparian, R. Sauerbrey, D. Mondelain, S. Niedermeier, J. Yu, J. P. Wolf, Y. B. André, M. Franco, B. Prade, S. Tzortzakis, A. Mysyrowicz, M. Rodriguez, H. Wille, and L. Wöste, "Infrared extension of the super continuum generated by femtosecond terawatt laser pulses propagating in the atmosphere," *Opt. Lett.* 25, 1397-1399 (2000).
10. G. Méchain, C. D'Amico, Y. B. André, S. Tzortzakis, M. Franco, B. Prade, A. Mysyrowicz, A. Couairon, E. Salmon, and R. Sauerbrey, "Range of plasma filaments created in air by a multi-terawatt femtosecond laser," *Optics Communications* 247, 171-180 (2005).
11. J. Kasparian, M. Rodriguez, G. Mejean, J. Yu, E. Salmon, H. Wille, R. Bourayou, S. Frey, Y.-B. André, A. Mysyrowicz, R. Sauerbrey, J.-P. Wolf, and L. Wöste, "White-Light Filaments for Atmospheric Analysis," *Science* 301, 61-64 (2003).
12. S. Tzortzakis, B. Prade, M. Franco, A. Mysyrowicz, S. Hüller, and P. Mora, "Femtosecond laser-guided electric discharge in air," *Physical Review E* 64, 057401 (2001).
13. S. Tzortzakis, L. Sudrie, M. Franco, B. Prade, A. Mysyrowicz, A. Couairon, and L. Bergé, "Self-Guided Propagation of Ultrashort IR Laser Pulses in Fused Silica," *Phys. Rev. Lett.* 87, 213902 (2001).
14. K. M. Davis, K. Miura, N. Sugimoto, and K. Hirao, "Writing waveguides in glass with a femtosecond laser," *Opt. Lett.* 21, 1729-1731 (1996).
15. S. Tzortzakis, M. A. Franco, Y. B. André, A. Chiron, B. Lamouroux, B. S. Prade, and A. Mysyrowicz, "Formation of a conducting channel in air by self-guided femtosecond laser pulses," *Physical Review E* 60, R3505 (1999).
16. D. G. Papazoglou and S. Tzortzakis, "In-line holography for the characterization of ultrafast laser filamentation in transparent media," *Applied Physics Letters* 93, 041120-041123 (2008).

17. H. Hamster, A. Sullivan, S. Gordon, W. White, and R. W. Falcone, "Subpicosecond, electromagnetic pulses from intense laser-plasma interaction," *Phys. Rev. Lett.* 71, 2725 (1993).
18. T. Löffler, F. Jacob, and H. G. Roskos, "Generation of terahertz pulses by photoionization of electrically biased air," *Applied Physics Letters* 77, 453-455 (2000).
19. D. J. Cook and R. M. Hochstrasser, "Intense terahertz pulses by four-wave rectification in air," *Opt. Lett.* 25, 1210-1212 (2000).
20. C.-C. Cheng, E. M. Wright, and J. V. Moloney, "Generation of Electromagnetic Pulses from Plasma Channels Induced by Femtosecond Light Strings," *Phys. Rev. Lett.* 87, 213001 (2001).
21. S. Tzortzakis, G. Mechain, G. Patalano, Y. B. Andre, B. Prade, M. Franco, A. Mysyrowicz, J. M. Munier, M. Gheudin, G. Beaudin, and P. Encrenaz, "Coherent subterahertz radiation from femtosecond infrared filaments in air," *Optics Letters* 27, 1944-1946 (2002).
22. S. Tzortzakis, G. Méchain, G. Patalano, M. Franco, B. Prade, and A. Mysyrowicz, "Concatenation of plasma filaments created in air by femtosecond infrared laser pulses," *Applied Physics B: Lasers and Optics* 76, 609-612 (2003).
23. G. Méchain, T. Olivier, M. Franco, A. Couairon, B. Prade, and A. Mysyrowicz, "Femtosecond filamentation in air at low pressures. Part II: Laboratory experiments," *Optics Communications* 261, 322-326 (2006).
24. P. Sprangle, J. R. Peñano, B. Hafizi, and C. A. Kapetanacos, "Ultrashort laser pulses and electromagnetic pulse generation in air and on dielectric surfaces," *Physical Review E* 69, 066415 (2004).
25. C. D'Amico, A. Houard, M. Franco, B. Prade, A. Mysyrowicz, A. Couairon, and V. T. Tikhonchuk, "Conical forward THz emission from femtosecond-laser-beam filamentation in air," *Phys. Rev. Lett.* 98(2007).
26. J. Zheng, C. X. Yu, Z. J. Zheng, and K. A. Tanaka, "Cherenkov radiation generated by a beam of electrons revisited," *Physics of Plasmas* 12, 093105-093106 (2005).
27. C. D'Amico, A. Houard, S. Akturk, Y. Liu, J. Le Bloas, M. Franco, B. Prade, A. Couairon, V. T. Tikhonchuk, and A. Mysyrowicz, "Forward THz radiation emission by femtosecond filamentation in gases: theory and experiment," *New Journal of Physics* 10(2008).
28. Y. Zhang, Y. Chen, C. Marceau, W. Liu, Z. D. Sun, S. Xu, F. Théberge, M. Châteauneuf, J. Dubois, and S. L. Chin, "Non-radially polarized THz pulse emitted from femtosecond laser filament in air," *Opt. Express* 16, 15483-15488 (2008).
29. M. Chen, A. Pukhov, X.-Y. Peng, and O. Willi, "Theoretical analysis and simulations of strong terahertz radiation from the interaction of ultrashort laser pulses with gases," *Physical Review E (Statistical, Nonlinear, and Soft Matter Physics)* 78, 046406-046407 (2008).
30. H. D. Wen and A. M. Lindenberg, "Coherent Terahertz Polarization Control through Manipulation of Electron Trajectories," *Phys. Rev. Lett.* 103, 4 (2009).
31. C. Thauray, F. Quere, J. P. Geindre, A. Levy, T. Ceccotti, P. Monot, M. Bougeard, F. Reau, P. d'Oliveira, P. Audebert, R. Marjoribanks, and P. Martin, "Plasma mirrors for ultrahigh-intensity optics," *Nat Phys* 3, 424-429 (2007).
32. H. C. Kapteyn, M. M. Murnane, A. Szoke, and R. W. Falcone, "Prepulse energy suppression for high-energy ultrashort pulses using self-induced plasma shuttering," *Opt. Lett.* 16, 490-492 (1991).
33. M. Kress, T. Löffler, S. Eden, M. Thomson, and H. G. Roskos, "Terahertz-pulse generation by photoionization of air with laser pulses composed of both fundamental and second-harmonic waves," *Optics Letters* 29, 1120-1122 (2004).

34. S. Augst, D. D. Meyerhofer, D. Strickland, and S. L. Chin, "LASER IONIZATION OF NOBLE-GASES BY COULOMB-BARRIER SUPPRESSION," *J. Opt. Soc. Am. B-Opt. Phys.* 8, 858-867 (1991).
35. X. Xie, J. M. Dai, and X. C. Zhang, "Coherent control of THz wave generation in ambient air," *Phys. Rev. Lett.* 96(2006).
36. J. Dai, N. Karpowicz, and X. C. Zhang, "Coherent Polarization Control of Terahertz Waves Generated from Two-Color Laser-Induced Gas Plasma," *Phys. Rev. Lett.* 103, 023001-023004 (2009).
37. M. D. Thomson, M. Kress, T. Löffler, and H. G. Roskos, "Broadband THz emission from gas plasmas induced by femtosecond optical pulses: From fundamentals to applications," *Laser & Photonics Reviews* 1, 349-368 (2007).
38. Y. Chen, M. Yamaguchi, M. Wang, and X. C. Zhang, "Terahertz pulse generation from noble gases," *Applied Physics Letters* 91, 251116-251113 (2007).
39. K. Y. Kim, A. J. Taylor, J. H. Glowina, and G. Rodriguez, "Coherent control of terahertz supercontinuum generation in ultrafast laser-gas interactions," *Nature Photonics* 2, 605-609 (2008).
40. A. V. Balakin, A. V. Borodin, I. A. Kotelnikov, and A. P. Shkurinov, "Terahertz emission from a femtosecond laser focus in a two-color scheme," *J. Opt. Soc. Am. B* 27, 16-26 (2010).
41. A. Börzsönyi, Z. Heiner, M. P. Kalashnikov, A. P. Kovács, and K. Osvay, "Dispersion measurement of inert gases and gas mixtures at 800 nm," *Appl. Opt.* 47, 4856-4863 (2008).
42. A. Dalgarno and A. E. Kingston, "The Refractive Indices and Verdet Constants of the Inert Gases," *Proc. R. Soc. Lond. A* 259, 424-431 (1960).
43. J. Dai and X. C. Zhang, "Terahertz wave generation from gas plasma using a phase compensator with attosecond phase-control accuracy," *Applied Physics Letters* 94, 021117-021113 (2009).
44. F. Blanchard, G. Sharma, X. Ropagnol, L. Razzari, R. Morandotti, and T. Ozaki, "Improved terahertz two-color plasma sources pumped by high intensity laser beam," *Opt. Express* 17, 6044-6052 (2009).
45. T. Bartel, P. Gaal, K. Reimann, M. Woerner, and T. Elsaesser, "Generation of single-cycle THz transients with high electric-field amplitudes," *Opt. Lett.* 30, 2805-2807 (2005).
46. F. Blanchard, L. Razzari, H. C. Bandulet, G. Sharma, R. Morandotti, J. C. Kieffer, T. Ozaki, M. Reid, H. F. Tiedje, H. K. Haugen, and F. A. Hegmann, "Generation of 1.5  $\mu$ J single-cycle terahertz pulses by optical rectification from a large aperture ZnTe crystal," *Opt. Express* 15, 13212-13220 (2007).
47. X.-C. Zhang and J. Xu, "Generation and Detection of THz Waves," in *Introduction to THz Wave Photonics*, pp. 27-48.
48. J.-M. Manceau, M. Massaouti, and S. Tzortzakis, "Coherent control of THz pulses polarization from femtosecond laser filaments in gases," *Opt. Express* 18, 18894-18899 (2010).

*Chapter III: Optimization of THz pulse  
emission via filamentation tailoring*

<b>CHAPTER III: OPTIMIZATION OF THZ PULSE EMISSION VIA FILAMENTATION TAILORING.....</b>	<b>68</b>
<b>III.1/ Introduction to filamentation tailoring .....</b>	<b>70</b>
<b>III.2/ THz pulse shortening from tailored fs filaments in air. ....</b>	<b>71</b>
III.2.1 A Tailoring approach for the electron density control.....	71
III.2.2 The effect on the THz pulse emission.....	73
III.2.3 Measurement of the electron density.....	74
<b>III.3/ Strong terahertz emission enhancement via filament concatenation in air .....</b>	<b>77</b>
III.3.1 Extension of the plasma length using the concatenation effect .....	77
III.3.2 The effect on the THz pulse emission.....	79
III.3.3 A cross correlation effect.....	80
<b>III.4/ Terahertz polarization state control from tailored femtosecond filaments in air .....</b>	<b>82</b>
III.4.1 Effect of an extended plasma length on the THz polarization control .....	82
III.4.2 A Tailoring approach to circumvent the phase walk-off.....	83
III.4.3 Effect on an extended plasma length the THz polarization state.....	86
<b>III.5/ Chapter conclusions .....</b>	<b>87</b>
References .....	89

### III.1/ Introduction to filamentation tailoring

The concept of filamentation tailoring relates to the use of external parameters in order to obtain the desired laser filamentary structure. As presented in the previous chapter, light filaments have very interesting properties that can be used for various applications. Thus, gaining control on the filamentation process will allow not only a better understanding of this highly nonlinear process but also offer new degrees of freedom and optimization for the filaments' applications. Due to the high intensities reached within a filament, it is impossible to insert optics in order to gain control on the filament process. Consequently, one needs to find external means to obtain control on this process.

Over the years, several reports have presented possibilities to tune the shape of filaments. For example a recent report has shown an extension of a filament length by a factor 5 [1]. The authors simply replaced a positive focusing lens by a combination of diverging lenses with an axicon. Furthermore, using this combination, the length of the filament was shown to be tuneable while keeping a high electron density. In another demonstration, the introduction of amplitude masks in the beam path have proven to be efficient tools for the control of multiple filamentation process [2]. Also, the using a spatial light modulator that can control the spectral phase of the input laser beam has allowed to obtain control on the filament starting position [3]. The field of filamentation tailoring also refers to the interaction of filaments between them. For example, a recent report demonstrated the possibility to form volume plasma density gratings by temporally and spatially overlapping two filaments [4]. This result is of main importance since it offers the possibility to create plasma photonic devices that have no damage threshold and which can be introduced in the path of filaments. Many other effects have been reported in the literature and most of them can be found in the review paper [5].

The aim of this chapter is to present the work that we have done on filamentation tailoring and its effects on the THz pulse emission. We will show that the optimization of the filamentary structure can lead to various effects such as THz pulse shortening, THz pulse enhancement or the production of THz pulses with various polarization states.

## III.2/ THz pulse shortening from tailored fs filaments in air.

### III.2.1 A Tailoring approach for the electron density control.

It is well known that THz emission from plasma depends on the electron density [6]. In most experimental situations, the highly dynamical nature of the filamentation process leads to a non-uniform plasma distribution with strong gradients along the propagation path [7]. At the beginning of this thesis there were no reports on the effect that the plasma density distribution has on the emitted THz radiation. The dependence of the THz radiation emitted from a filament upon the on-axis distribution of the plasma string appeared as a fundamental parameter to investigate. In order to tailor the plasma string and control its uniformity and length, appropriate adjustments of the input laser beam wavefront have been investigated.

First, we investigated the use of an axicon lens which offers the possibility to extend in a uniform manner the electron density once it is combined with a diverging lens. Axicons are commonly used to generate Bessel beams which can be viewed as the superposition of infinite plane waves whose wave-vector lies on a cone as represented in Figure 37(a). Adding a diverging lens before the axicon offers the possibility to tune the size of the Bessel zone as described in [1] and depicted in Figure 37(b). As this conical wave propagates, due to interference effects, an intense central core surrounded by lower intensity rings is formed along the propagation direction (see Figure 37). In the nonlinear regime the high intensity core of the Bessel beam will lead to the generation of free electrons through multi-photon ionization and hence the formation of a filamentary structure.

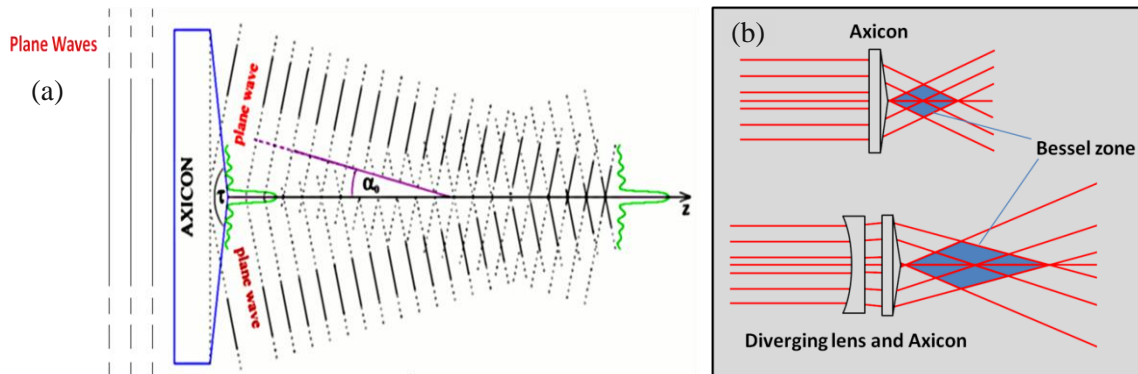


**Figure 37: (a) Schematic representation of a Bessel beam formation with an axicon lens. (b) Schematic representation of a Bessel beam formation with an axicon lens in combination with a diverging lens.**

Using an axicon with an apex angle  $178^\circ$  ( $\tau$  in Figure 37) in combination with a negative lens of -200 mm focal length, we investigated the formation of different filamentary structures. The first observations using this approach suggested that the electron density was too low. Indeed, using 800 nm laser pulse with 35 fs duration and 2.3 mJ input pulse we have not been able to observe the

fluorescence of the filamentary structure. As mentioned in the previous chapter, the THz emission from a two-color filament strongly depends on the electron density. Consequently, the absence of visible fluorescence from the nitrogen molecules of air indicates that the medium is weakly ionized which means that the electron density and the THz emission are low.

Another approach which offers control on the plasma density distribution consists of introducing astigmatism and other wavefront distortions to the laser input pulse. Such techniques have been proven efficient for gaining partial control on the filamentation process. For instance, it has been used for the suppression of multi-filamentation and filamentation stabilization [8]. In the continuity of the previous study, filaments were created in air using a converging lens ( $f = 200$  mm) coupled, in most cases, with the same axicon (apex angle  $178^\circ$ ) placed 130 mm after the first lens, while the BBO crystal is placed  $\sim 3.5$  cm from the focus. The wavefront control was then achieved by tilting one or both optical elements in a combined way as resumed on the schematic of Figure 38. In such a way, the high electron density is preserved as it was possible to directly observe the fluorescence of nitrogen molecules with naked eye.

We then inserted this combination of lenses within our time domain spectroscopy and we studied a number of plasma distributions. The obtained plasma string profiles can be tuned across a wide range. Typical experimental results are shown in Figure 39. These are the images of the different plasma string fluorescence, obtained with a conventional photographic camera. The electric field of the THz pulses emitted from the different plasma profiles have been measured and are presented in the following section.

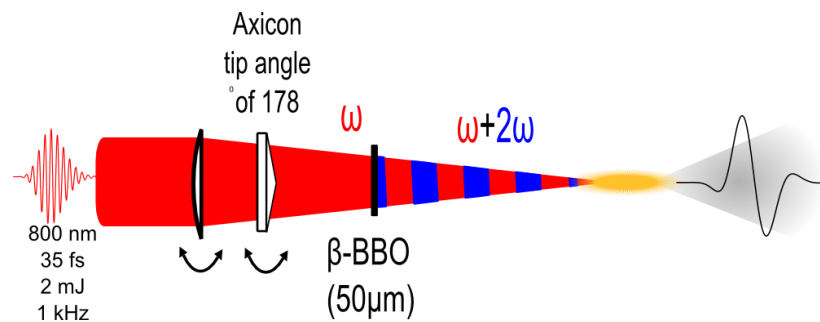


**Figure 38: Experimental approach for filamentation tailoring using wavefront distortions.**

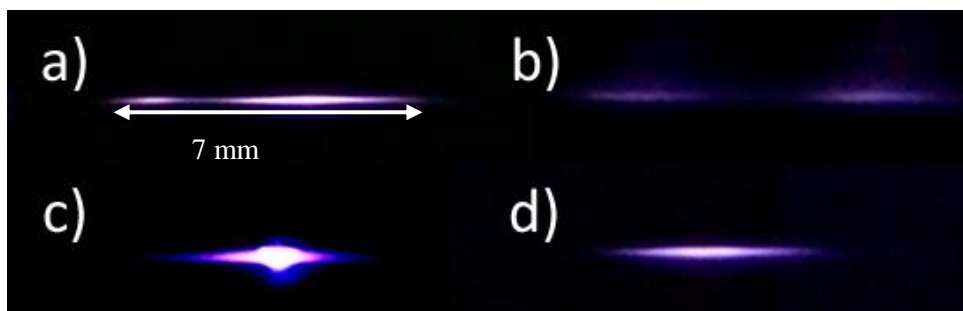


**Figure 39: Images of filament plasma string distributions under various experimental conditions.**

**(a) Asymmetric and (b) symmetric double peaks, (c) gradient and (d) uniform.**

### III.2.2 The effect on the THz pulse emission

In order to be sure to capture any potential effect due to the plasma tailoring, we recorded the emitted THz electric field using the very thin GaP (100  $\mu\text{m}$ ) crystal. As shown in the previous chapter, this crystal can resolve shorter pulses and is hence well adapted to the present study. The emitted THz radiation was measured for the plasma string profiles presented in Figure 39. As expected the obtained THz emission strongly depends on the plasma density distribution (see Figure 40). On this figure, each of the electric field traces has been arbitrarily shifted vertically for clarity purposes.

The first observation is that each plasma profile yields a different electric field in terms of strength and time duration. The most remarkable difference occurs between the uniform and the gradient plasma profile. A very important shortening seems to take place between the two conditions. For clarity, the electric field traces have been normalised and placed on the same y position as presented in Figure 41(a). The THz pulse emitted from the uniform plasma string is significantly shorter than the one with the strong gradient plasma string. For the uniform plasma string the emitted THz pulse duration was  $\sim 250$  fs (FWHM), while in the case of the gradient plasma string the corresponding THz pulse duration was  $\sim 400$  fs.

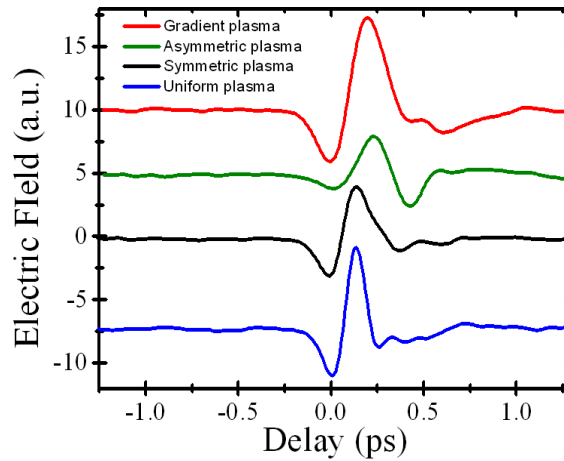


Figure 40: Measured electric field traces for the various plasma profiles.

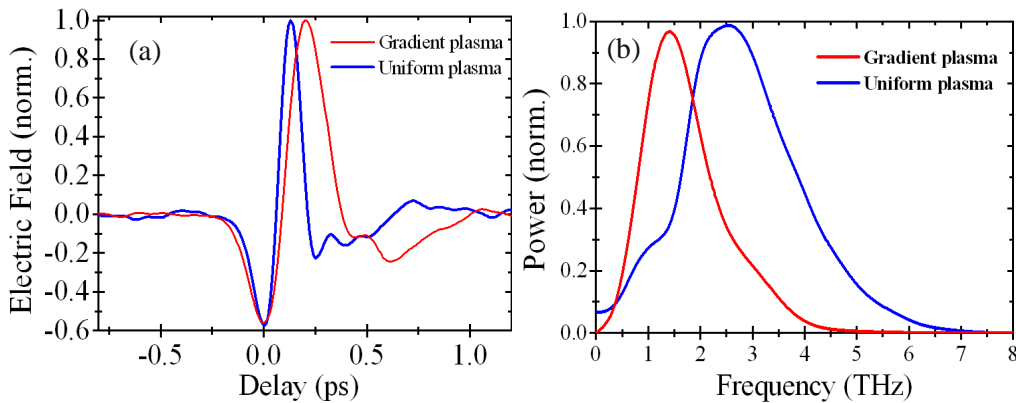
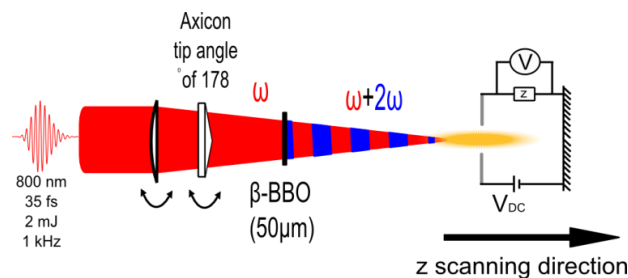


Figure 41: (a) Normalised electric field for the case of gradient and uniform plasma string. (b) Their respective Fourier transforms.

Applying a Fourier transform to the measured THz fields of Figure 40, the corresponding power spectra were obtained and are shown in Figure 41(b). As expected from the shorter pulse duration, the spectral bandwidth obtained for the uniform plasma string is significantly extended, from 4 THz of useful bandwidth to 7 THz. Furthermore, the central frequency is shifted by approximately 1.2 THz for the uniform plasma string. It is worth noticing that if we would have been able to keep the same level of energy, the increase of electric field strength would have been in the order of 76% for the case of the uniform plasma string.

### III.2.3 Measurement of the electron density

To fully relate this shortening with the electron density profile, we attempted to obtain quantitative information about the plasma densities. For this purpose, we employ the electric conductivity technique [9], which is schematically represented in Figure 42. The measurement system consisted of two steel electrodes ( $\sim 1$  mm diameter) separated by 3 mm distance. A Teflon slit aperture was placed in front of the electrodes to exclude undesired ionization on the electrode's surfaces and the whole system was mounted on a millimetre translation stage in order to scan the plasma string along the propagation axis. The plasma string passed between the two electrodes while a DC high voltage (1.4 kV) was applied on them. The laser generated plasma redistributed in the presence of the applied external electric field ( $\sim 4.7$  kV/cm) and screened out the external field, generating a potential drop across the electrodes that caused a current to flow through the  $8\text{ k}\Omega$  probe resistance of the electric circuit. The voltage drop across the resistance was measured using a standard oscilloscope. When this detection setup is operated in the Ohmic regime (current is proportional to the applied high voltage) the measured electric signal depends linearly on the mean, over the plasma channel diameter, excited electron density  $\langle N_e \rangle$ . The correlation of the electric conductivity measurements to plasma density estimations was done by comparison with a precise, but more complex, holographic method [10]. The electron plasma density distribution for the case of strong gradient plasma and uniform plasma is shown in Figure 43. In our experiments the strong gradient plasma string is obtained with the plano-convex lens, without the axicon, oriented perpendicular to the input laser beam. For the uniform plasma string both lenses (plano-convex and axicon) were used and tilted at about  $10^\circ$  each from their initial positions in the same direction.



**Figure 42: Schematic of the experimental set-up for the measurement of the plasma electron density.**

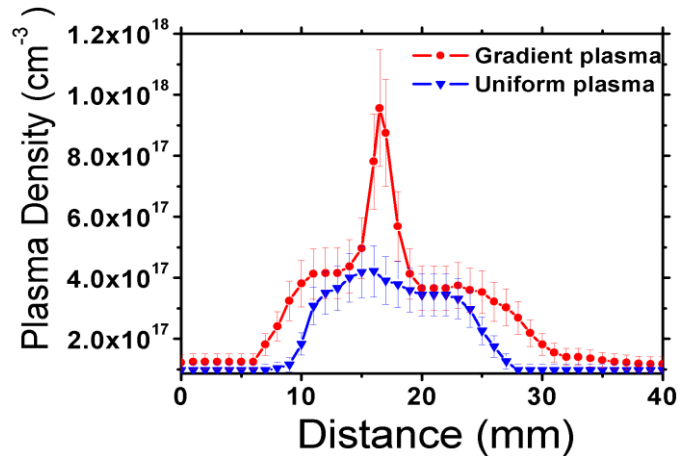


**Figure 43: Measured electron density profile along the propagation axis for the two cases of interest.**

As suggested by the CCD pictures of figure 2, the so-called gradient plasma presents a strong increase of electron density at its centre, which is nearly 1 order of magnitude higher than the uniform case. This lack of uniformity probably comes from the refocusing cycle of the filamentation process which is in turn extended over a longer distance as the measurement shows it. The results presented in Figure 41 and Figure 43 clearly suggests that uniform plasma with a lower density generates higher frequencies than gradient plasma.

In order to illustrate this point, we have investigated another approach. To obtain a uniform plasma string, one can also use a lens with a longer focal length and low laser input energy. The longer focal length will spread the electron density over a longer distance, while the low laser pulse energy will avoid the problem of refocusing cycle observed before. Therefore, if our previous observation is correct, a THz pulse emitted at low laser input energy in this focusing condition should be shorter than a THz pulse emitted at high laser pulse energy. The results presented in Figure 44 are in clear agreement with our previous observations. At low laser energy, the uniform plasma string emits shorter THz pulses which in turn offer an extended bandwidth.

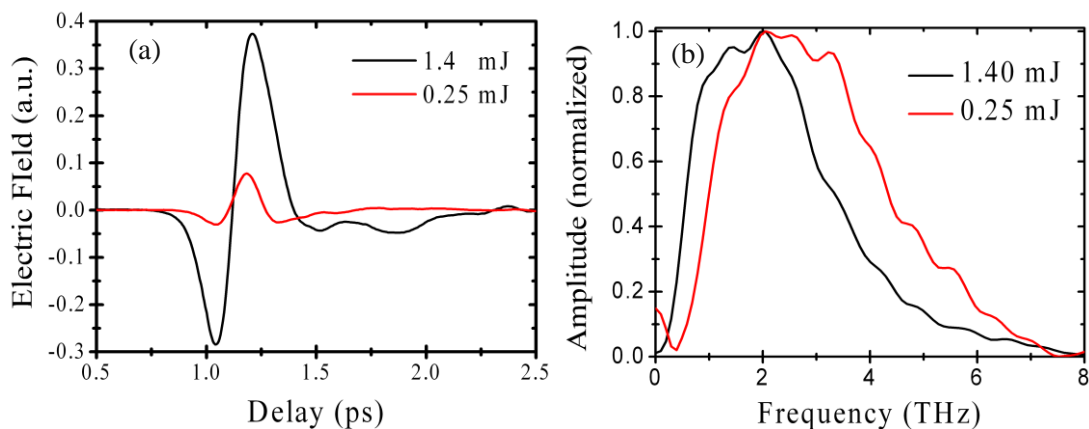


**Figure 44: (a) Measured THz pulse electric fields at two different levels of input laser pulse energy. (b) FFT of the electric field.**

Nevertheless, the approach which consists of introducing distortion to the laser pulse wavefront is by far more efficient in terms of electric field strength as seen when comparing Figure 40 and Figure 44(a). For comparison, the peak to peak ratio between the short and long THz pulse is equal to 0.89 with the first experimental approach. With the second approach, the ratio drops to 0.16.

The photocurrent point source model attributes THz generation to a net ionization current resulting from the asymmetry in the ionizing pulse [11, 12]. This has been shown to be in good agreement with results from particle in cell simulation which models THz emission from an extended longitudinal plasma [13], although not so long as a filament. All these models predict that the squared central frequency of the THz emission is directly proportional to the plasma electron density. This seems incompatible with our observations showing that the uniform plasma with the lower density generates higher frequencies than the gradient plasma. However, none of these models consider a strong gradient in the local electron density and coherent emission from the different parts of a non uniform plasma string. By focusing a few cycle pulse with an axicon, it was shown [14] that ionization induced plasma oscillations lead to an optical to THz conversion by far more efficient than that induced by the ponderomotive force [15, 16]. The proposed mechanism is similar to the photocurrent model except that it also accounts for non-uniformity of the plasma string distribution. This model shows that a larger spectrum, thus resulting in a shorter pulse, should be emitted from a uniform plasma string compared to the case of a plasma gradient, which explains rather well the results presented in this study.

In conclusion, in this section we provided the first to our knowledge demonstration of THz pulse optimization using appropriately tailored 2-color ultrashort laser filaments in air. Significant THz pulse shortening is achieved for uniform plasma strings. These results will prove valuable in applications where tailored THz pulses are needed. The obtained results also bring valuable information for a deeper understanding of the physical processes involved in this coherent emission.

## III.3/ Strong terahertz emission enhancement via filament concatenation in air

### III.3.1 Extension of the plasma length using the concatenation effect

Due to the highly dynamical nature of filaments, the optimization of the THz radiation emitted from them is not a trivial task and requires a good understanding of the external parameters which control their formation. For example, it has been already shown that the THz beam directionality could be increased as a function of the plasma string length [17]. The further increase of the THz pulse peak power has always been and remains a subject of fundamental importance. A number of efforts in this direction have been conducted in the last years, many of them employing two collinear plasma strings. For example, in the case of single color filaments without a DC bias voltage, a pre-existing plasma background effect, lasting for hundreds of picoseconds, has been shown to increase the THz power by a factor of 2.5 [18]. Later the same approach of bi-filamentation showed an increase by one order of magnitude of the strength of the weak THz source, present in the wake of a filament [19]. The latter was a nanosecond-lasting time scale effect, which was identified as being the result of the formation of a transmission line between the two slightly misaligned filaments. In the two-color filaments configuration, a rather small enhancement attributed to four-wave parametric process has been observed [20]. Also, in a multiple adjacent filaments configuration, a coherent superposition of THz radiation was demonstrated to weakly increase the THz output power [21].

Creating long plasma strings with uniform and relatively high average electron densities is not a trivial task. Concatenation, on the other hand, of shorter filaments is a nice way for bypassing this problem. The first demonstration of filamentation concatenation was reported in Ref. [22], where two filaments were shown to merge into a single filament of extended length under appropriate positioning and timing. This concatenation effect was also demonstrated to be an efficient tool for pulse compression [23]. Furthermore, this experimental work has brought the first demonstration of superluminal velocities of light within a filament. Indeed, it was shown that for these long filamentary structures one of the filaments needs to be delayed by 100 fs in order to merge with the other filament.

For the experiments described here, a Mach-Zehnder interferometer was built in order to separate the initial beam in two and appropriately recombine them (Figure 45). The control of the respective delay of the two beams was achieved using a high precision step motor (attosecond control). Both beams were focused with identical lenses of 200 mm before being recombined. In one of the arms, the lens as well as the last mirror was mounted on a micrometer stage, offering an accurate control on the position in space of one of the plasma strings in respect to the other. In the case of the two-color filamentation configuration, a Type I  $\beta$ -BBO crystal (50  $\mu\text{m}$  thick) was placed in the optical path of the recombined beams to partially double them in frequency.

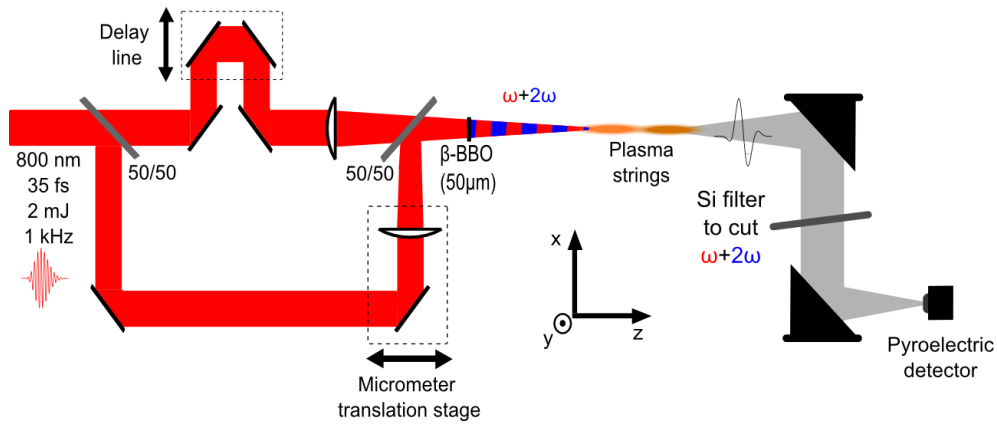


**Figure 45: Schematic representation of the experimental approach.**

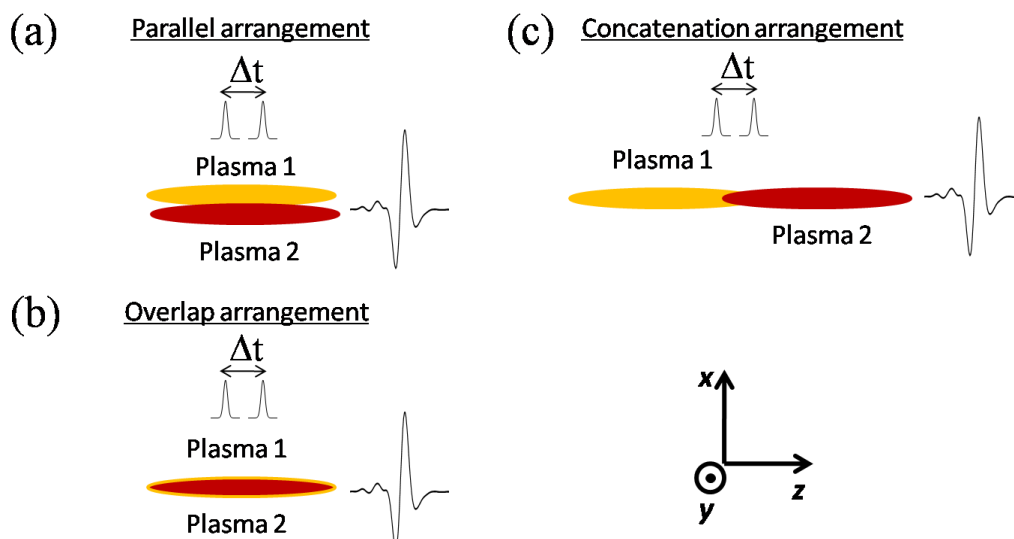


**Figure 46: Schematic representation of the investigated spatial arrangement.**

The emitted THz field from the plasma columns was collected and refocused on the detector by a pair of 2 inches parabolic mirrors with 100 mm focal lengths. The remaining optical radiation was stopped with a high-resistivity silicon wafer (1mm thick) while leaving the THz radiation passing through in order to be measured with our broadband thermal pyroelectric detector.

The above described experimental arrangement allowed us to form a set of two filaments of equivalent power [for the same input laser pulse energy (400 μJ)] that consequently yielded, independently, a quasi identical level of THz radiation. We then tuned the position of one filament with respect to the other one. The various spatial arrangements that have been investigated are presented in Figure 46. Each of the arrangement has been investigated and we made sure each time that the temporal overlap was optimized.

### III.3.2 The effect on the THz pulse emission

The emitted radiation from the two filaments that are synchronized in time and separated in space along the x-axis (parallel arrangement, Figure 46(a)) was first measured. In this case, the total THz emission is the sum of the two THz fields. Once the plasma channels are synchronized in time and well overlapped at the exact same position in space (x,y,z), coherent emission with an enhancement of a factor 4 compared to the field of a single filament is achieved (overlap arrangement, Figure 46(b)). Though, almost the same result is obtained, if instead of two similar beams, we focus one single beam but with the total energy of the two (i.e. 800  $\mu$ J). The CCD picture of this filament shows that it extends over 3.5 mm with an electron density which is higher than each of the 400  $\mu$ J plasma strings. Nevertheless, once the filaments are arranged at the same (x,y) positions but with an appropriate shift along the propagation direction (concatenation arrangement, Figure 46(c)) and for appropriate timing, an enhancement up to 1 order of magnitude is obtained. Under these conditions the two filaments are concatenated and extend over 5.5 mm length. Although in the present case the formed filamentary structures are much shorter than the ones reported in [22], from the pictures presented in Figure 47, the concatenation effect is clearly observable.

Figure 48 (a) is summarizing the different measurements for both configurations. The strong enhancement that is obtained under concatenation conditions is evident and is almost the same for the single and 2-color cases. The pictures in Figure 48(b) show that the effect is spatially very sensitive. Observing the interference fringes between the two beams (reflected from the BBO crystal), one can see that the maximum emission is occurring when there is a minimum of fringes, which happens when the two beams are well aligned along the z-axis. On the contrary if the two beams are slightly parallel, no matter the timing, the THz emission is even less than the sum of the two independent filament emissions. This observation demonstrates that the enhancement cannot be the result of the formation of a transmission line formed by two slightly misaligned filaments as it was the case in [19].

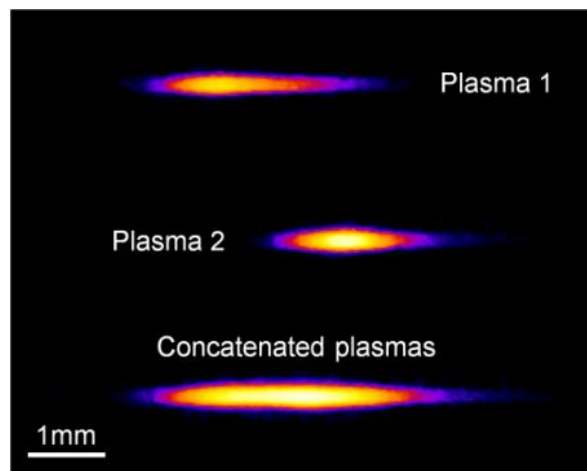


**Figure 47: Experimental pictures (fluorescence) of the 2 independent plasma strings and the concatenated one (pictures were taken with identical scales and camera exposure).**

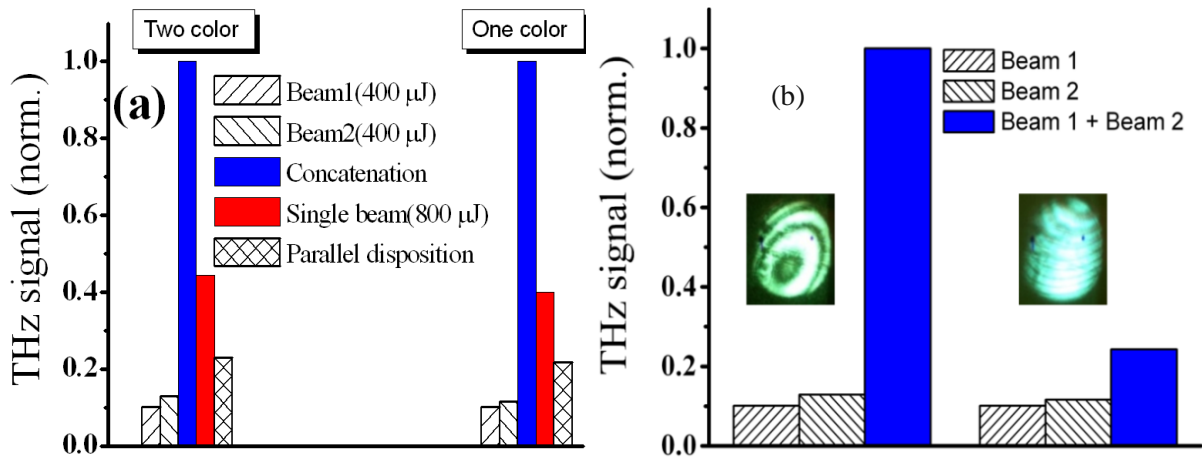


Figure 48: (a) THz signal yielded for different arrangements. (b) Effect of the spatial alignment sensitivity: concatenation (left) and close to concatenation (right).

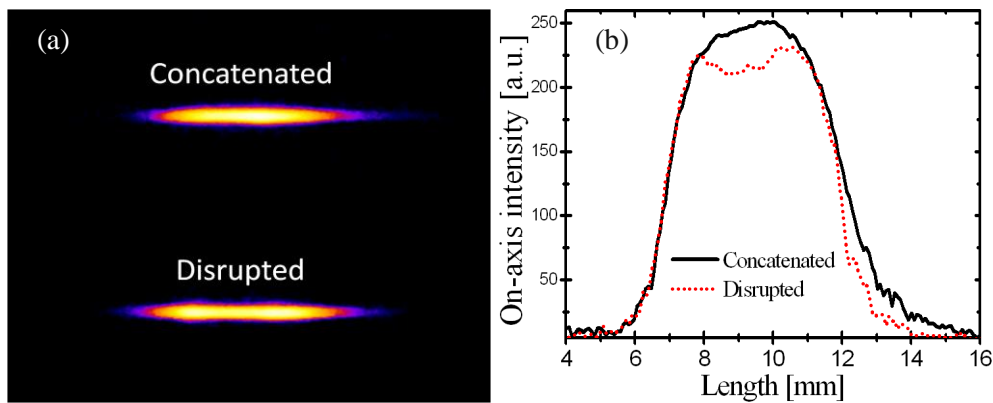
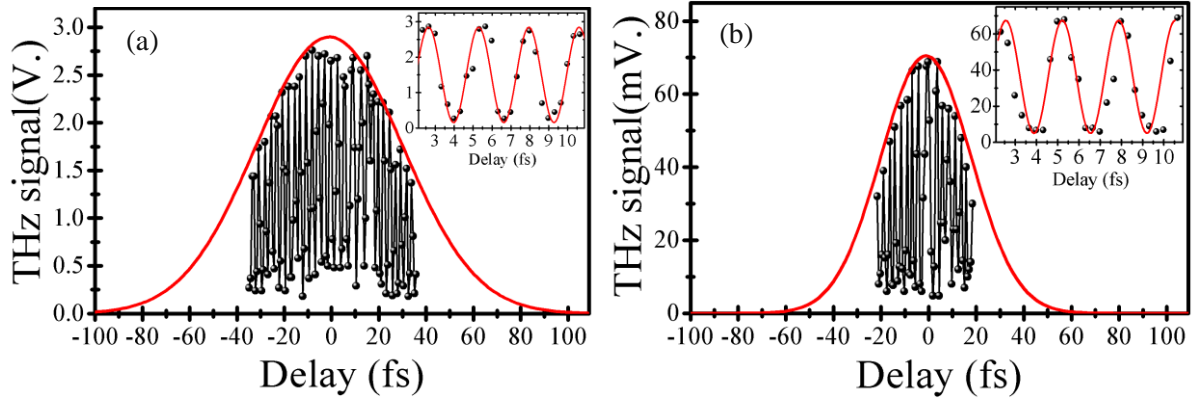


Figure 49: CCD pictures of a concatenated filament and a disrupted filament. On the right is presented the on-axis intensity profile.

Furthermore, once the filaments are concatenated, instabilities seem to occur. This is strongly related with the conical emission of white light, which either gets enhanced or decreased as the strength of the emitted THz radiation gets decreased or enhanced respectively. A CCD picture with both configurations is presented in Figure 49 (a). Their respective on-axis intensity profile suggests the presence of disruptive effect that may be correlated with their time overlap (Figure 49(b)).

### III.3.3A cross correlation effect

To better understand the observed enhancement, we performed additional experiments which show the effect of the delay between the two pulses on the THz radiation. In the case of 2-color filamentation, a scan with 0.7 fs resolution is shown in Figure 50(a). The result shows a THz radiated emission oscillating between maxima and minima as the delay between the two pulses is changed. The overall scan can be fitted with a Gaussian envelope, which is expected to be the result of the cross correlation between the two laser pulses. The FWHM of the envelope is equal to 73 fs, which after deconvolution gives an initial pulse length of 52 fs.



**Figure 50: THz signal as a function of the delay between the two laser pulses: (a) in the case of 2-color filamentation; (b) in the case of 1 color filamentation. Insets show better resolved oscillations.**

This duration is slightly bigger than our initial pulse duration, but can be explained by a temporal elongation while passing through the frequency doubling crystal. A better resolved experiment (step size 0.35 fs), showed that the THz emission can be very well fitted with the 800 nm cosine field, having a 2.66 fs period in air (see inset of Figure 50a). The same experiment has been conducted for the single color case and a similar effect has been observed as one can see in Figure 50(b). The envelope of the cross correlation is fitted with a Gaussian function, with a FWHM of 35 fs after de-convolution. This duration corresponds well to our initial laser pulse duration. Again in this case the THz emission can be fitted with the 800 nm laser electric field.

The fact that the THz emission follows the cross correlation of the two initial laser pulses demonstrates that the enhancement is not the result of the coherent superposition of different independent THz sources as it was demonstrated in [21]. Moreover, the short time (during the overlap of the two pulses) of the enhancement fully rejects the possibility of an increase due to a pre-existing plasma background which has been shown to last for hundreds of picoseconds [18]. It is thus clear that the observed enhancement, which is bigger than a simple superposition of two coherent THz sources, is the result of the concatenation between the two filaments into a single longer plasma string.

In conclusion, in this section, using the effect of concatenation between two collinear filaments in air, we demonstrated a strong amplification of the emission of the THz radiation. This enhancement which lasts during the coherent superposition of the two filaments is the result of a homogenous extension of the electron plasma string length. The proposed approach is an elegant way of producing more intense THz pulses with this simple filamentation tailoring approach.

## III.4/ Terahertz polarization state control from tailored femtosecond filaments in air

### III.4.1 Effect of an extended plasma length on the THz polarization control

In the previous chapter, we have already presented the direct control of the THz pulses polarization while playing with the dispersion induced by the surrounding gas pressure. This clearly indicates that the THz radiation is emitted from a transversal photocurrent. Nevertheless, the experiment already presented has been done at relatively low input laser pulse energy for which the plasma length is short. As a consequence, the yielded THz power was low. To obtain higher THz powers one needs to create longer filaments and this can be done by increasing the input laser energy. In Figure 51, we present the yielded THz power as a function of the gas pressure for different input laser pulse energies. One can clearly see that as the input laser pulse energy is increased, which automatically leads to a longer filamentary structure, an oscillatory behaviour is becoming more prominent.

This experimental observation let us presume that the nature of the oscillatory behaviour is directly linked with the plasma length and consequently as it was reported in [24], with the appearance of Maker fringes due to the phase walk-off in the extended plasma filament. In addition, when the THz power exhibits oscillatory behaviour we systematically observed that the polarization rotates unpredictably and not in accordance with the estimated relative phase difference variation as in the case of low laser energy power as presented in Figure 52. Indeed we measured a flip of  $95^\circ$  between the pressure point of 310 mBar and 600mBar, when calculations predicted only  $35^\circ$  of polarization rotation. This unexpected rotation of  $60^\circ$  of the THz pulse is the direct result of the filament extension. Another consequence of the plasma length extension is the appearance of ellipticity in the polarization of the emitted THz pulses. Ellipticity has also been observed in [25] and will be discussed in more details later.

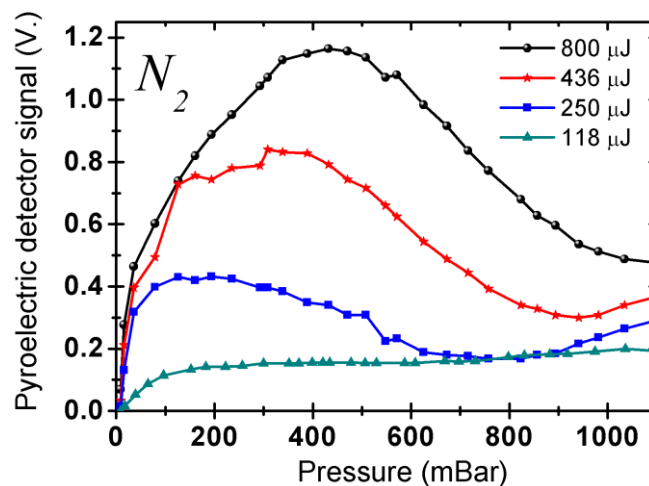


Figure 51: Detected THz power as function of nitrogen gas pressure for various laser input energies

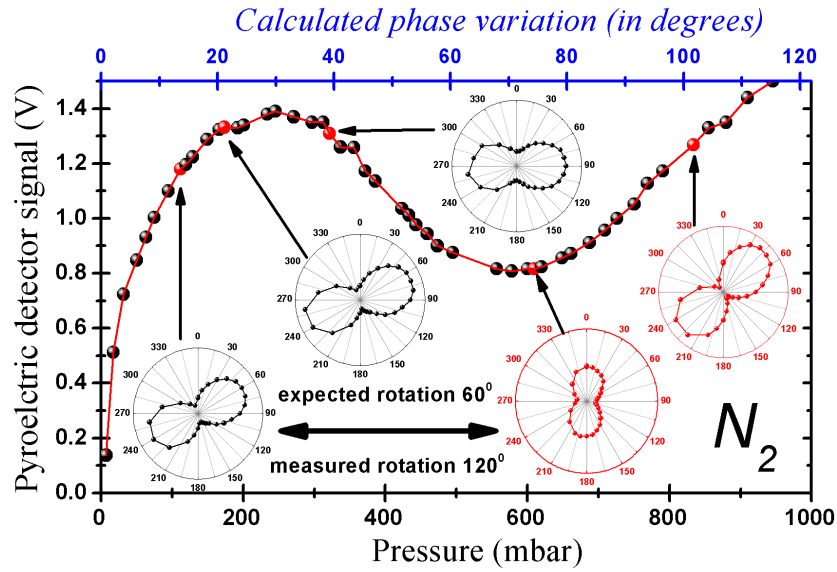


Figure 52: Detected THz power as function of nitrogen gas pressure (black Dots and red curve) and THz pulse polarization states at different pressure levels for an extended plasma length. The upper axis (blue colour) represents the calculated phase variation.

### III.4.2 A Tailoring approach to circumvent the phase walk-off

This oscillatory feature appears to be also dependent on the tilt of the BBO crystal one can see in Figure 53(a). A similar observation was reported in [12] and was attributed to the variation in the 800 nm beam ellipticity as the birefringent BBO crystal is tilted. We propose here a different explanation of the effect, which is related to the length of the filament and not on the increased ellipticity, which we measured and found it to be negligible. In our experiments measurements were made for different tilt angles of the BBO crystal, recording at the same time the THz emission as well as CCD pictures of the filaments' plasma fluorescence. Furthermore, for these measurements the BBO crystal is moved from the focusing point, in order to resolve one full oscillation in the contrary of the results presented in Figure 51.

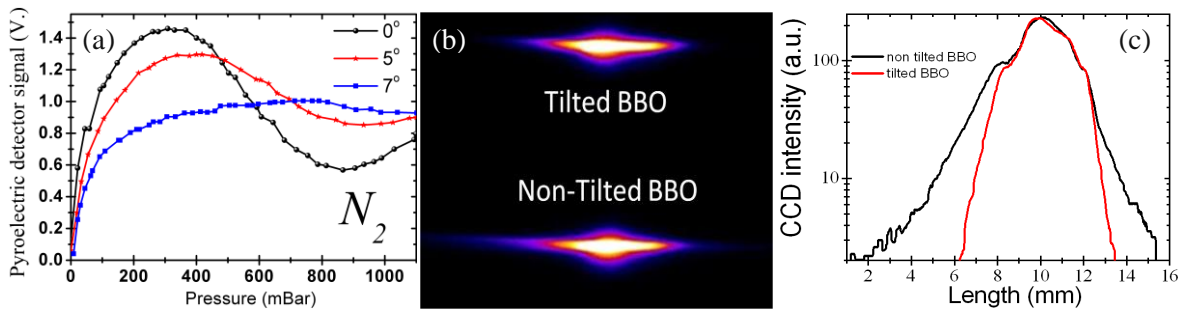
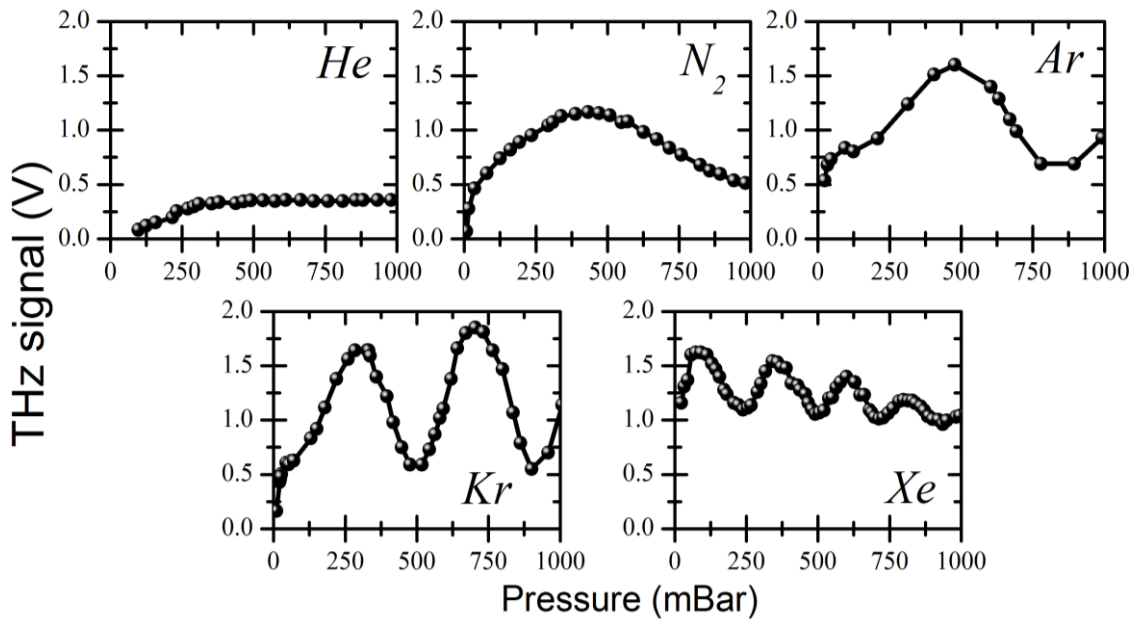


Figure 53: (a) Detected THz power as function of nitrogen gas pressure for various BBO tilting angles. (b) CCD pictures of plasma fluorescence for a BBO tilt angle of 7 degrees and a non-tilted

**BBO crystal (pictures were taken with identical scales and camera exposure). (c) On-axis fluorescence intensity profile for a BBO tilt angle of 7 degrees and a non-tilted BBO crystal.**

Figure 53(b) shows the plasma fluorescence for the case of 7 degrees tilt of the crystal compared to the non tilted one. As the on-axis intensity profiles of the CCD pictures attest (Figure 53(c)), the fluorescence of the plasma string formed after tilting of the BBO crystal is twice shorter (7 mm vs. 14 mm). This shortening is the result of the smaller amount of second harmonic when the BBO is tilted.

Furthermore, in order to fully relate the oscillatory behaviour of the THz output with the length of the plasma string, we conducted a pressure study with a non tilted BBO crystal for different rare gases. First, as one can see in Figure 54, the number of oscillations, over the same pressure range, increases for gases exhibiting higher atomic dispersion. Experimentally, we observed that the plasma formed within helium gas, which shows no oscillatory behaviour, was the shortest of all the filaments formed in the other gases. We also observed that for high input laser pulse energy, it is not possible to avoid this oscillatory behaviour with gases having a low ionization potential, such as Krypton (14 eV) and Xenon (12.13 eV) as shown in Figure 54. Even the BBO tilting approach described above is not enough to circumvent the oscillations for Krypton and Xenon gases. For such gases, the saturation intensities within the filament are much lower than for gases with higher ionization potential (e.g.  $N_2$  (15.58 eV) or Ar (15.76 eV), He (24.58 eV)) and the excess of input laser energy leads to an extension of the plasma length as was shown with numerical simulations in [26]. Consequently the effect of phase walk-off cannot be avoided for extended plasma length, whereas it does not exist for very short filamentary structures.



**Figure 54: THz power emitted from a double colour filament produced in different gas mediums (He,  $N_2$ , Ar, Kr, Xe) and at pressures ranging from 10 mbar up to 1013 mbar.**

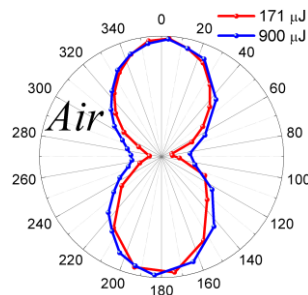


### III.4.3 Effect of an extended plasma length on the THz polarization state

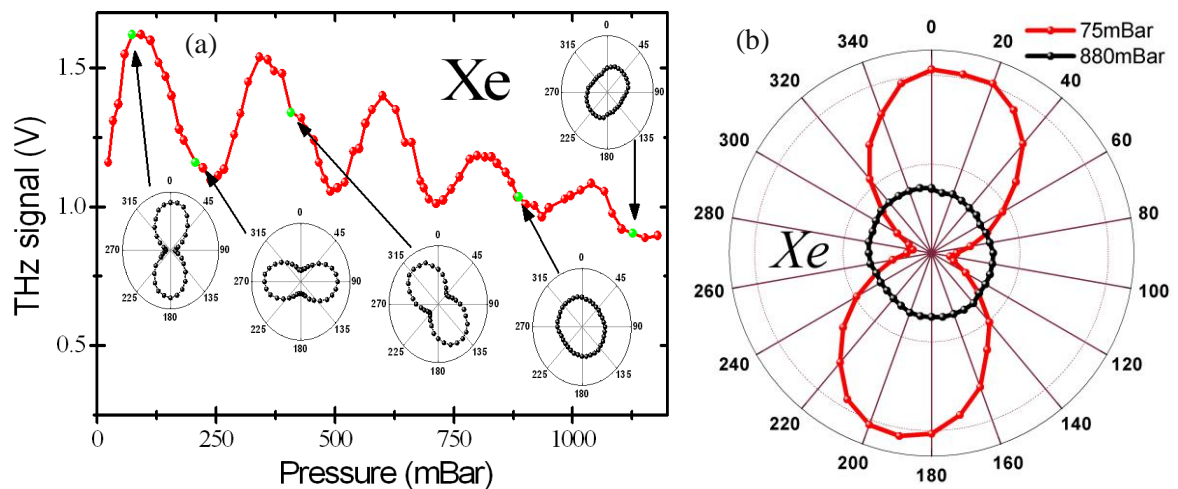
The disadvantage linked to extended plasma length for the control of the THz pulse polarization rotation can be useful to generate other polarization states than purely linear. As mentioned above, the increase of the input laser energy leads to the appearance of ellipticity on the polarization of the THz pulses. To illustrate further our observations, we have measured the polarization state of the THz beam in normal atmosphere conditions for two different levels of input laser pulse energies. The data presented in

Figure 55 have been normalized and clearly show the increase of the ellipticity of the THz beam with increasing input laser pulse energy. This has already been reported in the literature [25] and was also attributed to an extension of the filament length due to higher input laser pulse energy. It was also demonstrated that a filament can act as a polarization separator for a co-propagating beam [27]. Consequently as the plasma is getting elongated for higher laser pulse energies, the local THz radiation generated along the filament will experience a stronger birefringence, which in turn results to an increased THz ellipticity.

Triggered by this experimental evidence, we investigated the effect induced by the pressure variation for a gas producing longer filamentary structures. Hence, a systematic study of the THz generation in Xenon over one bar of pressure range was performed and the THz polarization state at various pressure levels was analyzed. The results are presented in Figure 56(a). As expected, the polarization of the THz pulse is rotating as the pressure of the gas medium is changing. The rotation is much more important than in nitrogen over the same range of pressure, which is due to the bigger atomic dispersion of the xenon gas. Beyond the rotation of the THz pulses polarization, we have been able to obtain elliptically polarized THz pulses at different states and up to fully circular polarized THz pulses, as one can also see in Figure 56(a). We interpret this interesting result as the result of two joint effects occurring on the plasma filament. It is well known in the literature that the filament radius decreases with an increase of the surrounding gas pressure, see for instance [28]. Also, the length of the filament is known to extend as the gas pressure increases [29]. The decrease of the filament radius inevitably leads to a decrease of the generated THz power as one can see in Figure 56(a).



**Figure 55: Normalized values of THz beam polarization state for two different level of input laser pulse energy.**



**Figure 56: (a) Detected THz power as function of xenon gas pressure and THz pulse polarization states at different pressure levels of Xenon gas and (b) the linear polarization (red curve) state of THz pulse at low pressure compared to the circular polarized THz (black curve) at 880 mbar.**

In parallel to the decrease of the main THz component, an increase of the orthogonal THz component is observed until it reaches values equivalent to the main component and results to a circularly polarized THz pulse (Figure 56(b)). This can be related to the increasing birefringence induced by the extended filament. The combination of both effects induces more and more ellipticity in the polarization of the THz beam up to the point where the polarization becomes fully circular.

In conclusion, in this section, we have demonstrated experimentally the possibility to control the polarization of THz pulses emitted from two color filaments in gases. We also reported a way to circumvent the disadvantage caused by the phase walk-off between the two laser fields within an extended plasma string. Finally, we have shown the possibility to obtain circularly polarized THz pulses using longer plasma filaments. The later is an elegant and easy way for producing circularly polarized THz light, opening new opportunities in THz time domain spectroscopy.

### III.5/ Chapter conclusions

In this chapter, the importance of filamentation tailoring has been demonstrated. The two color filament source which is one of the most intense table top sources of THz radiation can be considerably optimized if great attention is brought on the shaping of the filament. Clear experimental data have shown that the electron density distribution influences the duration of the emitted THz pulse [30]. In the same way, we showed that a uniformly extended plasma string with a relatively high electron density leads to a strong enhancement of the emitted THz radiation [31]. Finally, by exploring the effect of the plasma volume on the THz emission, we have demonstrated the possibility

to obtain circularly polarized THz light [32]. All these findings bring valuable information to the community concerning the optimization of this THz source. It also suggests introducing new parameters within theoretical models in order to accurately describe the physical mechanisms behind this coherent emission of THz radiation.

## Reference

1. D. Abdollahpour, P. Panagiotopoulos, M. Turconi, O. Jedrkiewicz, D. Faccio, P. Di Trapani, A. Couairon, D. G. Papazoglou, and S. Tzortzakis, "Long spatio-temporally stationary filaments in air using short pulse UV laser Bessel beams," *Optics Express* 17, 5052-5057 (2009).
2. G. Mechain, A. Couairon, M. Franco, B. Prade, and A. Mysyrowicz, "Organizing multiple femtosecond filaments in air," *Phys. Rev. Lett.* 93, 4 (2004).
3. G. Heck, J. Sloss, and R. J. Levis, "Adaptive control of the spatial position of white light filaments in an aqueous solution," *Optics Communications* 259, 216-222 (2006).
4. S. Suntsov, D. Abdollahpour, D. G. Papazoglou, and S. Tzortzakis, "Femtosecond laser induced plasma diffraction gratings in air as photonic devices for high intensity laser applications," *Applied Physics Letters* 94, 3 (2009).
5. A. Couairon and A. Mysyrowicz, "Femtosecond filamentation in transparent media," *Physics Reports-Review Section of Physics Letters* 441, 47-189 (2007).
6. P. Sprangle, J. R. Penano, B. Hafizi, and C. A. Kapetanakis, "Ultrashort laser pulses and electromagnetic pulse generation in air and on dielectric surfaces," *Phys. Rev. E* 69, 066415-(066411-066418) (2004).
7. A. Couairon and A. Mysyrowicz, "Femtosecond filamentation in transparent media," *Phys. Rep.* 441, 47-189 (2007).
8. G. Fibich, S. Eisenmann, B. Ilan, and A. Zigler, "Control of multiple filamentation in air," *Opt. Lett.* 29, 1772-1774 (2004).
9. S. Tzortzakis, M. A. Franco, Y. B. Andre, A. Chiron, B. Lamouroux, B. S. Prade, and A. Mysyrowicz, "Formation of a conducting channel in air by self-guided femtosecond laser pulses," *Phys. Rev. E* 60, R3505-R3507 (1999).
10. D. G. Papazoglou and S. Tzortzakis, "In-line holography for the characterization of ultrafast laser filamentation in transparent media," *Appl. Phys. Lett.* 93, 041120-(041121-041123) (2008).
11. K. Y. Kim, A. J. Taylor, J. H. Glowina, and G. Rodriguez, "Coherent control of terahertz supercontinuum generation in ultrafast laser-gas interactions," *Nat. Photonics* 2, 605-609 (2008).
12. H. D. Wen and A. M. Lindenberg, "Coherent Terahertz Polarization Control through Manipulation of Electron Trajectories," *Phys. Rev. Lett.* 103, 4 (2009).
13. M. Chen, A. Pukhov, X. Y. Peng, and O. Willi, "Theoretical analysis and simulations of strong terahertz radiation from the interaction of ultrashort laser pulses with gases," *Phys. Rev. E* 78, 046406 (2008).
14. V. B. Gildenburg and N. V. Vvedenskii, "Optical-to-THz wave conversion via excitation of plasma oscillations in the tunneling-ionization process," *Phys. Rev. Lett.* 98, 245002 (2007).
15. L. M. Gorbunov and A. A. Frolov, "Transition radiation generated by a short laser pulse at a plasma-vacuum interface," *Plasma Phys. Rep.* 32, 850-865 (2006).
16. C. D'Amico, A. Houard, S. Akturk, Y. Liu, J. Le Bloas, M. Franco, B. Prade, A. Couairon, V. T. Tikhonchuk, and A. Mysyrowicz, "Forward THz radiation emission by femtosecond filamentation in gases: theory and experiment," *New J. Phys.* 10, 013015-(013011-013018) (2008).
17. H. Zhong, N. Karpowicz, and X. C. Zhang, "Terahertz emission profile from laser-induced air plasma," *Applied Physics Letters* 88, 261103-261103 (2006).

18. X. Xie, J. Xu, J. Dai, and X. C. Zhang, "Enhancement of terahertz wave generation from laser induced plasma," *Applied Physics Letters* 90, 141104-141103 (2007).
19. Y. Liu, A. Houard, B. Prade, S. Akturk, A. Mysyrowicz, and V. T. Tikhonchuk, "Terahertz radiation source in air based on bifilamentation of femtosecond laser pulses," *Phys. Rev. Lett.* 99(2007).
20. J. Dai, X. Xie, and X. C. Zhang, "Terahertz wave amplification in gases with the excitation of femtosecond laser pulses," *Applied Physics Letters* 91, 211102-211103 (2007).
21. M.-K. Chen, J. H. Kim, C.-E. Yang, S. S. Yin, R. Hui, and P. Ruffin, "Terahertz generation in multiple laser-induced air plasmas," *Applied Physics Letters* 93, 231102-231103 (2008).
22. S. Tzortzakis, G. Méchain, G. Patalano, M. Franco, B. Prade, and A. Mysyrowicz, "Concatenation of plasma filaments created in air by femtosecond infrared laser pulses," *Applied Physics B: Lasers and Optics* 76, 609-612 (2003).
23. A. Couairon, G. Méchain, S. Tzortzakis, M. Franco, B. Lamouroux, B. Prade, and A. Mysyrowicz, "Propagation of twin laser pulses in air and concatenation of plasma strings produced by femtosecond infrared filaments," *Optics Communications* 225, 177-192 (2003).
24. Y. Liu, A. Houard, M. Durand, B. Prade, and A. Mysyrowicz, "Maker fringes in the Terahertz radiation produced by a 2-color laser field in air," *Opt. Express* 17, 11480-11485 (2009).
25. Y. Chen, C. Marceau, S. Génier, F. Théberge, M. Châteauneuf, J. Dubois, and S. L. Chin, "Elliptically polarized Terahertz emission through four-wave mixing in a two-color filament in air," *Optics Communications* 282, 4283-4287 (2009).
26. A. Couairon, H. S. Chakraborty, and M. B. Gaarde, "From single-cycle self-compressed filaments to isolated attosecond pulses in noble gases," *Physical Review A* 77, 053814 (2008).
27. Y. Chen, C. Marceau, F. Théberge, M. Châteauneuf, J. Dubois, and S. L. Chin, "Polarization separator created by a filament in air," *Opt. Lett.* 33, 2731-2733 (2008).
28. N. Kortsalioudakis, M. Tatarakis, N. Vakakis, S. D. Moustazis, M. Franco, B. Prade, A. Mysyrowicz, N. A. Papadogiannis, A. Couairon, and S. Tzortzakis, "Enhanced harmonic conversion efficiency in the self-guided propagation of femtosecond ultraviolet laser pulses in argon," *Applied Physics B: Lasers and Optics* 80, 211-214 (2005).
29. G. Méchain, T. Olivier, M. Franco, A. Couairon, B. Prade, and A. Mysyrowicz, "Femtosecond filamentation in air at low pressures. Part II: Laboratory experiments," *Optics Communications* 261, 322-326 (2006).
30. J. M. Manceau, A. Averchi, F. Bonaretti, D. Faccio, P. Di Trapani, A. Couairon, and S. Tzortzakis, "Terahertz pulse emission optimization from tailored femtosecond laser pulse filamentation in air," *Opt. Lett.* 34, 2165-2167 (2009).
31. J. M. Manceau, M. Massaouti, and S. Tzortzakis, "Strong terahertz emission enhancement via femtosecond laser filament concatenation in air," *Opt. Lett.* 35, 2424-2426 (2010).
32. J.-M. Manceau, M. Massaouti, and S. Tzortzakis, "Coherent control of THz pulses polarization from femtosecond laser filaments in gases," *Opt. Express* 18, 18894-18899 (2010).

*Chapter IV: Time Domain Spectroscopy for  
the analysis of cultural heritage related  
materials*

<b>CHAPTER IV: TIME DOMAIN SPECTROSCOPY FOR THE ANALYSIS OF CULTURAL HERITAGE RELATED MATERIALS.....</b>	<b>91</b>
<b>IV.1/ Introduction to cultural heritage studies.....</b>	<b>93</b>
<b>IV.2/ Qualitative and quantitative analysis in transmission mode .....</b>	<b>94</b>
IV.2.1 Experimental approach and samples preparation .....	94
IV.2.2 Experimental results.....	96
<b>IV.3 / Analysis in reflection mode and imaging .....</b>	<b>98</b>
IV.3.1 Reflection mode.....	98
IV.3.2 Imaging.....	100
<b>IV.4/ Chapter conclusions.....</b>	<b>102</b>
References .....	103

## IV.1/ Introduction to cultural heritage studies

The study, preservation and restoration of cultural heritage materials and objects are crucial for obtaining important historical information and/or maintaining their aesthetic appeal. Inevitably and very often time, environmental exposure and other factors cause damage and deterioration. As a consequence the preservation of cultural heritage items requires the use of technological tools and the expertise of various specialists such as physicists, chemists, archaeologists, conservators and historians. The approach in cultural heritage studies can be divided in two distinctive steps. The first step consists of giving a rigorous diagnosis of the artwork under study and establishes if further actions are needed. The diagnosis appears to be also valuable in order to gain historical knowledge and understanding of ancient techniques. The second step, which depends on the diagnosis result, is the curative part, also known as the restoration work. Numerous spectroscopic tools, spanning from X-rays up to the mid-infrared, have been used for the analysis and restoration of cultural heritage materials, with laser-based approaches playing a major role [1]. Concerning the diagnosis various approaches have been developed and can be classified as invasive or non invasive. When dealing with highly valuable pieces, the diagnosis tool has to be non-invasive or if invasion cannot be avoided it has to remain on the microscopic scale.

An example of non-invasive technique is the Raman spectroscopy. Raman spectroscopy is a particularly good tool for the identification of inorganic species, offering sharp fingerprints traces. The analysis of organic species is rather more complex since Raman spectra tend to be not quite so straightforward to interpret to a level that allows unambiguous identification of materials. This is due to the broad band features that arise from organic components [2].

An example of microscopic invasive technique which brings multi-element analysis is the so-called Laser Induced Breakdown Spectroscopy (LIBS). Exceeding the laser-induced optical breakdown of a material leads to the formation of a transient micro plasma that emits light characteristic of the elements in the ablated solid. Time and spectrally resolved analysis of the plasma emission is straightforward giving valuable information about the elemental content of the sample. Furthermore, the invasion remains relatively small when considering that a single pulse from a nanosecond laser can provide full multi-element analysis with a spot size smaller than 100  $\mu\text{m}$  [2].

Finally an impressive demonstration of laser-based restoration has been presented in Ref. [3]. In this collaborative work between IESL-FORTH, ESMA (Committee for the Preservation of the Acropolis Monuments) and YSMA (Acropolis Restoration Service) a cleaning of the West Frieze of the Parthenon block no. 3 ( $\Delta Z$  III) has been demonstrated using a combination of ultraviolet and infrared laser irradiation.

The development of new non-invasive diagnostic tools for the use in the analysis of cultural heritage material is essential. Furthermore, the recent development of THz time domain spectroscopy has brought researchers from various disciplines, including chemistry, materials science, biology and

medicine to use THz time domain spectroscopy (THz-TDS) for applications ranging from semiconductor to DNA monitoring [4]. Thus, due to the unique properties of THz radiation, enumerated in the introductory chapter, it seemed rather obvious to apply THz imaging and spectroscopy to the field of art conservation.

Consequently in this chapter, we will present the application of THz-TDS spectroscopy in art which was a virgin field at the beginning of my thesis, since only some preliminary work using traditional FTIR spectroscopy has been done [5, 6]. The emphasis of our work has been made on paintings and the materials used for paintings [7]. Their analysis encompasses the characterization of their composition and structure; both aspects are of particular complexity due to the many materials of different chemical composition which are found within paintings as well as the multilayered and heterogeneous structure of most paintings. Paintings often contain pigments and colorants, mixed with a binding medium, which are applied in mixtures and in different strata over some kind of support, which maybe stone, wood, or plaster. In addition, many paintings are covered with layers of varnish. The complexity of the materials and mixtures used in the field is such that it demands careful preparation of samples. For instance parameters like sample type (film, powder or solution), degree of aging, humidity, and temperature control play a vital role and can influence the results. Moreover, multilayer structures found in paintings as well as highly absorbing media demand the use of THz systems with a large dynamic range, as it will be shown in the following. In an effort to assess the THz transmission properties of some painting materials and to contribute to the extension of THz spectroscopy to the analysis of cultural heritage materials, a first and crucial step is the characterization of some natural polymers which have been used extensively in painted artifacts. Many different binding media have been used for paint and for varnish and these include different glues and dairy products, resins and gums, plant oils and waxes. In this chapter, we will also present our investigations on the possibility to obtain an image of a hidden painting, as well as the possibility to obtain stratigraphic profile using the inherent time of flight parameter.

## IV.2/ Qualitative and quantitative analysis in transmission mode

### IV.2.1 Experimental approach and samples preparation

For this research, films of representative materials and thicknesses were prepared so as to classify the THz absorption of different art-related media: animal glue, egg yolk, linseed oil, mastic resin. Animal glues are composed of the protein collagen which is extracted from bones, skins and other tissues and are commonly found in the preparation of canvases for paintings and have been recommended as binding media for wall paintings[8]. For this study, films of ox bone glue were prepared and pigments were painted out using the same glue. Eggs represent another animal based binding medium which contains a mixture of both fatty acid esters (40%) and proteins (60%); upon evaporation and aging egg yolk forms a strong adhesive which has been used as a binding medium for

the execution of many easel paintings and icons, with particularly well known examples in the Italian Renaissance [8, 9]. Drying oils are another class of binding media, which set to form a hard film following polymerization and cross linking of unsaturated fatty acid esters. Not all oils are suitable for paint, but linseed oil, chosen for this research, is one of the most commonly used painting media and contains a mixture of palmitic, stearic, and C18 (oleic, linoleic and linolenic) acids. Finally, varnishes are usually composed of many different molecules, and in this study, a solid tree resin known as mastic was considered. This resin is based on a mixture of triterpenoids, which can be dissolved easily, and dries to form a transparent and protective film [10]. As varnishes are found on the surface of paintings, the absorption properties of these materials are of particular interest.

With the aim to apply THz spectroscopy to study realistic samples, which could include monitoring of paintings, we decided to study the samples in the form of thin films, having thicknesses close to those found in paintings. Films were deposited on 3 mm thick rectangular (60\*90mm<sup>2</sup>) Teflon substrates. Binding media were prepared according to traditional recipes [8, 9] and samples were naturally aged for 1 month prior to analysis. The recipes applied in this study were as follows: egg yolk sample- 2 gr. of pure egg yolk (purchased from a local market and manually separated from the white), with film thickness of approximately 600  $\mu\text{m}$ ; linseed oil sample- 0.5 gr. of a 0.5% diluted solution of linseed oil (Kremer Pigmente) in turpentine, with film thickness estimated around 230  $\mu\text{m}$ ; collagen (rabbit glue) sample- 2.5 gr. of 10% aqueous solution of solid rabbit skin glue (Kremer Pigmente), with film thickness around 120  $\mu\text{m}$ ; and varnish sample- 2.5 gr of 10% solution of Chios mastic (powdered) in dichloromethane, with film thickness around 400  $\mu\text{m}$ . Pigmented samples were prepared using both collagen and oil as binding media, and cobalt yellow as a pigment. Samples were painted out, on the same Teflon substrates, using a fine brush with paint made by mixing a pigment with a binding medium in order to achieve a suitable consistency to be applied in a single layer. One sample was prepared by mixing the pigment with a 5% solution of rabbit skin glue in a ratio of 3: 1 by weight and a second sample was made by mixing pigment with pure linseed oil in the same ratio. Therefore, upon drying, the paint made with rabbit skin glue contained less binding medium compared to the oil-based paint, which dries by photo-oxidation and crosslinking reactions rather than by evaporation of water.

The substrates were then placed in a metallic sample holder with a 50 mm diameter clear aperture centred and covering the whole collimated THz beam, as shown in Figure 57. In our approach we have used the unfocused THz beam, around 40 mm diameter, to probe the samples. This has allowed us to use large surfaces of the samples and obtain average values, which give more representative results. Also, this approach reduces the errors that could be induced by scattering problems that appear when a focused beam encounters large pigment particles. In our case, the films contained pigment particles that were smaller than 20  $\mu\text{m}$  and in most cases were of the order of less than 1  $\mu\text{m}$  in diameter. The time domain spectrometer used for this experiment is the first time domain spectrometer developed in our laboratory. This set-up was also based on the emission from 2-color

filament and a detection scheme using an electro-optic sampling method in a 1 mm ZnTe crystal. It differed from the previously described set-up (see chapter I) because we have used only two parabolic mirrors and the probe beam was introduced in the THz beam path through a tiny hole drilled at the centre of the refocusing parabolic mirror as depicted in Figure 57(c). The electric field and its subsequent Fourier transform were identical to the one presented in chapter II, since the same emission and detection scheme were used.

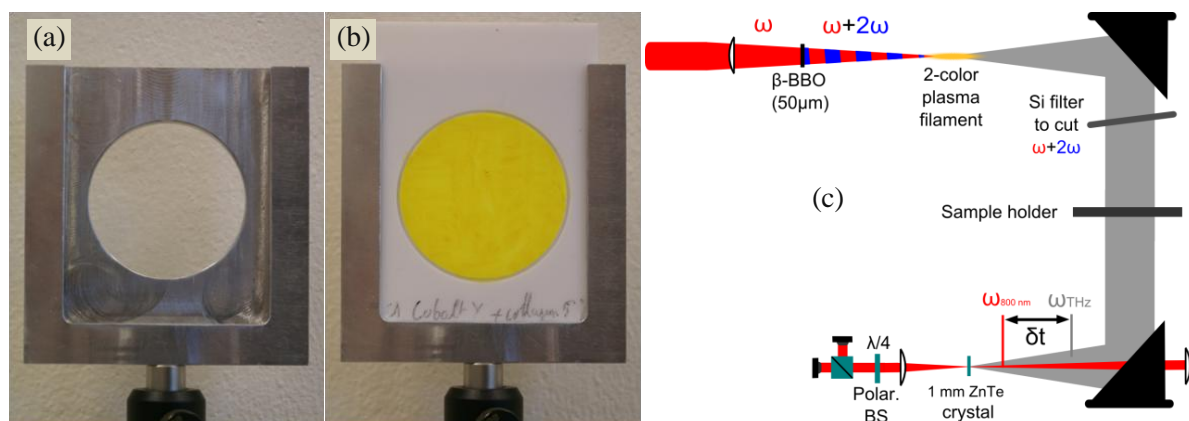


**Figure 57: (a) CCD picture of the sample holder without sample (b) CCD picture of the holder with a Cobalt yellow sample deposited on the Teflon substrate. (c) Schematic of experimental set-up.**

## IV.2.2 Experimental results

Transmission spectra have been recorded independently for each binding medium and are shown in Figure 58(a). Oil is the binding medium that absorbs least in the THz region, practically it can be considered as neutral. Egg yolk has the most profound absorption with a characteristic broad absorption peak at 2 THz. Collagen shows an intermediate absorption which increases with frequency. It is worth noting that varnish has a nearly flat response, but has non-negligible absorption (varnish thickness 400  $\mu\text{m}$ ). This could in some cases be a limiting factor, where multiple layers of varnish of significant thicknesses may cover a painting. In this case, THz-TDS can provide valuable means of revealing spectral details beneath the strong absorption of the covering varnish layers.

Following analysis of pure binding media, we recorded transmission spectra of pigments mixed with various binders in different concentrations. The mixtures of cobalt yellow with oil and with collagen are shown in Figure 58(b). The characteristic absorption peak of cobalt yellow at 3 THz is clearly recognizable in both cases. It is noticeable that the difference in the depth of the peak is due to the different concentrations of the pigment in the two cases, demonstrating that this technique provides quantitative as well as qualitative analysis. Spectra of pigment mixtures both with and without varnish layers have also been recorded, confirming the resolving power of our system.

In order to further demonstrate the advantages of our approach, we have performed comparative measurements between our THz-TDS and an FTIR spectrometer system (BRUKER IFS 66v/s). For low absorbing media the two techniques yield similar results. Yet, when it comes to media

with higher absorption and/or thicknesses the low signal-to-noise ratio FTIR system quickly reaches its limits while our powerful THz-TDS can still resolve the absorption spectra, as shown in Figure 58(c) for the case of egg yolk. Furthermore, the absorption spectra of various substrates commonly used in art have been measured using the FT-IR spectrometer. As one can see from Figure 58(d), the widely used substrates which are canvas and skins are fully absorbing the THz radiation.

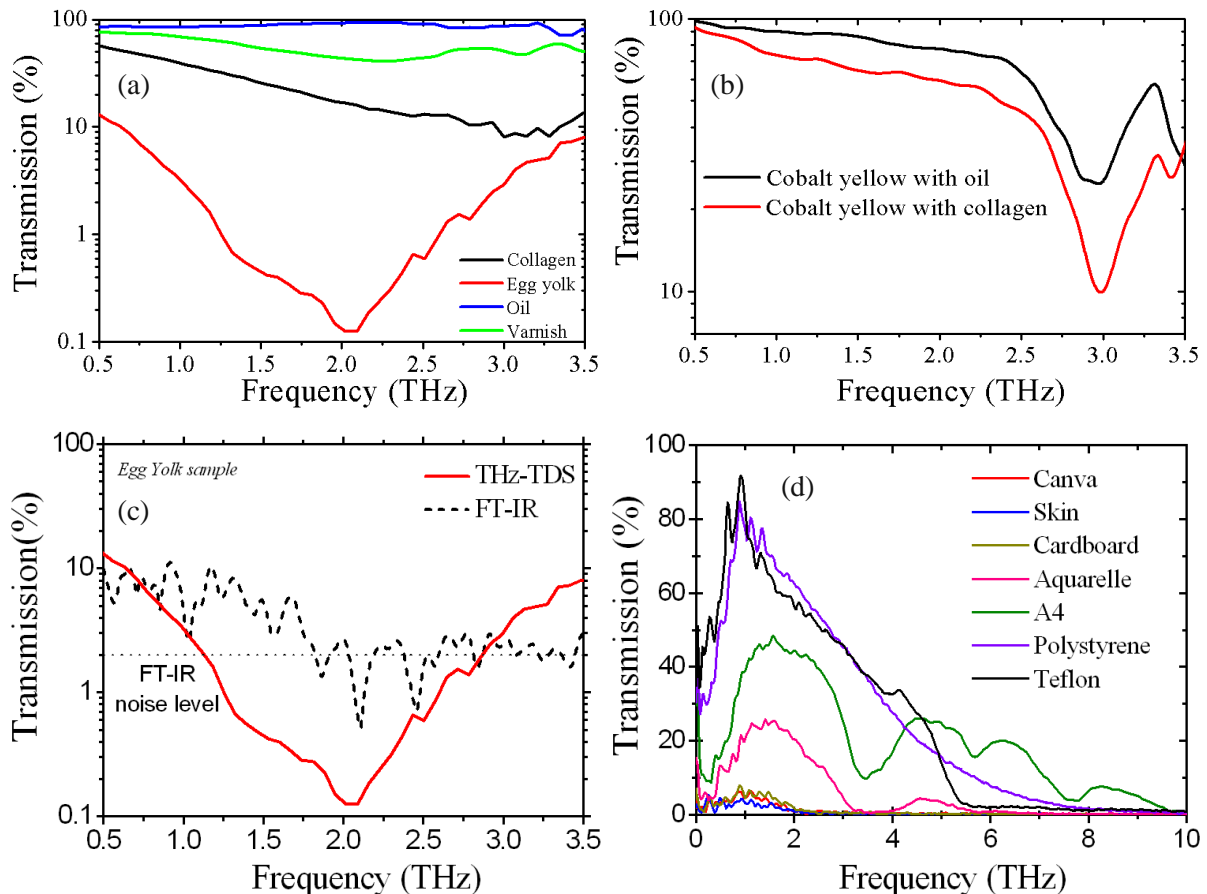


**Figure 58: (a) Transmission of various binding media and varnish. (b) Pigment mixed with different binding media. (c) Comparison between traditional FTIR and THz-TDS. (d) FTIR measurement of various substrates.**

This observation is yet another illustration of the necessity to use a THz-TD spectrometer with high signal to noise ratio if the measurement are done in transmission. Nevertheless, this inconvenience linked to a highly absorptive substrate may be avoided while making measurement in a reflection mode. Temperature and humidity control is of vital importance for the technique. Both of these parameters can change dramatically the recorded structures, and fluctuations in ambient conditions can hinder reproducibility of results. Specifically, as we have already discussed, water strongly absorbs THz radiation while temperature variations can modify the absorption bands. This is because most absorption observed in the THz range for solid media are related to collective vibrational, rotational and torsional modes of molecular complexes and chains, which are strongly dependent on the temperature of the medium [11]. For the same reason, the observed absorption

structures are broad at room temperatures (as shown here at 22 C°). This suggests that, further studies should be performed in order to explore the role of material aging, humidity content and temperature dependence of THz absorption spectra. Furthermore, a recent report has demonstrated the possibility to distinguish small differences in a white pigment originating from different producers [12]. This discrimination of pigment powder has been possible by relating the absorbance of the calcium carbonate (CaCO<sub>3</sub>) crystal with its shape and the presence of impurities.

## IV.3 / Analysis in reflection mode and imaging

### IV.3.1 Reflection mode

The analysis in reflection mode is primordial, if one targets the use of THz radiation in a museum environment. Indeed it is rather complicated to move pieces of art of high value. If one is willing to get information from a painting, most of the time it has to be done in-situ. Consequently, it appears absolutely necessary to obtain information in a reflection mode and demonstrate the proof of principle. For this experiment, we used our last developed time domain spectrometer, that we modulated in reflection mode as presented in Figure 59. In this approach, the sample was placed at 45 degrees at the focusing position and the reflected THz radiation was collected at 90 degrees via a parabolic mirror placed exactly at one focal length. Then a flat gold coated mirror directed the collimated THz beam to the last focusing parabolic mirror and the detection scheme.

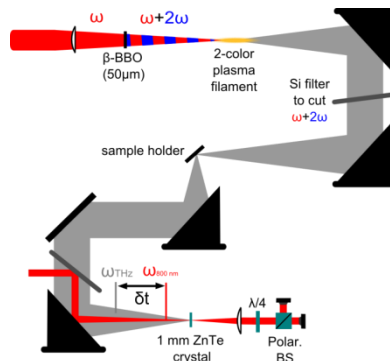


**Figure 59: Schematic of the experimental set-up in reflection mode.**

In order to prove the feasibility of reflection measurement and the potential gain of this approach, we first decided to measure the possibility to obtain information on the varnish covering layer. Within the conservator community, it seems important to gain information on the presence of a thin layer of varnish covering a painting. The varnish sample described in the previous section was then placed at the focusing and the electric field was recorded. In order to compare, an identical bare Teflon substrate sample was also investigated. Figure 60(a) presents the recorded THz electric field for both samples where the black curve corresponds to the bare substrate. As one can see, there is a first peak which corresponds to the front surface of the Teflon and around 15 ps later, there is a second peak which corresponds to the back surface of the Teflon substrate. Once the Teflon substrate

is covered with a layer of varnish the results differ. The first electric field peak is higher and wider, which suggests that the varnish has higher reflectivity than the Teflon. More interestingly the second peak arising from the back surface of the Teflon substrate is delayed. Figure 60(b) shows a cropped time window of the second electric field peak, which clearly allows to measure the time delay induced by the varnish layer. This delay corresponds to two round trips within the varnish layer and is equal to 175 fs.

Furthermore, an attempt to distinguish two successive layers of paint has been done. For this experiment, two pigments were painted on a classic paper sheet. The first pigment is a synthetic pigment first introduced in 1920 and named Titanium white ( $\text{TiO}_2$ ). This pigment is important in the diagnosis of art pieces, since it allows the detection of fake pieces. A remarkable example is presented in [2], where a LIBS analysis of a piece of art dating from 1903 demonstrated the presence of Titanium white, which revealed the falsification. The second pigment was a natural mineral pigment used since the antiquity and named yellow ochre. Elements such as Fe, Si, Al have already been identified in its composition. Each of the layers of paint has been spread separately on a thin piece of paper and they were then suspended on a free standing mount. The results are presented in Figure 61(a) and Figure 61(b). First, one can see that once the yellow ochre is on top of the Titanium white, it is possible to distinguish a second pulse which corresponds to the white titanium layer. The other way around is not obvious, since only one but much bigger peak is distinguishable. This seems to be due to a higher reflectivity from the white titanium which prevents from distinguishing the yellow ochre. This experiment suggests that it may be difficult to discriminate different layers of paint when placed one above the other. Nevertheless, if layers are appropriately thick and the first layer not too reflective, it would be possible to obtain a stratigraphic profile of a painting. This exact experiment has been reported recently, with clear images of a paint profile [13]. Such time of flight measurements have also been successfully used in combination with a technique of shearography, in order to get detailed information from wooden panel paintings [14]. In this report, the authors were able to observe defects hidden behind the painting which provide valuable information in view of proceeding to restoration work.

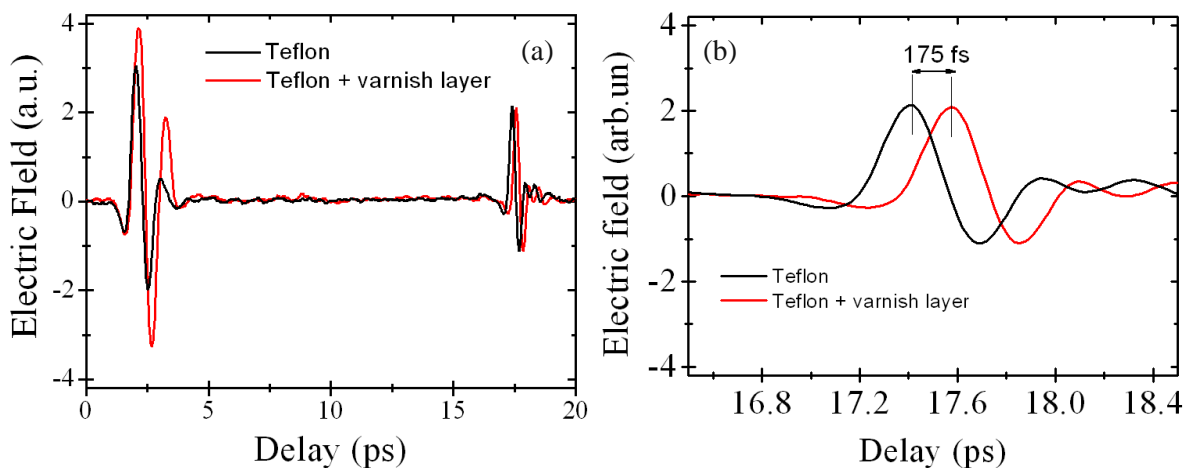


**Figure 60: (a) Time domain trace of a bare Teflon substrate and a substrate recover with a varnish layer. (b) Close-up on the second peak of the time domain trace of (a).**

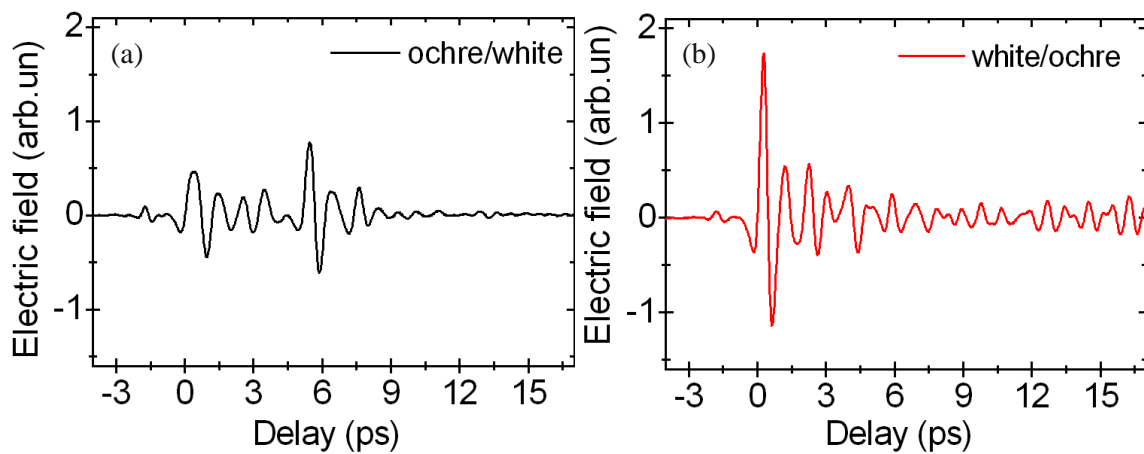


**Figure 61: (a) measured electric field of a layer of titanium white on top of a yellow ochre layer. (b) Measured electric field of yellow ochre layer on top of a titanium white layer. In both cases and each layer has been spread on a separated piece of normal A4 paper.**

### IV.3.2 Imaging

As presented in the introduction chapter, THz science became an extremely popular field of research since the first demonstration of THz imaging. This has brought tremendous amount of work and technological developments towards bringing THz imaging to the real world. In order to continue our work on the diagnosis of cultural heritage material, the demonstration of the THz imaging is an essential step to achieve. For this reason, we decided to image a paint drawing hidden at the back side of a thick Teflon substrate. The paint used for this sketch was Mars Black Acrylic and the painted schematic is shown on Figure 62(a). The sample was mounted on an X-Y translation stage and the THz beam was first passing through the bare surface of the sample as depicted in Figure 62(b). The THz electric field was recorded at different points in X-Y space. The electric fields were then Fourier transformed and each spectrum was integrated. The highest and lowest integrated values were then identified in order to establish the limit of a gray scale. Each of the integrated values was then placed in a matrix corresponding to their position in X-Y space and then the image was reconstructed. The spectral contrast image obtained is presented in Figure 63.

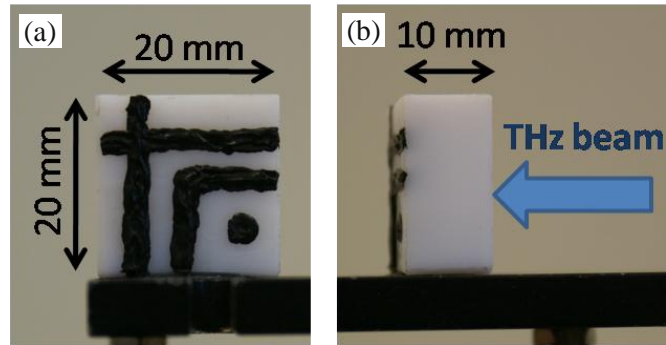


**Figure 62: (a) CCD picture of the sample back surface with the painted sketch. (b) CCD picture of the sample side.**

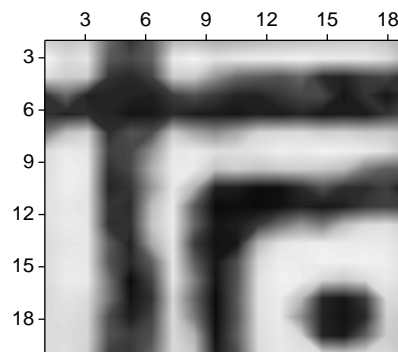


**Figure 63: THz spectral contrast image obtained.**

As a result, a good agreement was obtained and the painted sketch is clearly visible on the THz image. The resolution was limited because of the wavelength size which is around  $300\ \mu\text{m}$ , but can be improved using a near field scanning technique as discussed in chapter I. Nevertheless, this demonstrates the possibility to obtain images of hidden objects as long as the used substrate is at least partially transparent to THz radiation. Furthermore, we developed a Labview program in order to automate the acquisition of multiple scans and reconstruction of the measured image. The demonstration of imaging a hidden drawing behind a 4 mm layer of plaster has been shown in [15]. In this work, the authors have used the same approach of power integration of the spectral information. The same group has also recently demonstrated the use of THz pulse imaging for dendrochronology study [16]. Furthermore, a demonstration of broadband imaging of documents written with lead pencils has also been reported [17]. This report as well as the results presented above clearly suggest that it is possible to obtain visualization of sketches of original painting beneath layers of paint.

## IV.4/ Chapter conclusions

The application of THz science to the field of cultural heritage preservation has been subject of a growing interest in the last 3 years. From the initial work consisting of spectroscopic analysis of various components [7], the field moved towards imaging of hidden layers and observations of hidden defects. Most of the proofs of principle have been already demonstrated and now the field is mainly depending on the technological development that will be brought to the sources. We identified two key points for an application of the THz technique to the cultural heritage field. Firstly, the need for a portable device is absolutely essential. Efforts have been done in this direction with the recent development of a real-time imaging portable system using a quantum cascade laser source and a micro bolometer focal plane detector array [18]. This device can bring valuable information for identification of pigments. Nevertheless, it does not offer the possibility to image hidden drawing or layers of paints since it does not measure the time domain trace of the electric field. Consequently and secondly, the portable device needs to offer a time domain measurement. With the recent development of fiber amplified lasers, it seems possible to develop such a compact time domain system. The main limitation in THz-TDS remains the acquisition time needed to scan a large area. This can be circumvented by using fast oscillating delay lines, or as presented above by using a powerful source that will allow expanding the THz beam in order to scan large areas.

## References

1. C. Fotakis, D. Anglos, V. Zafiropoulos, S. Georgiou, and V. Tornari, "Lasers in the Preservation of Cultural Heritage: Principles and Applications," (Taylor & Francis, New York) (2006).
2. S. Georgiou, D. Anglos, and C. Fotakis, "Photons in the service of our past: lasers in the preservation of cultural heritage," *Contemporary Physics* 49, 1-27 (2008).
3. A. Nevin, P. Pouli, S. Georgiou, and C. Fotakis, "Laser conservation of art," *Nature Materials* 6, 320-322 (2007).
4. B. Ferguson and X. C. Zhang, "Materials for terahertz science and technology," *Nature Materials* 1, 26-33 (2002).
5. K. Fukunaga, Y. Ogawa, S. Hayashi, and I. Hosako, "Terahertz spectroscopy for art conservation," *IEICE Electron. Express* 4, 258-263 (2007).
6. I. Hosako, N. Sekine, M. Patrashin, S. Saito, K. Fukunaga, Y. Kasai, P. Baron, T. Seta, J. Mendrok, S. Ochiai, and H. Yasuda, "At the dawn of a new era in terahertz technology," *Proc. IEEE* 95, 1611-1623 (2007).
7. J. M. Manceau, A. Nevin, C. Fotakis, and S. Tzortzakis, "Terahertz time domain spectroscopy for the analysis of cultural heritage related materials," *Applied Physics B-Lasers and Optics* 90, 365-368 (2008).
8. C. Cennini, "The Craftsmen's Handbook, Translation of Il'Libro dell'Arte," New Haven: Yale University Press(1936).
9. D. V. J. Thompson, "The Practice of Tempera Painting " (New Haven: Yale University Press. 1946).
10. R. White and J. Mills, "The Organic Chemistry of Museum Objects " (London: Butterworth Heinemann, 1999).
11. M. B. Johnston, L. M. Herz, A. L. T. Khan, A. Kohler, A. G. Davies, and E. H. Linfield, "Low-energy vibrational modes in phenylene oligomers studied by THz time-domain spectroscopy," *Chemical Physics Letters* 377, 256-262 (2003).
12. M. Mizuno, K. Fukunaga, S. Saito, and I. Hosako, "Analysis of calcium carbonate for differentiating between pigments using terahertz spectroscopy," *J. Eur. Opt. Soc.-Rapid Publ.* 4, 4 (2009).
13. A. J. L. Adam, P. C. M. Planken, S. Meloni, and J. Dik, "TeraHertz imaging of hidden paintlayers on canvas," *Opt. Express* 17, 3407-3416 (2009).
14. R. M. Groves, B. Pradarutti, E. Kouloumpi, W. Osten, and G. Notni, "2D and 3D non-destructive evaluation of a wooden panel painting using shearography and terahertz imaging," *NDT & E International* 42, 543-549 (2009).
15. J. B. Jackson, M. Mourou, J. F. Whitaker, I. N. Duling, S. L. Williamson, M. Menu, and G. A. Mourou, "Terahertz imaging for non-destructive evaluation of mural paintings," *Optics Communications* 281, 527-532 (2008).
16. J. B. Jackson, M. Mourou, J. Labaune, J. F. Whitaker, I. N. Duling, S. L. Williamson, C. Lavier, M. Menu, and G. A. Mourou, "Terahertz pulse imaging for tree-ring analysis: a preliminary study for dendrochronology applications," *Meas. Sci. Technol.* 20, 10 (2009).
17. E. Abraham, A. Younus, A. El Fatimy, J. C. Delagnes, E. Nguema, and P. Mounaix, "Broadband terahertz imaging of documents written with lead pencils," *Optics Communications* 282, 3104-3107 (2009).
18. K. Fukunaga, N. Sekine, I. Hosako, N. Oda, H. Yoneyama, and T. Sudoh, "Real-time terahertz imaging for art conservation science," *J. Eur. Opt. Soc.-Rapid Publ.* 3, 4 (2008).

*Chapter V: Time Domain Spectroscopy for  
dynamical studies of metamaterial*

<b>CHAPTER V: TIME DOMAIN SPECTROSCOPY FOR DYNAMICAL STUDIES OF METAMATERIAL.....</b>	<b>104</b>
<b>V.1/ Introduction to metamaterial science .....</b>	<b>106</b>
V.1.1 Historical overview.....	106
V.1.2 Negative $\epsilon$ and $\mu$ .....	107
a) Negative $\epsilon$ .....	107
b) Negative $\mu$ .....	108
<b>V.2/ Split Ring Resonator (SRR) all-optical switch.....</b>	<b>110</b>
V.2.1 SRR electrical response characterization.....	110
V.2.2 Dynamical control of the electrical response .....	112
a) SRR switch .....	112
b) Frequency shift and broadband phase plate.....	113
c) Simulations .....	114
<b>V.3/ Mode shifting.....</b>	<b>117</b>
V.3.1 eSRR design and fabrication .....	117
V.3.2 Experimental results.....	118
V.3.3 Simulations .....	119
<b>V.4/ Chapter conclusions .....</b>	<b>121</b>
References .....	122

## V.1/ Introduction to metamaterial science

### V.1.1 Historical overview

Metamaterials are artificially structured sub-wavelength materials which exhibit peculiar electromagnetic response not seen in naturally occurring media. Because visible light has a wavelength that is hundreds of times larger than the atoms that compose any material, the atomic details lose importance in describing the interaction between the light and the material. In practice, it means one can average over the atomic scale characterizing a material by just two macroscopic electromagnetic parameters: the electric permittivity  $\epsilon$  and the magnetic permeability  $\mu$ . These two electromagnetic parameters do not strictly depend from the response of atoms or molecules. Any collection of objects whose size and spacing are much smaller than the light wavelength can be described by a  $\epsilon$  and  $\mu$ . Consequently, this suggests that carefully designed sub-wavelength structures can be incorporated to a specific material in order to exhibit tailored  $\epsilon$  and  $\mu$  with simultaneous negative values [1]. The first article introducing the concept of simultaneously negative  $\mu$  and  $\epsilon$  was done by Veselago more than 40 years ago and already showed that in principle it should lead to negative refractive index [2].

Despite the exciting result presented in this paper, interest in negative index materials vanished and this result could not be proven experimentally because no known material exhibits such properties. It is only in 1999, that was done the first demonstration of an effective magnetic permeability  $\mu_{\text{eff}}$  using microstructures built from nonmagnetic conducting sheets [3]. There, the effective magnetic permeability was shown to be tuned to values not accessible in naturally occurring materials, including large imaginary components of  $\mu_{\text{eff}}$ . Following this precursory work, the first demonstration of simultaneous negative  $\epsilon$  and  $\mu$  was done [4] using a composite structure based on the split ring resonator (SRR) design already introduced in [3]. The negative  $\mu$  occurred at frequencies above the resonance frequency of the SRR structure. The negative  $\epsilon$  was introduced by adding a lattice of conducting wires to the SRR lattice. Shortly after, Pendry demonstrated theoretically the possibility to obtain a perfect lens using negative refraction, in what is to date the most popular paper in the field [5]. In the continuity of this work, the last two decades have seen an exponential growth of the research on metamaterials, as literature attests it. Fundamental and applied research, spanning from radio frequencies to optical wavelengths [6] have demonstrated a variety of interesting phenomena, such as negative refraction [7], sub-diffraction limited imaging [8] and electromagnetic cloaking [9]. More recently, considerable advances have been made on research related to terahertz metamaterials and have led to the development of various metamaterial components to control the THz radiation properties. Components, such as frequency tunable filters[10, 11], all-optical switches and modulators[11-13], and perfect absorbers[14], have already been demonstrated experimentally. Recently, an efficient phase shifting device in the THz range has been demonstrated [15], with an

achievable phase change over a narrow band of frequency (23 GHz). Also, specifically designed metamaterial structures have been proposed for THz polarimetric devices [16].

### V.1.2 Negative $\epsilon$ and $\mu$

#### a) Negative $\epsilon$

The electric response of natural conductive materials typically takes place at high frequencies, i.e., at the visible or UV band for metals. This is evident from the electrons plasma frequency  $\omega_{ep}$ , which can be formulated as:

$$\omega_{ep}^2 = \frac{ne^2}{\epsilon_0 m_{eff}},$$

where  $n$  is the electron density,  $e$  is the electron charge,  $\epsilon_0$  is the vacuum permittivity, and  $m_{eff}$  is the electron effective mass. For example, gold with an electron density of  $5.9 \times 10^{22} \text{ cm}^{-3}$  has a plasma frequency located at approximately 138 nm or within the far UV range. In order to achieve an electric response at a lower frequency range, e.g., in the THz region, the plasma frequency must be modified. According to the above equation the plasma frequency can be reduced through changes in the electron density and effective mass. A metamaterial structure made of an array of thin metallic wires, similar to that shown in Figure 64(a), is a workable solution [8]. In such a structure, the electron density  $n$  is diluted due to the sparseness of metal in a unit cell. Furthermore, the electron effective mass  $m_{eff}$  is intensified because of the apparent mutual inductance of the wires that exerts a force on the electrons. From the analysis, given that  $a$  is the array spacing and  $r$  is the wire radius, the plasma frequency of the structure now becomes [17, 18]:

$$\omega_{ep}^2 = \frac{2\pi c_0^2}{a^2 \ln\left(\frac{a}{r}\right)},$$

where  $c_0$  is the velocity of light in vacuum. It is clear that the plasma frequency of the structure can be manipulated merely through its dimensions,  $a$  and  $r$ . By assuming infinite wire length, the structure can be characterized by an effective permittivity that takes on a Drude model:

$$\epsilon_{eff}(\omega) = 1 - \frac{\omega_{ep}^2}{\omega^2 + j\Gamma\omega},$$

where  $\Gamma$  is responsible for the propagation loss. At  $\omega < \omega_{ep}$  the permittivity becomes negative.

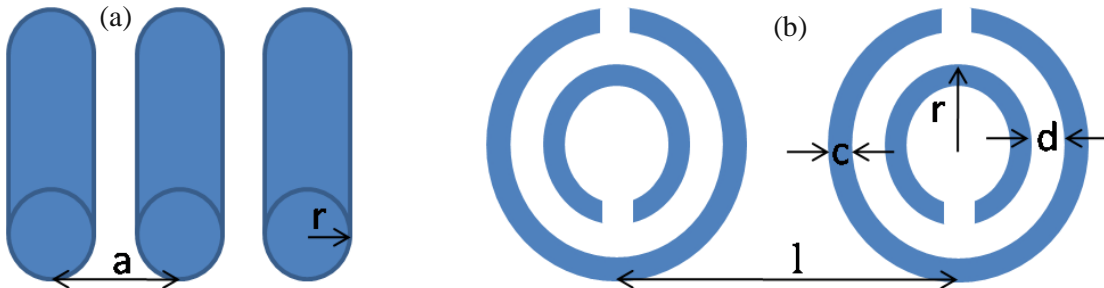


Figure 64: (a) thin wires planar array. (b) SRR planar array.

### b) Negative $\mu$

Magnetism is obtainable from nonmagnetic materials, provided that the materials can support current loops that bring about a magnetic dipole moment. By adopting this principle, SRRs, which feature sub-wavelength conducting loops, can have a magnetic response under the proper alignment of the electromagnetic waves [3]. As shown in Figure 64(b), a unit cell of the original double SRRs is basically composed of two concentric metallic rings with opposite splits or gaps. When the SRR is coupled to a magnetic field component oscillating in the axial direction, the ring establishes a current flow, which further builds a magnetic dipole parallel or antiparallel to the magnetic field. The loop inductance and gap capacitance are equivalent to an LC resonant circuit, causing a strong magnetic response at its resonance. The inner concentric ring contributes to the net capacitance of the double SRR and thus lowers the resonance frequency. Hence, this ring boosts up the ratio between the operating wavelength and lattice constant, making the SRRs appear more homogeneous to the electromagnetic excitation. In spite of this, the inner ring can be removed without a significant impact on the SRR's function while shifting the resonance frequency. A metamaterial structure composed of periodically aligned SRRs under a magnetic excitation can be described by an effective magnetic permeability with a Lorentzian model [3]:

$$\mu_{eff}(\omega) = 1 - \frac{F\omega^2}{\omega^2 - \omega_{m0}^2 + j\Gamma\omega},$$

where  $\omega_{m0}$  is the magnetic resonance frequency,  $\Gamma$  represents the energy dissipation, and  $F$  is the fill factor of the SRR. The magnetic resonance frequency is related to the SRR's geometry through [3]:

$$\omega_{m0}^2 = \frac{3lc_0^2}{\pi \ln \frac{2c}{d} r^3},$$

The magnetic plasma frequency is where the permeability crosses zero and is given by:

$$\omega_{mp}^2 = \omega_{m0}^2 / (1 - F)$$

At frequencies lower than the resonance the SRRs have a positive response to the magnetic field, and between the resonance and plasma frequencies, the response becomes negative. Therefore, the structure can support para-magnetism  $\mu_{eff} > 1$  and diamagnetism  $\mu_{eff} < 1$ , including a negative permeability.

In order to obtain simultaneous negative  $\epsilon$  and  $\mu$ , careful design of the structure must be done. Since, a lattice of wires possesses a cut-off frequency below which  $\epsilon$  is negative [17]; by choosing the parameters of the wire lattice such that the cutoff frequency is significantly above the SRR resonant frequency, the composite can have an overlapping region where both  $\epsilon$  and  $\mu$  are negative.

In this chapter, we report in the first section on the ability to obtain tunable electric resonance responses in the THz regime, as well as a broadband ( $\sim 250$  GHz) phase tunability (over  $\pi/4$ ), using classical metamaterials consisting of metallic SRRs on the top of a semiconductor substrate [19]. In the second section, we explore experimentally a new metamaterial design, and we demonstrate for the first time to our knowledge, a blue-shift optical switching effect. All the experimental results presented in the following pages have been obtained in our laboratory, while all the simulations have been obtained from the Metamaterials group of our Institute with which we collaborate on these projects.

## V.2/ Split Ring Resonator (SRR) all-optical switch.

### V.2.1 SRR electrical response characterization

The metamaterial sample studied in this work is the same as the one presented in Ref. [12]. It consists of an array of SRRs, fabricated from copper, deposited on 670  $\mu\text{m}$  thick, high resistivity GaAs substrate. The exact dimensions of the SRRs are given in Figure 65(a). Figure 65(b) shows a view of an array of 9 SRRs and the dimension of a unit cell (50  $\mu\text{m}$ ) is depicted with a black square. To characterize the electrical response of this sample, we used our THz time domain spectroscopy, previously described in details. The sample was placed at the focusing point of the THz beam and at a normal incidence. Thus, two orientations can be defined, which depend on the orientation of the sample gap with the THz electric field. The orientation presented in Figure 65(a) is the perpendicular orientation where the electric field of the THz beam (yellow arrow) is perpendicular to the sample gap. Upon rotating the sample by 90°, the sample is placed in the parallel configuration.

Figure 66(a) shows the electric field measured with the bare GaAs substrate which will be used as reference and also the electric fields transmitted through the sample for both orientations. The curves have been translated vertically for clarity. A clear deformation of the time domain trace is observable once the THz beam goes through the sample. We applied a Fourier transform to these electric fields and we obtained the spectral information, as presented in Figure 66(b). Hence, we could divide each spectrum with the reference spectrum ( $t(\omega) = E_{\text{sample}}(\omega)/E_{\text{ref.}}(\omega)$ ) in order to obtain the spectral transmission for each orientation, as presented in Figure 66(c). For the case of perpendicular orientation, two clear resonances are observable at respectively 0.5 THz ( $\omega_0$ ) and 1.6 THz ( $\omega_1$ ). According to simulations [12], the absorption at  $\omega_0$  corresponds to the surface circulating current produced from the incident time varying electric field which generates a magnetic field polarized parallel to the surface normal of the SRR. Since the SRRs are bianisotropic, the electric and magnetic responses of the SRRs are occurring at the same frequencies. Further experiments in [12] have shown that by tuning the angle of incidence, the magnetic resonance at  $\omega_0$  could be clearly identified. It is also important to note that in our case the low frequency side (below 0.5 THz) is much more absorbed than in [12].

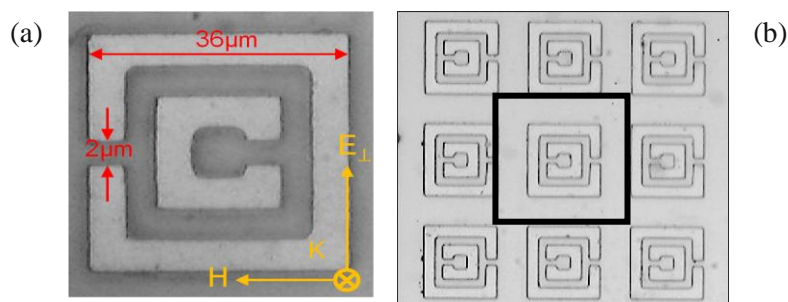


**Figure 65: (a) Microscope picture of one unit cell split ring resonator and its dimensions. (b) Microscope picture of an array of 9 SRRs.**

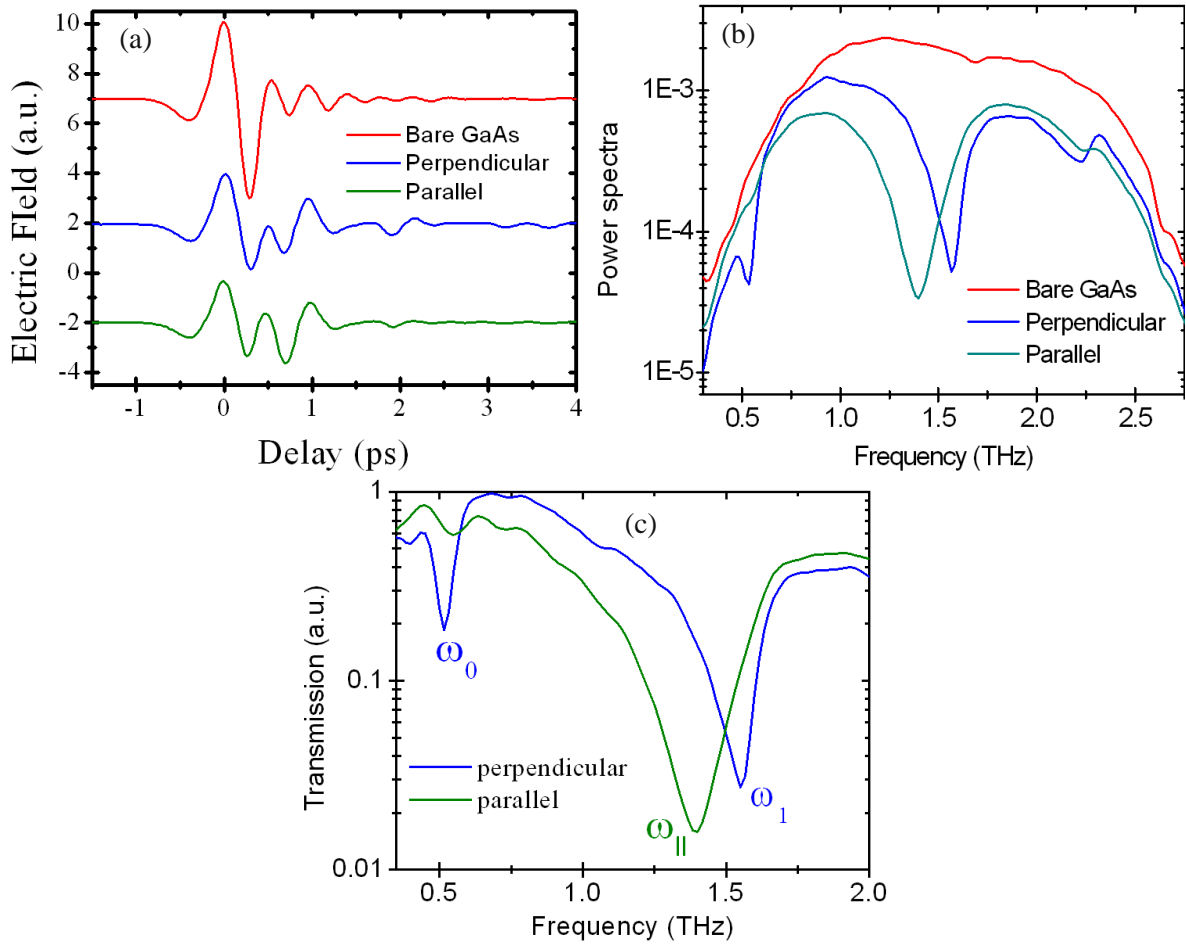


**Figure 66: (a) Measured electric field for the bare substrate, the perpendicular and the parallel orientation. (b) The Fourier transform of the electric field presented in (a). (c) Transmission spectrum for both orientations.**

Furthermore from [12], the  $\omega_1$  absorption corresponds to the half-wave resonance due to one side length of the SRR (36  $\mu\text{m}$ ), as the surface current simulation showed it. For the other sample orientation, the electrical response is completely different and only a single broad absorption line at 1.4 THz is observed ( $\omega_{||}$ ). Simulations in [12] have demonstrated that this resonance is equivalent to  $\omega_1$  and the frequency red-shift is attributed to the presence of two side length aligned with the THz electric field. We can conclude here, that in general the observed electrical response of the metamaterial sample is in good agreement with the previous report in literature.

## V.2.2 Dynamical control of the electrical response

The main interest for this sample besides the simultaneous negative  $\mu$  and  $\epsilon$ , comes from the fact that the substrate is a semiconductor. Consequently it provides the opportunity to dope the substrate and obtain different electrical responses. To study the dynamic electrical response of the metamaterial, an optical-pump beam was used to excite photocarriers in the GaAs substrate. This optical beam was extracted from the probe beam and its temporal synchronization with the THz beam was done using a manual delay line. The sample was placed as for normal incidence and at the focus of the THz beam (Figure 67). At this point the THz beam spot's diameter measured about 1 mm. The optical pump was launched unfocused at  $45^\circ$  on the sample (6.6 mm FWHM). The temporal synchronization of the THz and the optical pump beams has been experimentally defined. Afterwards, the THz pulse was delayed to assure a 5 ps average (because of the angle between the two beams) delay between them. This 5 ps delay was used to assure a quasi-steady state of the injected photocarriers, since they have a life-time in the nanoseconds regime.

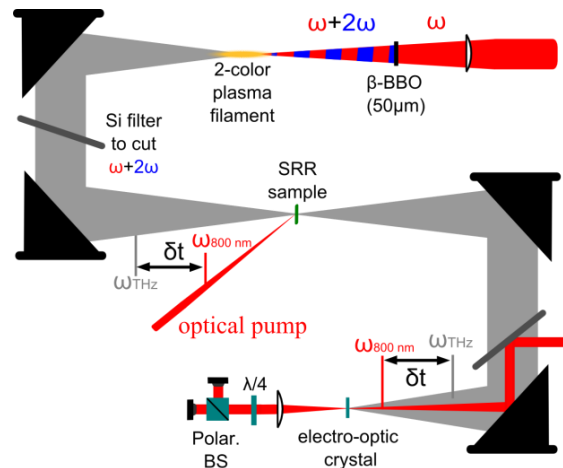


**Figure 67: Schematic of the TDS experimental set-up and the extra optical pump beam.**

### a) SRR switch

The dynamical study of the SRR with its gap perpendicularly-orientated to the THz electric field has been conducted for different level of photoexcitation. The results are presented in Figure 68(a). As one can see the  $\omega_0$  electrical resonance is gradually decreasing as more photocarriers are injected within the substrate, passing from 18% transmission to 42%. This figure is rather small compare to the one observed in [12] which was equal to 55%. The fluence of the optical beam has been measured accurately using a joule meter placed at the sample position. Nevertheless, the other resonance is quasi not affected about the injection of photocarriers with a decrease in the absorption less than 10% as expected in [12] and the general transmission is decreasing at other frequencies for higher optical pump fluency. An interesting point which can be observed from our experimental data is the slight blue-shift observed on  $\omega_1$ . This shift in frequency was also observed in [12], but its origin

has not been yet addressed. In order to identify the origin of this shift, we have measured the electric field going through the bare GaAs substrate for different levels of photocarriers.

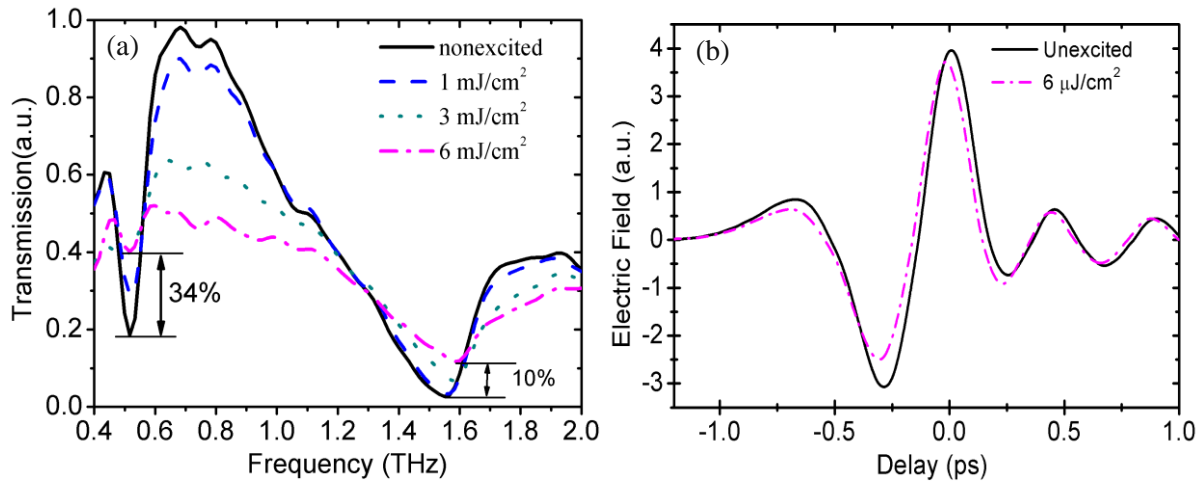


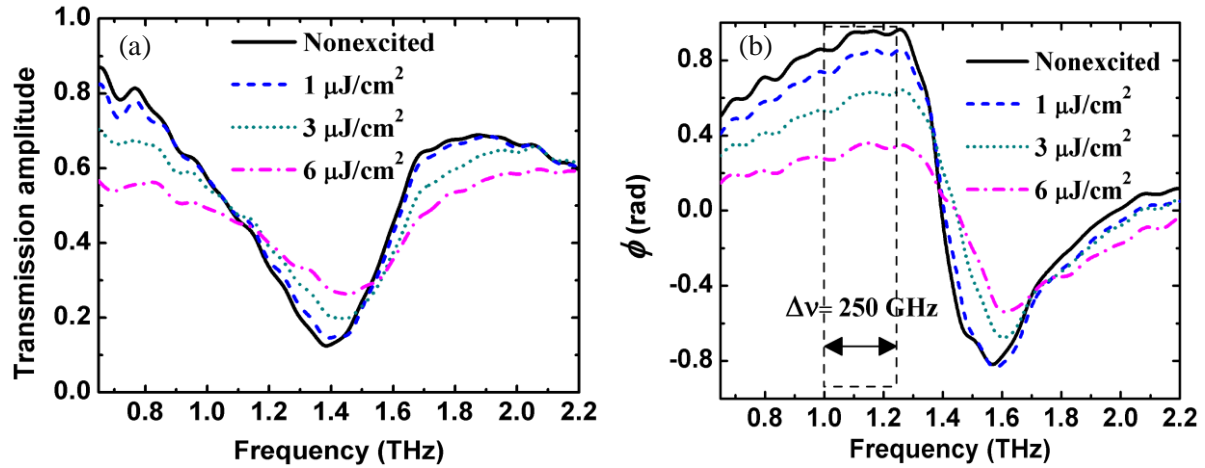
**Figure 68: (a) Experimental transmission amplitude spectra for the perpendicular orientation case at different level of photoexcitation (b) Measured electric field of the bare GaAs substrate at two levels of photoexcitation.**

As Figure 68(b) shows, the electric field recorded in case of high optical pump fluency arrives 20 fs earlier than in the case of no excitation. Such effect was also reported in [20], and was attributed to the variation of refractive index at the interface between air and GaAs sample. In order to fully attribute this shift to the change of the substrate dielectric parameter, we have decided to investigate the behavior of the parallel orientation electrical response as function of the photocarriers injection, which has not been yet reported in the literature.

#### b) Frequency shift and broadband phase plate

In the same experimental approach than the one described above, we measured the THz electric field for different levels of excitation fluence in the case of parallel orientation. The results are shown in Figure 69. The first observation from Figure 69(a) is the presence of an amplitude modulation of the resonance when photocarriers are excited. This broad resonance is the dipole-like resonance of the structure, related to the finite length of the metallic element along the electric field direction; thus, its amplitude modulation cannot be related to the short-circuit phenomenon observed for the magnetic resonance frequency ( $\omega_0$ ) shown in [12]. Instead, this phenomenon should be related to the change of conductivity of the substrate, where increasing amounts of charges finally screens the existing resonance. More interestingly, it is also possible to observe a frequency shift towards higher values (up to 50 GHz) as photo-carriers are injected within the substrate (see Figure 69(a)). This observation is similar to the one with perpendicular orientation. As electrons and holes are created under photo-excitation within the substrate (over one penetration depth; 1  $\mu\text{m}$  at 800 nm), the complex index of refraction is expected to change as well and can explain the experimental observations,

except from changes in the conductivity. Before moving to the theoretical analysis, let us consider the phase information from the experimental data. By determining the ratio between the extracted phase with and without photo-injection of carriers, one can characterize the phase shift,  $\Delta\Phi$ , produced by the photo-excitation of the sample.



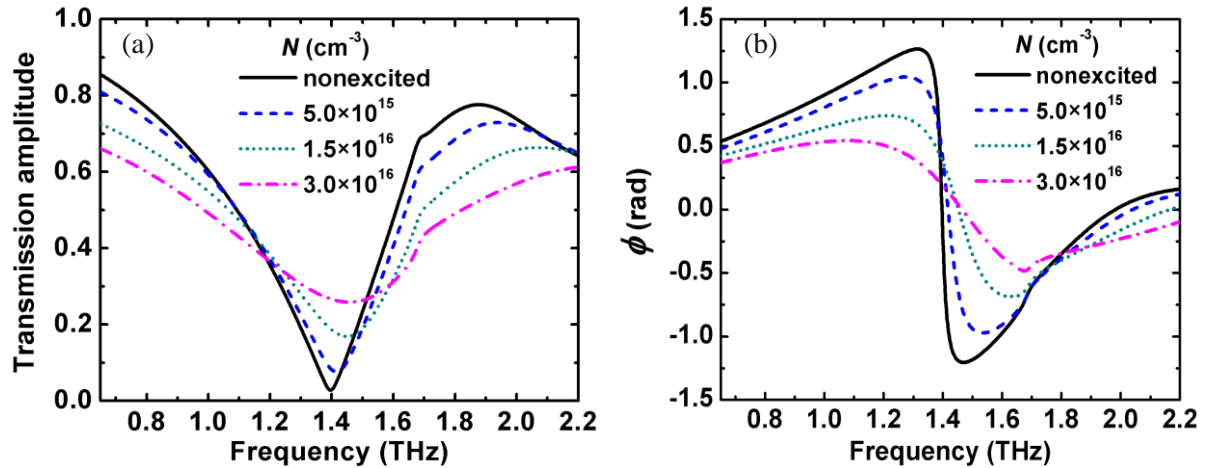
**Figure 69: (a) Experimental transmission amplitude spectra for the parallel orientation case and (b) phase tunability for different level of photo-excitation.**

Figure 69(b) clearly shows an almost flat phase shift extending over a very broad range of frequencies (from 1 to 1.25 THz), just before the anomalous phase shift on the resonance. The phase shift amplitude decreases as the photo-excitation becomes more important, forming practically a tunable THz wave-plate. Although the losses are not negligible, this is still a remarkable result, considering that this level of phase shift is achieved over a very broad spectral range and for a non-specifically designed or optimized metamaterial.

### c) Simulations

To understand the origin of the frequency and phase tunability, we first conducted a series of simulations. The theoretical study of our metamaterial system was performed using the finite-integration technique, employed through the well-established commercial software CST Microwave Studio. The simulations were performed by considering one unit cell of the system embedded in a waveguide with electric and magnetic boundaries to support a constant profile TEM wave. Waveguide ports were used as source and detector to monitor the transmission and reflection properties of this system. In the simulations, the substrate dielectric coefficient (for the non-photo-excited substrate) was taken as 12.7, and the copper conductivity  $5.8 \times 10^7$  S/m. First, we only consider the effect of a conductivity change. In this condition, only a red shift of the resonant frequency was observed. The blue-shift of the resonance frequency would most probably be due to photo excitation-induced dynamic response of the GaAs substrate beneath the SRRs as the observation from Figure 68(b) suggested it. To fit the experimental results, we used the well-known Drude model, capable of

describing the dynamic behavior of GaAs accurately within our considered frequency regime [21, 22]. We first assume the photo-excited layer with a thickness (i.e., penetration depth),  $d$ , of a typical value, 1  $\mu\text{m}$ . The frequency-dependent complex conductivity takes the form,  $\sigma = \epsilon_0 \omega_p^2 / (\gamma - i\omega)$ , where  $\epsilon_0$  is the permittivity of vacuum,  $\gamma$  represents the collision frequency and  $\omega_p$  the plasma frequency is determined by  $\omega_p = \sqrt{Ne^2 / (\epsilon_0 m^*)}$ .



**Figure 70: (a) Simulation results of the transmission amplitude spectra and (b) phase modulation for different levels of carrier density  $N$ .**

$N$  is the carrier density,  $e$  is the free electron charge ( $1.6 \times 10^{-19}$  C), and  $m^* = 0.067m_0$  ( $m_0$  is the mass of the free electron), the effective carrier mass in n-doped GaAs. The dielectric constant  $\epsilon(\omega)$  is obtained, based on  $\sigma(\omega)$  by  $\epsilon(\omega) = \epsilon_s + i\sigma / (\epsilon_0 \omega)$ , where  $\epsilon_s$  is the dielectric constant of un-doped GaAs. To fit the resonance frequency at 1.4 THz for the case of a non-illuminated sample, we used  $\epsilon_s = 12.7$ , and we kept this value throughout our fitting procedure for all cases. Next, we focused on the photo-doping cases. According to the Drude model, it is easily found that the carrier density,  $N$ , and collision frequency,  $\gamma$ , are pending quantities, which together determine the properties of the photo-excited layer and the response of the sample. In our fitting procedure,  $\gamma$  should be kept constant for any set of  $N$  because the mobility of the carriers changes slightly within the explored carrier density range. The collision frequency,  $\gamma$ , was taken as 1.8 THz. By fitting the resonance frequencies and the corresponding transmission amplitudes, and simultaneously considering the transmission levels at a low frequency band, the retrieved values of the carrier density  $N$  are  $3 \times 10^{16} \text{ cm}^{-3}$ ,  $1.5 \times 10^{16} \text{ cm}^{-3}$ , and  $5 \times 10^{15} \text{ cm}^{-3}$  for the excitation at  $6 \mu\text{J}/\text{cm}^2$ ,  $3 \mu\text{J}/\text{cm}^2$ , and  $1 \mu\text{J}/\text{cm}^2$ , respectively. The simulated results of the transmission spectra fit well the experimental ones, as shown in Figure 70(a). In the simulations, we also extracted the phase information of the transmission for the different cases. These results are presented in Figure 70(b). Similar to the experimental results, we also can observe the interesting phase modulation effect almost as impressive as in the experiments.

To conclude, in this section we have shown the existence of a frequency shift under injection of photo-carriers related to the change of the refractive index of the GaAs substrate. Also, an important phase tunability (over  $\sim\pi/4$ ) for a large frequency bandwidth ( $\sim 250$  GHz) was observed, which demonstrates the possibility of phase modulation under photoexcitation, consequently, opening the way to the realization of simple broadband phase plate devices in the THz range.

## V.3/ Mode shifting

An attractive progress for THz metamaterials is the proposal of frequency-agile metamaterials, i.e., frequency-tunable notch filters [10]. A clever and quite straightforward, idea is to incorporate photoconductive semiconductors, as elements of metamaterial resonators, so the working frequency of the metamaterial resonator can be tuned through photo-excited carrier injections. A red-shift tunability has already been achieved, due to a photoconductive increase in capacitance of the resonator [10]. For greater flexibility in practical applications, blue-shift tunability should be also of great importance. As we have shown in the previous section, a change in the substrate refractive index can allow a relatively small blue-shift in frequency ( $\sim 50$  GHz). Two theoretical designs have been proposed in order to achieve a bigger shift. Nevertheless their potential seem to be limited by the excessive amount of photo-excitation needed to generate enough current to traverse the silicon regions and reduce the effective loop size [10]. The high level of optical pumping needed may simply results in the damage of the metamaterial sample.

### V.3.1 eSRR design and fabrication

Therefore, another design for blue-shift tunability based on the new mechanism of photoconductive mode switching effect has been proposed [11]. This mechanism is derived from electric-field coupled inductor-capacitor (ELC) resonator [23] and an evolved version of the E1 structure presented in [24]. Photoconductive silicon islands are integrated within two side gaps as depicted in Figure 71(a). With such a design, under high intensity pump the two side loops are short-circuited which contributes to a decrease of the total effective inductance leading to a higher resonance frequency. Hence an all-optical blue-shift switching effect is achieved which can ideally be tuned up to 39 % as simulations have shown [11]. The metamaterial under study has been fabricated on commercially available silicon-on-sapphire (SOS) wafers, consisting of a  $0.6 \mu\text{m}$ -thick (100) Si epitaxial layer on top of a  $530 \mu\text{m}$ -thick R-plane sapphire substrate. The intrinsic resistivity of the Si epilayer was not measured, but was specified as  $>100 \Omega \text{ cm}$  by the manufacturer. The first step of the fabrication process was the definition of the photosensitive area. This was accomplished by photolithographically protecting the two  $6 \times 6 \mu\text{m}^2$  regions that coincide with the two side gaps of the metallic resonator, and subsequent reactive ion etching (RIE) of the Si epilayer outside the two side gap regions. Next, the photo resist pattern was removed, and a second RIE step was performed on the entire unprotected sample surface to decrease the thickness of the patterned Si layer from  $0.6$  to  $0.2 \mu\text{m}$ . This resulted in two  $6 \times 6 \times 0.2 \mu\text{m}$  mesa-shaped Si photosensitive regions per unit cell. The metallic resonator pattern aligned to the Si photosensitive mesa was defined by photolithography,  $150 \text{ \AA}$  titanium and  $2350 \text{ \AA}$  gold were deposited by E-beam evaporation.

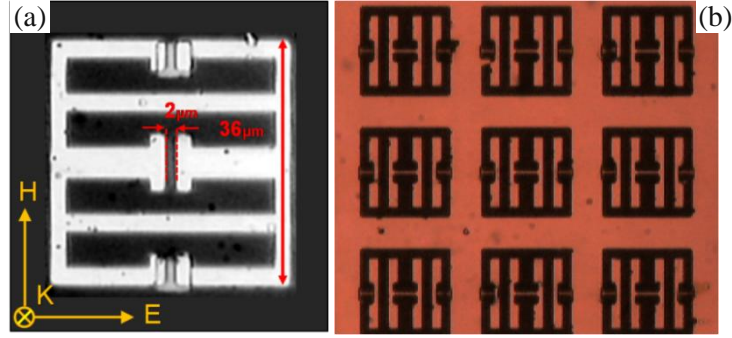


**Figure 71: (a) Microscope picture of one unit cell ERC and its dimensions. (b) Microscope picture of an array of 9 ERCs.**

Finally, this is followed by removal of unwanted metal. The fabricated sample is shown in Figure 71(a) and part of the array in Figure 71(b).

### V.3.2 Experimental results

The experimental study of the sample was performed using our time domain spectrometer (see Figure 67). To study the dynamic response of the metamaterial, an optical-pump beam was used to excite photo-carriers in the silicon. The sample was placed orthogonally on the THz beam path and at the focus of the THz beam, while 45° to the optical pump beam. At this point, the THz beam spot's diameter measured about 1 mm. The temporal synchronization of the THz and the optical pump beams has been experimentally defined. Afterwards, the THz pulse was delayed to assure a 5 ps average (because of the angle between the two beams) delay between them. This 5 ps delay was used to assure a quasi-steady state of the injected photo-carriers, since they have a lifetime in the nanoseconds regime. In addition, to ensure a uniform photo-excitation and the focused optical beam pumps the exact same region of the sample probed by the THz beam, the pump beam was expanded to a diameter of ~3 mm. A metallic aperture of 1.2 mm diameter placed immediately in front of the sample. Any residual pump laser radiation, which would bring noise in the detection of the THz electric field, was filtered out by placing a Si wafer (375 μm thick) just after the sample. The linearly polarized THz electric field is normally incident onto the metamaterial sample or the sapphire reference substrate. The transmitted THz electric fields are then coherently recorded in the time domain (see Figure 72). The frequency-dependent amplitude  $t(\omega)$  of the transmitted THz pulse through the metamaterial is retrieved by the division of the sample spectrum with the reference spectrum  $t(\omega) = E_{\text{sample}}(\omega)/E_{\text{ref}}(\omega)$ .

The experimental results of the frequency-dependent response of the studied metamaterial are shown in Figure 73(a). Without applying the pump beam, the normalized transmitted THz electric field amplitude exhibits a minimum of  $t(\omega) = 10\%$  near the resonance at 0.76 THz (black dashed curve). As the pump energy flux increases, the resonance initially weakens. For cases with a flux value higher than 102 μJ/cm<sup>2</sup>, the resonance shows a significant shift to higher frequencies.

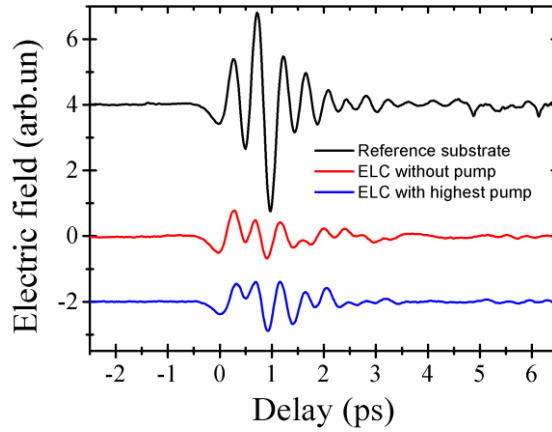


**Figure 72: Measured electric field for the reference substrate and for the sample without optical pump and at the highest level of optical pump.**

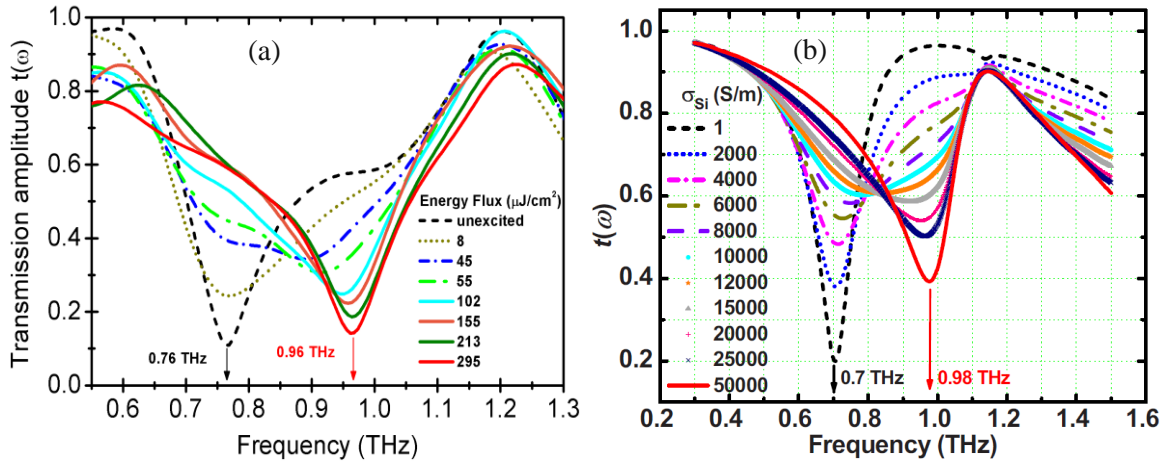


**Figure 73: (a) Normalized transmission amplitude spectra as a function of energy flux of pump beam. (b) Results of simulations as a function of silicon conductivity.**

At the level with energy flux  $295 \mu\text{J}/\text{cm}^2$ , the resonance dip in the transmission spectrum,  $t(\omega) = 15\%$ , is finally located at  $0.96 \text{ THz}$  (red line), which corresponds to a fairly broadband blue-shift of  $27\%$  in the resonance frequency.

### V.3.3 Simulations

As a comparison and to support our experimental demonstrations, we present in Figure 73b the results of numerical simulations performed by the commercial software CST Microwave Studio. A single unit cell was adopted for the simulations with appropriate boundaries resembling actual conditions in the THz TDS experiment. For the metallic parts (gold) of the metamaterial resonator, a lossy-metal model is utilized, the conductivity is  $\sigma_{\text{gold}} = 7 \times 10^6 \text{ S/m}$ . The sapphire substrate is taken

as lossless dielectric with  $\epsilon_{\text{Sapphire}} = 10.5$ . For the photo-active silicon parts, we applied a simple conductivity model,  $\epsilon_{\text{Si}} = 11.7$ , and the conductivity,  $\sigma_{\text{Si}}$ , is a pending value chosen to correspond to different pump levels. For the case without illumination,  $\sigma_{\text{Si}}$  was taken to be 1 S/m, the simulated resonance occurs around 0.69 THz and the transmission at resonance is around 20%.

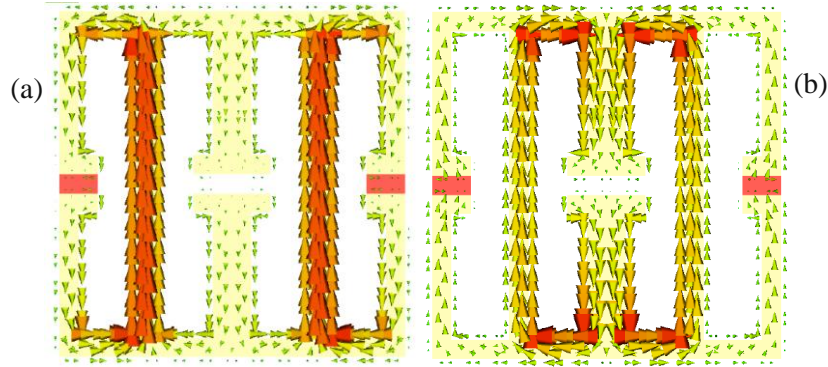


**Figure 74: Distribution of surface current density at resonance frequency. (a), Surface current at  $f = 0.7$  THz for  $\sigma_{\text{Si}} = 1$  S/m (no pump case). (b) Surface current at  $f = 0.96$  THz for  $\sigma_{\text{Si}} = 50000$  S/m (case with highest pump intensity).**

Following the increasing pump fluxes, we selected different corresponding values of  $\sigma_{\text{Si}}$  to reproduce the experimental results. The final conductivity of Si was taken as high as  $1 \times 10^5$  S/m only for obtaining similar transmission behavior relative to the no pump case, but it is noticed that actually around  $\sigma_{\text{Si}} = 3 \times 10^4$  S/m, the resonance has been shifted close to the final frequency 0.96 THz. Therefore, the simulations showed an all-optical blue-shift with the tuning range of 39%, which is in good agreement with the experimental demonstration. The deviation between the simulations and experiments may be due to imperfections in the sample preparation, which cannot be taken into account within the simulations. For further intuitive understanding of this mechanism, we show in Figure 74 the distributions of surface current density at two corresponding resonance frequencies for cases of no pump and highest pump, respectively.

In conclusion, in this section, we have experimentally demonstrated all-optical broadband blue-shift tunability with a meticulously-designed metamaterial in the terahertz regime. The goal was essentially achieved by our proposed photo-excited mode switching effect, which offers a new path to exploring more designs targeting greater flexibility for practical applications in the range of frequency-agile metamaterials. The work also paves the way for future bi-directional and multi-band even cascade switchable devices as suggested from theoretical studies [11].

## V.4/ Chapter conclusions

In this chapter, we have shown the possibility to obtain a frequency shift and a broadband tunability from a classic metamaterial design such as Split Ring Resonator. Numerical calculations, using a simple Drude model, can explain both of these effects, as a result of the changes induced on the complex index of refraction of the photo-excited semiconductor substrate. Furthermore, we have shown that much bigger tunability can be obtained using a careful design of the metal structure. Both experimental demonstrations have been done dynamically using a synchronized laser beam for the injection of photo-carriers.

## References

1. D. R. Smith, J. B. Pendry, and M. C. K. Wiltshire, "Metamaterials and Negative Refractive Index," *Science* **305**, 788-792 (2004).
2. V. G. Veselago, "The electrodynamics of substances with simultaneously negative values of  $\epsilon$  and  $\mu$ ," *Soviet Physics Uspekhi* **10**, 509 (1968).
3. J. B. Pendry, A. J. Holden, D. J. Robbins, and W. J. Stewart, "Magnetism from conductors and enhanced nonlinear phenomena," *IEEE Trans. Microw. Theory Tech.* **47**, 2075-2084 (1999).
4. D. R. Smith, W. J. Padilla, D. C. Vier, S. C. Nemat-Nasser, and S. Schultz, "Composite medium with simultaneously negative permeability and permittivity," *Phys. Rev. Lett.* **84**, 4184-4187 (2000).
5. J. B. Pendry, "Negative Refraction Makes a Perfect Lens," *Phys. Rev. Lett.* **85**, 3966 (2000).
6. C. M. Soukoulis, S. Linden, and M. Wegener, "PHYSICS: Negative Refractive Index at Optical Wavelengths," *Science* **315**, 47-49 (2007).
7. R. A. Shelby, D. R. Smith, and S. Schultz, "Experimental Verification of a Negative Index of Refraction," *Science* **292**, 77-79 (2001).
8. N. Fang, H. Lee, C. Sun, and X. Zhang, "Sub-Diffraction-Limited Optical Imaging with a Silver Superlens," *Science* **308**, 534-537 (2005).
9. D. Schurig, J. J. Mock, B. J. Justice, S. A. Cummer, J. B. Pendry, A. F. Starr, and D. R. Smith, "Metamaterial Electromagnetic Cloak at Microwave Frequencies," *Science* **314**, 977-980 (2006).
10. H. T. Chen, J. F. O'Hara, A. K. Azad, A. J. Taylor, R. D. Averitt, D. B. Shrekenhamer, and W. J. Padilla, "Experimental demonstration of frequency-agile terahertz metamaterials," *Nature Photonics* **2**, 295-298 (2008).
11. N.-H. Shen, M. Kafesaki, T. Koschny, L. Zhang, E. N. Economou, and C. M. Soukoulis, "Broadband blueshift tunable metamaterials and dual-band switches," *Physical Review B (Condensed Matter and Materials Physics)* **79**, 161102-161104 (2009).
12. W. J. Padilla, A. J. Taylor, C. Highstrete, M. Lee, and R. D. Averitt, "Dynamical Electric and Magnetic Metamaterial Response at Terahertz Frequencies," *Phys. Rev. Lett.* **96**, 107401-107404 (2006).
13. H.-T. Chen, W. J. Padilla, J. M. O. Zide, S. R. Bank, A. C. Gossard, A. J. Taylor, and R. D. Averitt, "Ultrafast optical switching of terahertz metamaterials fabricated on ErAs/GaAs nanoisland superlattices," *Opt. Lett.* **32**, 1620-1622 (2007).
14. N. I. Landy, S. Sajuyigbe, J. J. Mock, D. R. Smith, and W. J. Padilla, "Perfect Metamaterial Absorber," *Phys. Rev. Lett.* **100**, 207402 (2008).
15. H.-T. Chen, W. J. Padilla, M. J. Cich, A. K. Azad, R. D. Averitt, and A. J. Taylor, "A metamaterial solid-state terahertz phase modulator," *Nat Photon* **3**, 148-151 (2009).
16. X. G. Peralta, E. I. Smirnova, A. K. Azad, H.-T. Chen, A. J. Taylor, I. Brener, and J. F. O'Hara, "Metamaterials for THz polarimetric devices," *Opt. Express* **17**, 773-783 (2009).
17. J. B. Pendry, A. J. Holden, W. J. Stewart, and I. Youngs, "Extremely low frequency plasmons in metallic mesostructures," *Phys. Rev. Lett.* **76**, 4773-4776 (1996).
18. J. B. Pendry, A. J. Holden, D. J. Robbins, and W. J. Stewart, "Low frequency plasmons in thin-wire structures," *J. Phys.-Condes. Matter* **10**, 4785-4809 (1998).

19. J. M. Manceau, N. H. Shen, M. Kafesaki, C. M. Soukoulis, and S. Tzortzakis, "Dynamic response of metamaterials in the terahertz regime: Blueshift tunability and broadband phase modulation," *Applied Physics Letters* **96**, 021111-021113 (2010).
20. M. Schall and P. U. Jepsen, "Photoexcited GaAs surfaces studied by transient terahertz time-domain spectroscopy," *Opt. Lett.* **25**, 13-15 (2000).
21. N. Katzenellenbogen and D. Grischkowsky, "Electrical characterization to 4 THz of N- and P-type GaAs using THz time-domain spectroscopy," *Applied Physics Letters* **61**, 840-842 (1992).
22. M. C. Beard, G. M. Turner, and C. A. Schmuttenmaer, "Transient photoconductivity in GaAs as measured by time-resolved terahertz spectroscopy," *Physical Review B* **62**, 15764-15777 (2000).
23. D. Schurig, J. J. Mock, and D. R. Smith, "Electric-field-coupled resonators for negative permittivity metamaterials," *Applied Physics Letters* **88**, 041109-041103 (2006).
24. W. J. Padilla, M. T. Aronsson, C. Highstrete, M. Lee, A. J. Taylor, and R. D. Averitt, "Electrically resonant terahertz metamaterials: Theoretical and experimental investigations," *Physical Review B (Condensed Matter and Materials Physics)* **75**, 041102-041104 (2007).

*Chapter VI: Applications of an intense THz  
source for THz nonlinear optics*

**CHAPTER VI: APPLICATIONS OF AN INTENSE THZ SOURCE FOR THZ NONLINEAR OPTICS ..... 124**

**VI.1/ Introduction..... 126**

**VI.2/ Excitation of phonons in semiconductors..... 127**

VI.2.1 Traditional approach for phonon excitation ..... 127

VI.2.2 Coherent phonon excitation with THz radiation..... 129

    a) Experimental approach and sample characterization..... 129

    b) Coherent phonon ..... 130

    c) THz coupling to the semiconductor lattice..... 131

VI.2.2 Lattice deformation and incoherent phonon excitation ..... 132

    a) Lattice deformation ..... 132

    b) Incoherent phonon..... 134

**VI.3/ Nonlinearities in electro-optic crystal ..... 136**

VI.3.1 Phonons generation ..... 136

VI.3.2 THz pulse self-phase modulation ..... 137

VI.3.3 Electro-optic distortions ..... 139

**VI.4/ Scaling up the THz pulse energy ..... 140**

**VI.5/ Chapter conclusions ..... 143**

    References ..... 144

## VI.1/ Introduction

Due to the lack of powerful sources, for many years the application of THz radiation stayed limited to probing experiments, or more generally to spectroscopic applications. Historically, micro joule energy range could only be reached using huge installations such as free electron lasers. In the last five years, few experimental approaches have proven to reach this level of energies while using table-top lasers [1-3]. The two-color filamentation source is an excellent candidate in order to routinely produce THz pulses in the micro-joule range as many reports attested it [4, 5]. Such level of energy confined in an ultrashort pulse of a sub millimeter focused size allows reaching unprecedented electric fields approaching the MV/cm level. This source has already been successfully used in nonlinear THz experiments [6, 7]. Furthermore, recent reports have demonstrated the possibility to observe nonlinearities in electro-optic crystals or liquids [8-10].

In this chapter we will present our time-resolved pump-probe experiments where we employed intense, single cycle THz pulses to directly excite (pump) phonons into semiconductors. There, we followed the lattice dynamics by monitoring the transient transmission changes of an optical pulse (probe) tuned to the valence-to-conduction-band transition. Following this first section, we will present evidence of THz pulse self-phase modulation in a non-centrosymmetric crystal. Furthermore, using a thinner crystal, we have been able to observe distortions in the recorded electro-optic signal. Finally, we will report on our recent attempt to scale-up the energy of our THz source and reach the level of micro-joule per THz pulse.

## VI.2/ Excitation of phonons in semiconductors

Intense THz pulses interaction with matter has already been the subject of intense studies. For example it has already been shown to resonantly couple with electronic states in nanostructures revealing for instance the dynamics of excitonic polarization [11] or directly coupling into ferroelectrics revealing their lattice vibrational anharmonicity [12]. At higher level of THz electric field, the large ponderomotive forces associated with the THz pulses have been shown to shift the band edge of semiconductors or quantum well resonances [13, 14]. Finally, a last class of experiments with an emphasis on doped semiconductors has demonstrated the possibility to accelerate free carriers via the THz electric field leading to impact ionization processes [6, 7, 15, 16].

Another interesting potential application of intense THz pulses would be the direct and resonant excitation of the vibrational modes of a physical system. This is of main importance in order to understand and control physiochemical as well as biological processes [17-19]. For many systems such modes have eigen frequencies in the THz regime. Direct and selective coherent excitation of lattice modes with far-infrared radiation e.g. THz frequencies and probing with temporal resolution could allow to prepare and study a system in a state where energy is not statistically distributed among its degrees of freedom (e.g. as the result of the incoherent electron-phonon interaction) but may well be preferentially channeled towards a desirable pathway triggered by few - or ideally one – eigenmodes, e.g. chemical selectivity of a surface reaction controlled by selective excitation of vibrational modes at the substrate. The clear advantage here would be to employ a single, direct and resonant photon-phonon transition which is by definition a much more probable process. This, with the proper introduction of temporal resolution will allow the study of the dynamics in the excitation and the decay of the lattice alone.

### VI.2.1 Traditional approach for phonon excitation

Traditionally, phonon excitation has been realized either as a side effect of an initial electronic excitation through interaction with optical radiation or via Raman mechanisms. In the first case electron density effects hinder direct measurements of the phonon decay. This approach is known as Displacive Excitation of Coherent Phonons (DECP) [20-25] and refers to the excitation and study of the lattice in an excited electronic potential where the phonons are studied under the influence of the excited electrons, which is unwanted. Such optical-pump/optical-probe experiments have been frequently employed to study ultrafast coherent phenomena in solids, including bulk semiconductors and their superlattices [21]. Following initial optical interband excitation electron-hole pairs are created. Relaxation follows with a variety of physical mechanisms [26] including electron-electron and electron-phonon scattering.

Incoherent phonons on one hand are excited and manifested as lattice vibrations with random energies and momenta. They are macroscopically evidenced as a temperature increase. Coherent lattice excitation on the other hand is the population of a certain eigenmode of the lattice vibration. In the case of semiconductors (including GaAs-based compounds) coherent phonon excitation of the optical and acoustical branch [20-24, 27, 28] occurs by the initially excited electrons. In the case of the optical phonon excitation this is frequently attributed to ultrafast screening variations due to ultrafast scattering and trapping of the generated carriers resulting in large carrier density gradients and surface space-charge fields [29] while in the case of acoustic phonons they are attributed to the induced inhomogeneity in the excitation (photo-elasticity) and the resulting lattice strain effects. In the case that the photon energy is not enough to be directly absorbed, e.g. energy below the band gap of the semiconductor, two photons within the Fourier components of the broadband pulse may couple with the nonlinear susceptibility of the material resulting in coherent phonon excitation [22] provided that energy and momentum are conserved during the interaction processes. With the first resonant excitation scheme, electrons and holes are unavoidably excited thus restricting the study of the excitation and decay of the coherent phonons alone. With the second non-resonant case, the efficiency of the process is restricted due to the nonlinear character of the interaction of light with matter. Unavoidably, when increasing the light intensity in order to increase the efficiency of the process undesirable electron-hole generation via nonlinear absorption may occur.

In the second approach, incoherent and stimulated time-resolved Raman scattering probes the energy relaxation and the dephasing of the excited phonons respectively [30, 31]. The narrow band width of the required laser source restricts the temporal resolution of the experiments and therefore probing the lattice excitations in a phase sensitive manner is not possible. When an energetically large quasi-particle (e.g. electron-hole pair excitation) is created like in the first paragraph, the subsequent incoherent electron-phonon interaction creates phonons with characteristics (i.e. energy, momentum, symmetry, etc.) that cannot be externally controlled. This can be partially accomplished when employing an Impulsive Stimulated Raman Scattering (ISRS) scheme [20-24]. In this case however, the lattice excitation is achieved by combination of either two narrowband laser sources leading to loss of high temporal resolution or by nonlinear scattering/mixing of two photons of the same broadband pulse. In order to increase the efficiency of this process, the required high laser intensities may very well induce additional nonlinear phenomena as well, like multi-photon electronic excitations, which are undesirable. Furthermore, special and restrictive phase matching conditions may be involved.

## VI.2.2 Coherent phonon excitation with THz radiation

### a) Experimental approach and sample characterization

For this experiment, we have used our time domain spectrometer, already described in details. The THz radiation is collected and focused onto our semiconductor sample front surface which is orientated with a  $\sim 60^\circ$  angle with respect to the incoming THz beam. The variations in the interband transition probability are probed by monitoring with a linear photodiode the intensity of a 35 fs 800 nm probe, non-collinear to the THz pulse which marks a  $\sim 65^\circ$  angle with the sample. The angle between the THz pump and the optical probe was  $\sim 55$  degrees (see Figure 75). The semiconductor that has been used in this work is the intrinsic semiconductor  $\text{Al}_{0.08}\text{Ga}_{0.92}\text{As}$  (001) its dimensions are  $1 \mu\text{m}$  thick and  $\sim 1 \times 1 \text{ cm}^2$  wide and has been grown by molecular beam epitaxy at  $600 \text{ }^\circ\text{C}$ . The sample is chemo-mechanically treated to achieve the final thickness and deposited onto glass slides. Optical characterization determined the band gap at  $1.5 \text{ eV}$  ( $810 \text{ nm}$ ). The 8% Al mole fraction is assumed to have as a sole effect the increase of the band gap energy ( $E_g = 1.5 \text{ eV}$  for AlGaAs,  $E_g = 1.42 \text{ eV}$  for GaAs) leaving other band structure features essentially unchanged. Structural (Transmission Electron Microscopy) and electrical characterization of the grown samples shows the absence of defects in the form of mid-gap states and trapping centres. We have chosen to work with an intrinsic semiconductor as to avoid initial free carrier excitation. Furthermore, its large band-gap prohibits electronic excitations using THz pulses, preventing us from inducing DECP phenomenon. We started our study by leading an optical pump and probe experiment with the samples at our disposition. An example of all optical excitation and probing is presented on Figure 76(a). It reveals the rich dynamics in AlGaAs that contain valuable information about the electron thermalization and transport effects. Figure 76(b) clearly demonstrates the possibility to differentiate the nature of the samples using this approach. The low-temperature grown GaAs shows a much faster recombination time, due to the imperfections induced during the annealing of the sample. Many semiconductors in general have been extensively studied using this technique.

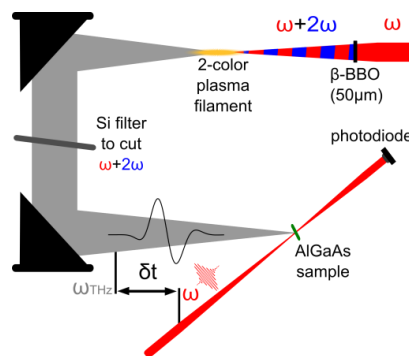


**Figure 75: Schematic of the experimental approach.**

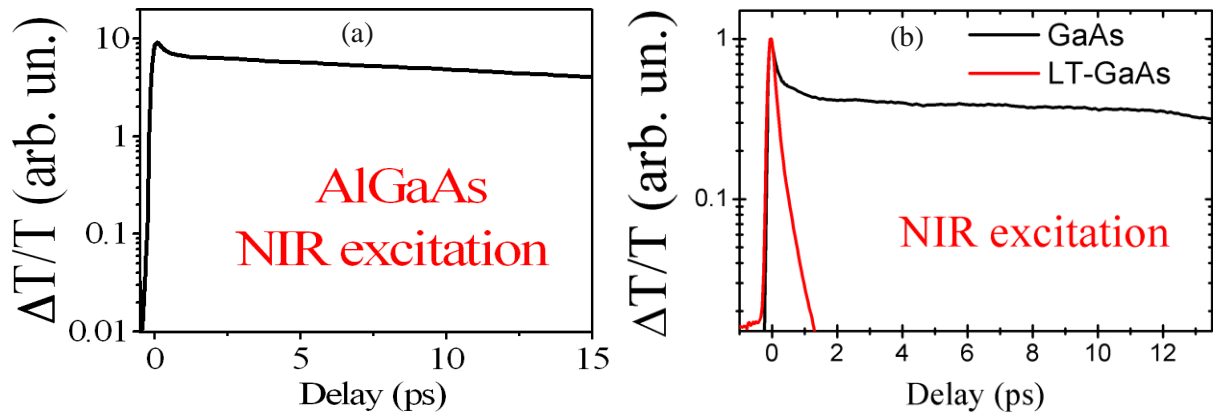


**Figure 76: Optical pump/optical probe analysis of three different samples. (a) AlGaAs, (b) GaAs and LT-GaAs.**

b) Coherent phonon

The picture changes radically from the all-optical case once we use the THz beam as source of excitation. The effect of the THz excitation is probed in time using a low intensity beam of our laser at 800nm and the results are shown in Figure 77(a). This constitutes a unique response and represents the direct, resonant (linear) coupling of the incident THz pulse with the lattice of AlGaAs and the subsequent probing with the 1.55 eV optical pulses of the decay dynamics. The strong-amplitude oscillation is embedded on an exponential-like decay with a characteristic decay time of 0.3 ps. We simulated the THz signature of the system with an antisymmetric function that we subtracted to the recorded signal and a subsequent analysis gives the results plotted in Figure 77(b). There we have isolated the coherent response of the AlGaAs crystal. It is evident that the response consists of a cosine-like oscillation convoluted with an exponential decay of the amplitude of the oscillation. The decay time of the amplitude of the oscillation is 0.5 ps and is attributed to the dephasing of the excited phonon which occurs via anharmonic decay due to the large availability (continuum) of acoustic phonon states with lower energy. The frequency of the oscillation is  $f = 2$  THz and the phase is  $\varphi = \pi/2$  indicating a displacive nature of the phonon excitation [21]. One of the fundamental differences between ISRS and DECP is that in the first case the impulse starts and ends with the incident laser pulse whereas in the second case the system after the impulsive excitation of the laser finds itself in an excited electronic eigenstate where even after the end of the impulsive laser excitation the equilibrium position of the lattice ions will remain shifted due to the re-arrangement of the electronic potential. In that case the excitation takes the form of a sudden step-like function. In our case, the excitation is different from both of the above. Firstly, we do not have a step-like excitation due to a suddenly shifted electronic potential and therefore the lattice oscillates around the original equilibrium position.

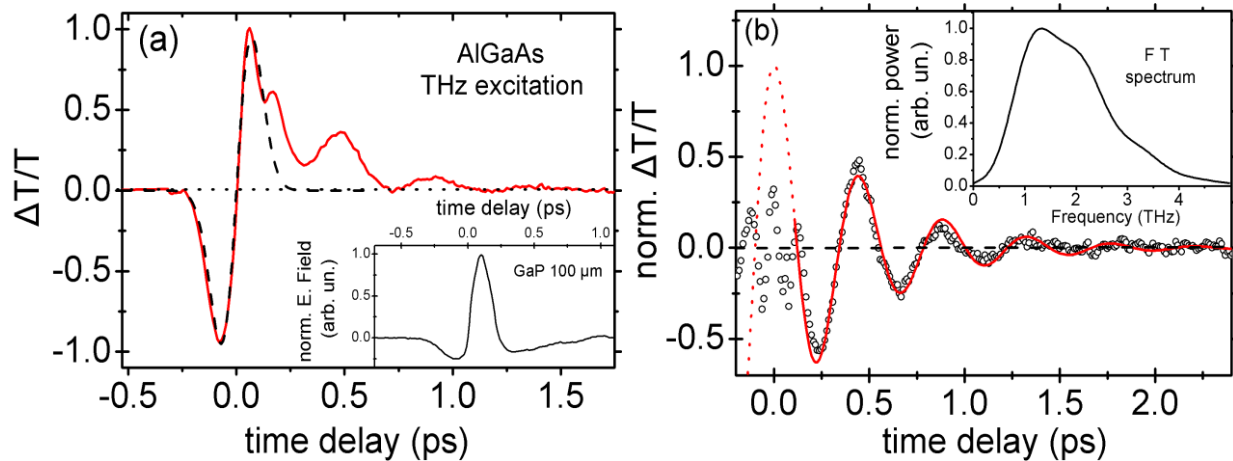


**Figure 77: (a) Dynamics following THz ultrafast excitation of AlGaAs with optical probing tuned to the valence-to-conduction band transition. (b) Dynamics following THz ultrafast excitation of AlGaAs with optical probing tuned to the valence-to-conduction band transition**

Nevertheless, the amplitude of the oscillation exhibits a  $\cos(\omega t)$  behavior which is characteristic of the DECP mechanism that we have excluded in our case. This discrepancy in the relaxation dynamics constitutes a novel behavior that certainly needs theoretical investigation to help understand in depth the underlying physics.

### c) THz coupling to the semiconductor lattice

A point to address here is how the THz radiation couples to the semiconductor. The Franz-Keldysh effect (FKE) (electro-absorption) has been shown to couple mid infra-red radiation with a semiconductor lattice [32]. In a similar approach to [32], we have examined the induced optical change around the band edge of the AlGaAs at different time delays of the THz-induced signal. As shown in Figure 78, we have observed an induced transparency above the band edge along with a strong induced absorption below the band edge that shows the driving force of the FKE for as long as the THz pulse illuminates the sample (in good agreement with [32]) whereas when the THz pulse has ended (e.g. at  $t=0.25$  ps) there is practically no FKE-induced effect. On the other hand, for longer time delays the signal remains non-zero and intensely oscillatory. Therefore, energy transfer from the laser to the lattice has to be considered.

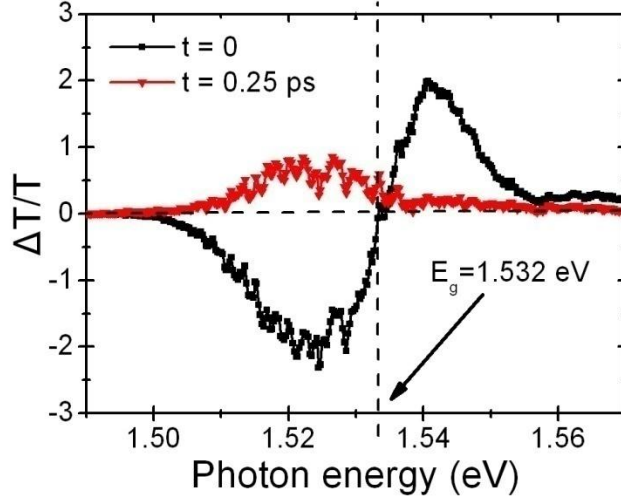


**Figure 78: Absorption of the probe beam at the AlGaAs band edge.**

An estimation of the Keldysh parameter can be deduced from the following equations [14]:

$$E_{KE} = \frac{e^2 E_{THz}^2}{4m^* \omega_{THz}^2},$$

$$\gamma = \frac{E_{KE}}{\hbar \omega_{THz}} = \frac{e^2 E_{THz}^2}{4m^* \hbar \omega_{THz}^3}.$$

Where  $E_{KE}$  is the mean kinetic energy of a particle of mass  $m^*$  and charge  $e$  in an electric field  $\vec{E}_{THz} \cos(\omega_{THz}t)$ , i.e., the ponderomotive energy. The dc FKE corresponds to  $\gamma \gg 1$ ; multiphoton effects occur for  $\gamma \ll 1$  and the case of  $\gamma \sim 1$  is the distinct Dynamical FKE regime. According to our electric field estimation with GaP crystal ( $202 \text{ kV.cm}^{-1}$ ) and the central frequency of our pulse (2 THz), we estimated  $\gamma$  to be equal to 216. This calculation further confirms the fact that we should observe an electro-absorption at the semiconductor band-edge while applying such strong THz electric field.

## VI.2.2 Lattice deformation and incoherent phonon excitation

### a) Lattice deformation

Another point to address here is how the excitation of the lattice, induces the measured transmission changes in the optical probe. The detection of coherent phonons is enhanced when the probe is tuned to the interband due to the energy shifts caused by the deformation potential. The influence of the phonon generation on a system's band structure has been recently directly verified with time-resolved photoemission spectroscopy [33, 34]. Therefore, phonon generation may lead to relative motions in E-k space of the conduction band minimum with respect to the valence band maximum (Figure 79a). Thus, the varying resonance conditions for the 800 nm probe induce the variations in the transmitted intensity. We therefore assign the observed oscillatory response (Figure 77(b)) to the generation of coherent

acoustic phonons and to an accompanied periodic shift of the positions of the conduction and valence bands. The subsequent periodic change in the transition probability from the valence towards the conduction band is manifested with the oscillating transmission of the NIR pulses. The extracted frequency ( $f = 2$  THz) matches well the predominant absorption peak for the TA phonon branch [35]. We propose that in the case of AlGaAs we are very sensitive to horizontal (momentum) relative band motions. This is because the optical transitions are more probable at the vicinity of  $k = 0$  and the probability reduces for both sides of the  $k$ -axis (Figure 79(a)).

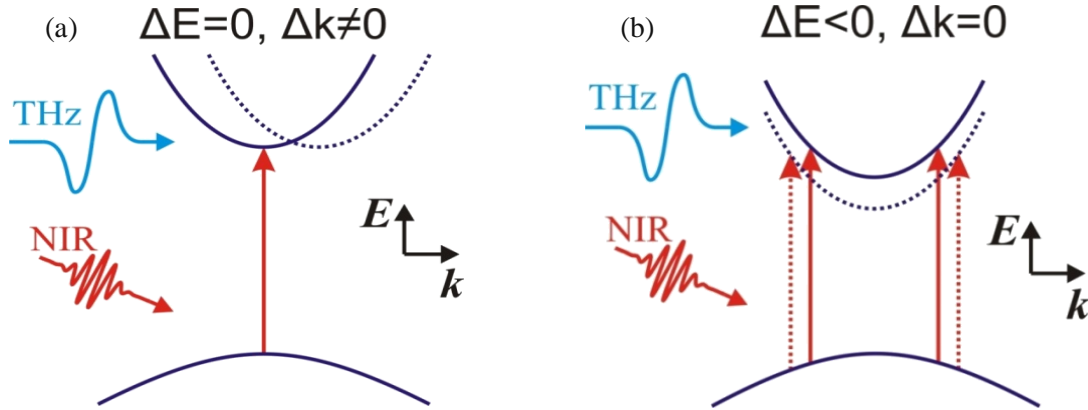


**Figure 79: (a) Simplified E-k band diagram for AlGaAs in the vicinity of  $k = 0$ . In AlGaAs lateral shift of the conduction band (dashed line) induced by the THz pulses, results in out-of-resonance conditions and therefore decrease in the absorption of the NIR pulse pulses by electrons initially residing in the valence band. (b) Simplified E-k band diagram for GaAs showing a downward shift of the valence band: absorption of NIR pulses increases.**

For  $t > 0$  the transient transmissivity remains positive at all time-delays corroborating the decreased overall absorption that the probe beam experiences due to the above mentioned out-of-resonance condition. This observation renders vertical (purely energetic) shifts of the conduction band rather improbable because this would occur in a direction in accordance to a temperature increase i.e. closer to the valence band [36]. This would lead to increased absorption (decreased overall transmission) which is contrary to our observations (Figure 77). Nevertheless, in order to fully relate this oscillatory behaviour to a deformation of the band structure, we decided to investigate the effect of the THz pulse excitation on intrinsic semiconductor for which the bandgap does not match the photon energy of the probe beam (e.g. GaAs). Hence, using a GaAs sample we would probe higher in the conduction band, which would directly prevent us from observing lateral displacement of the band in E-k space owing to the symmetry of the band (see Figure 79(b)).

### b) Incoherent phonon

In corroboration with our expectations, the signal observed once we shined the GaAs sample with the THz pulse did not show a coherent response but a simple incoherent response (see Figure 80). For vertical motions ( $\Delta E \neq 0$ ,  $\Delta k = 0$ ) of the conduction band, the net effect of the phonon excitation is the monotonous energetic shift of the conduction band. The probing with optical transitions is therefore more sensitive to this energetic shift which corresponds to the local increase in the temperature lattice that is known to result in a reduction of the band gap in semiconductors. Reduction of the band gap results in bringing the electrons with the probe in higher lying states in the conduction band where the absorption strength increases. Note here that the changes in the transmitted intensity of the 800 nm pulses depends solely on the transition probabilities from the valence towards the conduction band and not on electron population and bleaching effects that have been studied so far to study ultrafast dynamic effects in semiconductors.

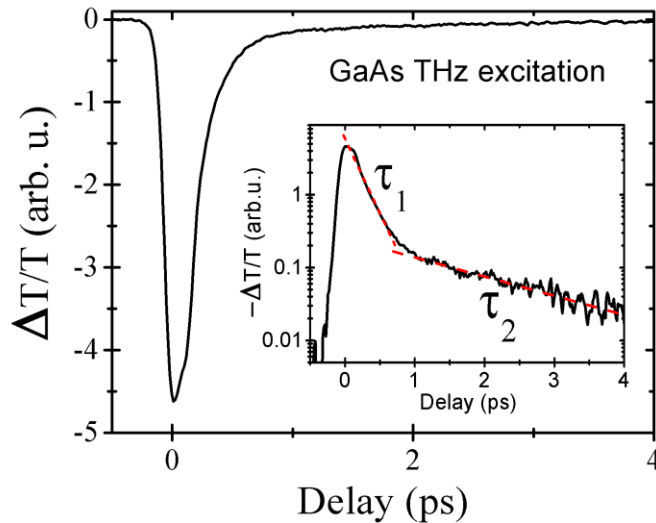


**Figure 80: Optically probed dynamics following ultrafast THz excitation of GaAs. Dashed lines correspond to exponential fittings with decay rates  $\tau_1$  and  $\tau_2$ .**

For  $t > 0$  the signal exhibits a bi-exponential decay. The first part is very fast with a characteristic decay time of 160 fs and the second one is much slower with a characteristic decay time of 1.4 ps. This observation points towards a non-uniformly excited phonon system and therefore to phonon modes that couple more strongly with the THz field. These internally redistribute energy and momentum reaching a local equilibrium within 160 fs. Subsequent phonon scattering with the rest of the phonon bath equilibrates the system with a time constant of 1.4 ps. This observation exhibits similarities with the phonon bottleneck effect recently observed with angle- and time-resolved photoemission spectroscopy of superconductors [33]. There, it was suggested that only a small percentage of the total lattice modes

contribute to the initial stage of the thermalization of electrons with the lattice. After this fast initial thermalization, the rest of the phonons start to contribute, however with a lower coupling strength that results in a reduction of the energy dissipation rate [33]. This mechanism is in analogy with the internal thermalization of electron following ultrafast optical excitation that undergo first a very fast internal thermalization and then at later times thermalize with the surrounding lattice. A second explanation for the observed bi-exponential decay may be the simultaneous excitation of TA and LA vibrational modes of the lattice. Both kinds of modes may well be excited by the THz radiation however we expect that lattice thermalization through LA phonon emission would be more efficient and therefore faster because of the higher slope in their dispersion curves and therefore the smaller number of phonons needed for redistribution of the excess energy and momentum acquired by the THz laser source.

In conclusion, in this section, we have shown the direct and resonant excitation of coherent and incoherent lattice modes in a semiconductor using intense, ultrashort THz pulses and the novel aspects of the relaxation dynamics that can be investigated with time delayed optical pulses. This is achieved by monitoring the transient variations in the absorption of optical wavelengths tuned in the vicinity of the valence-to-conduction band transition. This approach may allow the selective excitation and detection of coherent lattice modes from the rest of the thermal and incoherent phonon bath instead of the undesirable electronic contributions during DECP and restricting nonlinearities during ISRS. Projection of the results of this work may lead to utilization of intense THz pulses for the selective excitation of specific modes (e.g. vibrational) in a number of molecular systems. This would result in defining preferential pathways in chemical and biological reactions and thus gaining control over them.

## VI.3/ Nonlinearities in electro-optic crystal

### VI.3.1 Phonons generation

The effective nonlinear susceptibility  $\chi_{\text{eff}}^{(2)}$  of ZnTe in the THz domain has been shown to be strongly frequency dependent [37]. Thus, the highest detectable frequency with a ZnTe crystal is limited by its first Transverse-Optical (TO) phonon at 5.3 THz [38]. Later, a THz-TDS analysis of a ZnTe crystal has shown the influence of new phonon lines which strongly absorb THz radiation [39] at frequencies below 5.3 THz. In fact, the THz detected bandwidth was shown to be restricted by the new identified Transverse Acoustic (TA) phonon at 3.7 THz and Longitudinal Acoustic (LA) phonon at 1.6 THz, for a thick ZnTe crystal ( $>0.5$  mm) [39].

In the following, we present our own investigations using our time-domain spectrometer based on the detection with a 1mm ZnTe crystal. Figure 81(a) shows the temporal evolution of the THz electric field for two different levels of input pulse energy. Besides the difference in terms of electric field strength, one can observe the appearance of oscillations after 4 ps. Figure 81(b) presents a closer look at the recorded electric field after the main cycle. We presume that the following oscillations are related to the phonon modes within the ZnTe crystal. Consequently, by applying a Fourier Transform to the electric fields, we gained access to the relative spectra. In Figure 82 are presented the results. Firstly, the results show that it is possible to resolve frequencies up to 4.7 THz at low Electric field values. Secondly, discontinuities are observed around 2.7 THz. At higher THz electric fields, the picture radically changes. Figure 82 clearly shows the appearance of sharp phonon modes once the strength of the THz source is increased. The previously reported TA phonon at 3.7 THz and LA phonon at 1.6 THz are clearly resolved. Furthermore, one can see two new lines at 2.7 and 2.9 THz, which are the result of a direct LA-TA transition in the [110] ZnTe crystal [40].

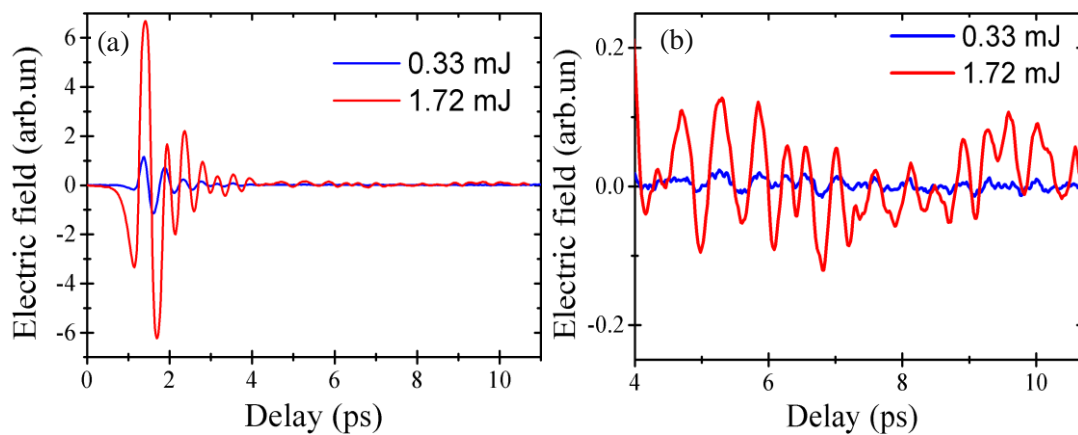


**Figure 81: (a) THz electric field as function of input pulse energy for 1mm ZnTe detection crystal. (b)**

**Zoom on Electric field trace after 4 ps delay.**

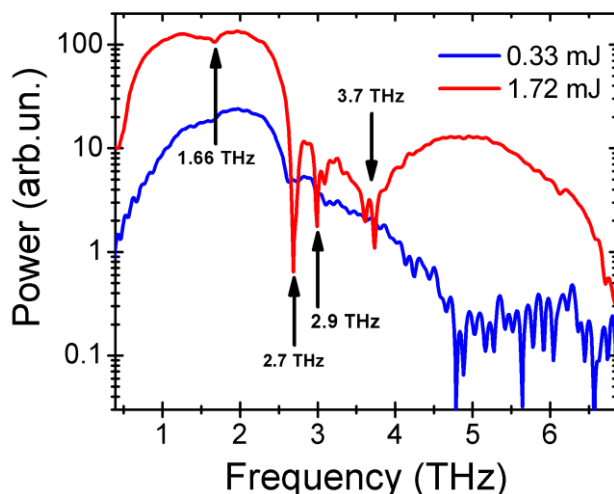


**Figure 82: Power spectrum and phonon identification**

Furthermore, we suggest that the possibility to observe much sharper phonon lines can be related to the strength of the applied THz field. It is not the result of a nonlinear phenomenon but rather the result of an increase of the signal to noise ratio. Thus, as the strength of the applied source is increased it becomes easier to resolve the variation of phonon modes induced by the THz radiation.

### VI.3.2 THz pulse self-phase modulation

The effect of self-phase modulation on the intense THz pulses propagating in nonlinear crystals can be attested in the normalized spectra shown in Figure 83(a). At high intensity, the THz spectrum shows a dip at the centre of the spectrum (2.7–4 THz) and an increase at each of the wings of the spectrum, compared to the low-intensity case. The effect is even clearer, once we plot the ratio of the spectra (see Figure 83(b)). This effect is typical of self-phase modulation (SPM). SPM is a nonlinear optical effect of light-matter interaction. An intense ultrashort pulse of light, when travelling in a medium, will induce a variation in the refractive index of the medium. This variation in refractive index is known to produce a phase shift in the pulse, leading to a change of the pulse's frequency spectrum.

The effect is so strong in this case that it can be observed directly in the time domain profiles. Figure 84 shows a zoom on the main cycle of the electric fields that were already presented in Figure 81(a). For clarity, the electric fields have been normalized. Careful analysis of the data shows that the delay between the first positive peak and the second negative peak is 70 fs larger at high intensity than at low intensity. This extra delay  $\tau$  is caused by the THz-intensity-dependent change in the THz index of refraction. Similar results have already been reported in other material at low temperature [7, 11].

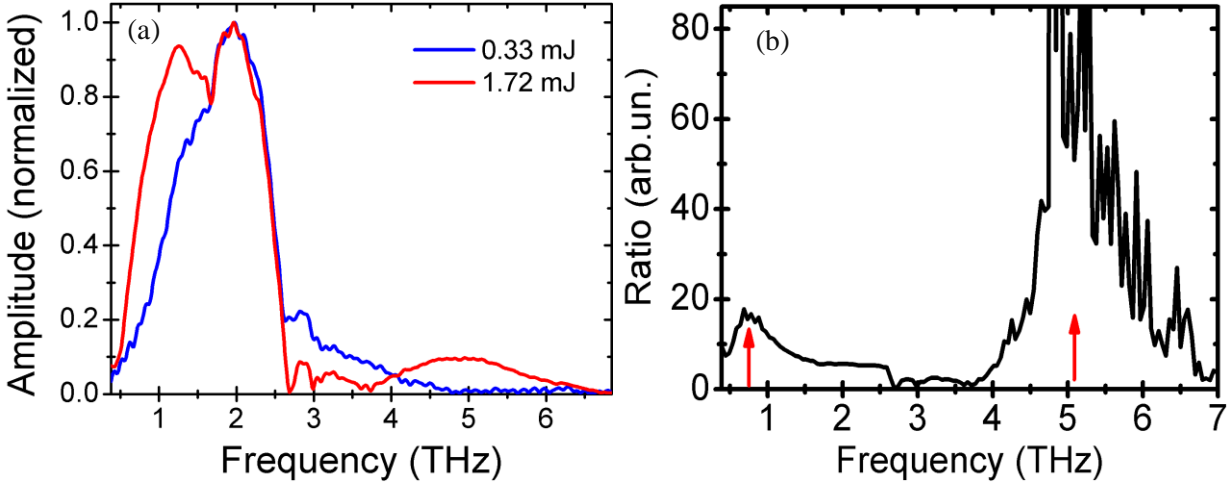


Figure 83: (a) Normalized spectra at high and low THz energy. (b) Ratio of the two spectra.

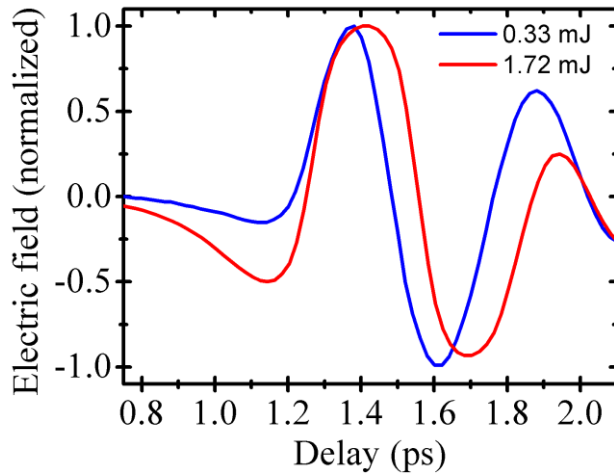


Figure 84: Zoom on the first cycle of the electric fields presented on Figure 81(a).

The fact that the SPM occurs in a non-centrosymmetric crystal could bring doubts about its origin. Indeed, cascaded second-order nonlinear effects have also been shown as an alternative for creating equivalent Kerr-like nonlinearities [41]. Nevertheless, such phenomenon is not instantaneous. Consequently, in our case, the SPM can be attributed to the optical Kerr effect, and it is possible to get an estimation of the refractive index change  $\Delta n$ , according to:

$$\Delta n = \frac{\tau c}{L} = n_2 I_{THz} .$$

Where  $\tau$  is the induced time delay, and  $I_{THz}$  is the intensity of the THz pulse. If we consider an interaction length of 1 mm within the ZnTe,  $\Delta n$  is equal to 0.021. At this level of laser input energy, the THz pulse energy was equal to 110 nJ. Using the time duration of the THz pulse measured with the GaP crystal (360 fs) as well as the  $1/e^2$  beam diameter, we obtained THz intensity of  $2.06 \times 10^8$  W/cm<sup>2</sup>. Thus, our estimation of the nonlinear refractive index,  $n_2$ , is equal to  $1.02 \times 10^{-10}$  cm<sup>2</sup>/W at THz frequencies. By

comparison, the  $n_2$  value reported for visible light in ZnTe is equal to  $1 \times 10^{-13} \text{ cm}^2/\text{W}$  [41]. Similar deviation with the value of  $n_2$  in LiNbO3 was observed at THz frequencies and attributed to the lattice anharmonicity [11].

### VI.3.3 Electro-optic distortions

As previously mentioned, the principle of electro-optic detection relies on the phase retardation induced to a probe beam by the THz field within an electro-optic detector. The measured signal  $S$  on the balanced photodiodes is proportional to  $\sin(\Delta\Gamma)$ , where  $\Delta\Gamma = \pi E_{\text{THz}}/E_\pi$  is the induced phase retardation.  $E_\pi$  represents the half-wave field of the crystal, which defines the minimum electric field which gives  $\pi$  phase delay with unit thickness. This suggests that there is the possibility to over-rotate the probe beam ( $\Delta\Gamma > \pi$ ) which should restrict the measurement of the THz electric field. At low THz electric fields ( $E_{\text{THz}} \ll E_\pi$ ), one can consider  $\sin(\Delta\Gamma) \sim \Delta\Gamma$  which makes the measured signal  $S$  proportional to the electric field. At higher electric levels, it has been shown recently that the measured signal  $S$  is not linear anymore [10]. Indeed at electric field level around half of  $E_\pi$  (45 kV/cm for ZnTe), the measured signal  $S$  significantly deviates from  $\Delta\Gamma$ , and reaches the point where the measured electric field is folding on itself.

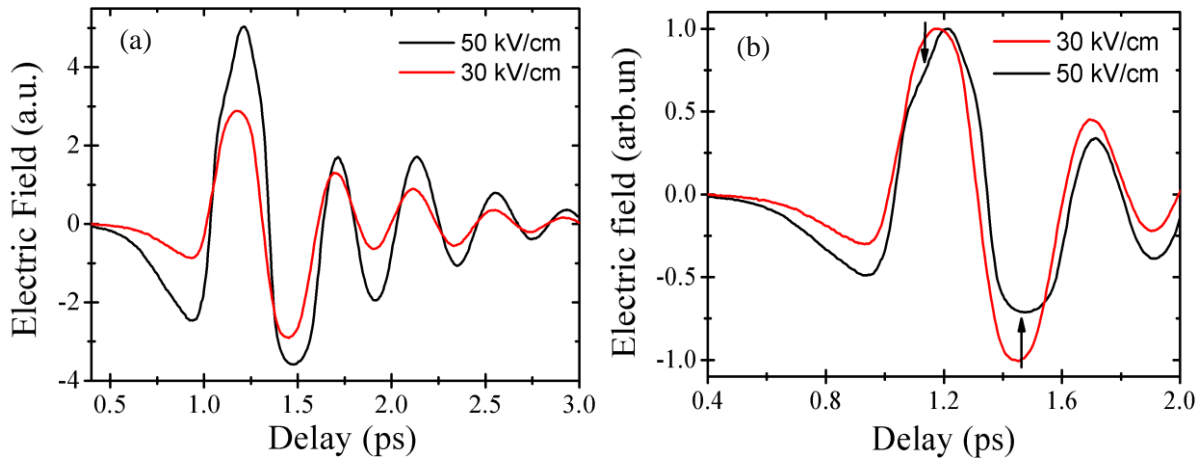


**Figure 85: (a) Measured THz electric field for two different laser input energies. (b) Zoom on the respective electric fields main cycle.**

As already calculated in chapter II, our estimation of the THz electric field emitted from 2-color filament with the kHz laser output was equal to 42 kV/cm. Our value, which is closed to the minimum one reported in [10] for nonlinear regime, let us presumed of the possibility to observe distortions with our time domain spectrometer. Consequently, we have led a careful optimization of our time domain spectrometer as well as our laser source. Hence, we have been able to reach an estimated level of electric field of 50 kV/cm. Furthermore, in order to reproduce the experimental condition of [10] and to minimize the effect of self-phase modulation, we have used a thinner ZnTe crystal (0.5 mm). Figure 85(a), shows

the recorded field for two values of laser input energy and their respective electric field estimation. At this level, we are able to observe the first distortions occurring on the signal. A close up on the main cycle of the THz electric fields is shown in Figure 85(b). There, it is obvious that above half of  $E_{\pi}$ , the THz electric field presents a peculiar shape. Furthermore, we normalized the electric fields which shows that the negative part of the main cycle of the electric field starts to fold (for the case of 50 kV/cm). Folding of the first positive peak is also observable, which is in good agreement with [10]. This value of 50 kV/cm has been obtained for maximum laser input pulse energy of 1.4 mJ (kHz repetition rate) and pulse duration of 35 fs. Furthermore, self-phase modulation is also observed, to a smaller scale since the comparison occurs between two high levels of THz intensity.

## VI.4/ Scaling up the THz pulse energy

One question that has not been addressed so far in the literature is the effect that the BBO crystal thickness has on the emission of THz from a 2-color filament. Figure 86 shows the electric fields and their Fourier transforms obtained for three different thicknesses of BBO crystals. For each crystal the maximum value of THz electric field was optimized at the detection crystal (ZnTe 1mm). The electric fields have been recorded in a normal atmosphere with 50% of relative humidity which explains the oscillatory features occurring after the main cycle. Figure 86(a) clearly demonstrates that the thinnest BBO crystal yields the strongest THz pulse. This can be attributed to a minimized temporal walk-off occurring between  $\omega$  and  $2\omega$ . Consequently, the optimization of the yielded THz power is more dependent on the temporal walk-off than the amount of yielded second harmonic field. Furthermore, it is important to note that there is no variation in the yielded spectra, in the limit of the resolved bandwidth (Figure 86(b)).

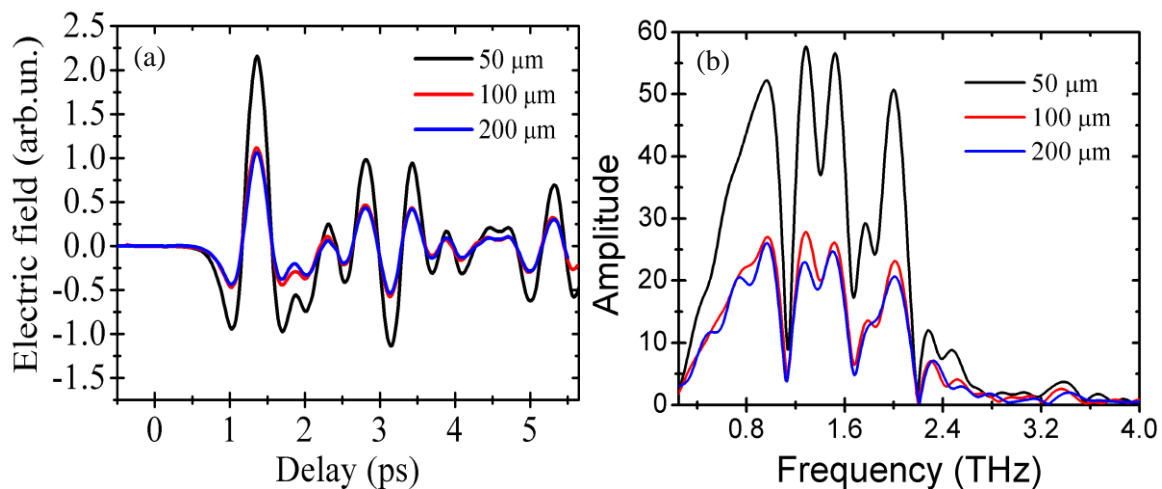


**Figure 86: (a) Measured THz electric field for three different BBO crystal thicknesses. (b) Fourier transform of the electric fields.**

The scaling-up of the yielded THz radiation as a function of the laser input pulse energy has also been investigated. As mentioned in the second chapter, for many years, misleading experiments have been conducted using electro-optic sampling technique in order to explain the THz emission mechanism. Figure 86 presents a classic example of measurement from electro-optic set-up that could be wrongly interpreted. When measuring the peak to peak value of the recorded THz electric fields, we see that the yielded THz radiation reaches saturation very fast (Figure 87(a)). On the contrary, when we measured with the broadband pyroelectric detector, for the same range of input laser energies, the THz yield grew in a linear way (Figure 87(b)).

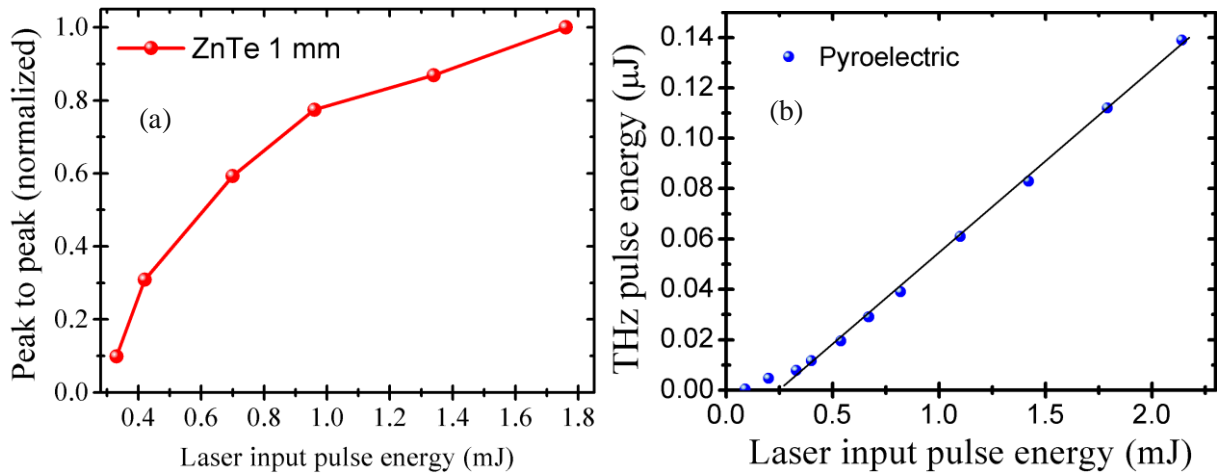


**Figure 87: (a) Peak to peak evolution of the THz electric measured in 1 mm ZnTe as function of the laser input pulse energy. (b) THz measured power as function of the laser input pulse energy.**

The saturation in the first case comes from the fact that electro-optic sampling is a polarization sensitive technique. Consequently, once the filament length increases, the polarization rotates and the electro-optic measurement imitates a saturation effect. The laser system in our laboratory presents two outputs. One at a kHz repetition rate, which has been used in all the experiments presented so far in this thesis, and another output at a 50 Hz repetition rate. The 50 Hz output has a higher level of energy, with a maximum of 35 mJ per pulse, for duration of 35 fs. Thus, we have been able to extend the measurement already presented in Figure 87(b) to higher levels of laser input pulse energy. Figure 88 presents the scale-up of the THz pulse energy using the 50 Hz laser output. The yielded THz still follows a linear increase, even for higher input laser energies. This is in good agreement with a recent publication where similar parameters have been used [42]. As one can see, we have limited our measurement to 10 mJ of laser energy. At this level of energy, the intensity reached levels close to the damage threshold of the BBO crystal. As a consequence, the BBO crystal needs to be placed a bit further from the focusing point, in order to decrease the laser intensity on its surface. Unfortunately, our BBO crystals had small apertures

(5×5 mm) which systematically led to the clipping of the laser beam, once the crystal was moved backwards. This clipping was big enough to substantially decrease the yielded THz radiation.

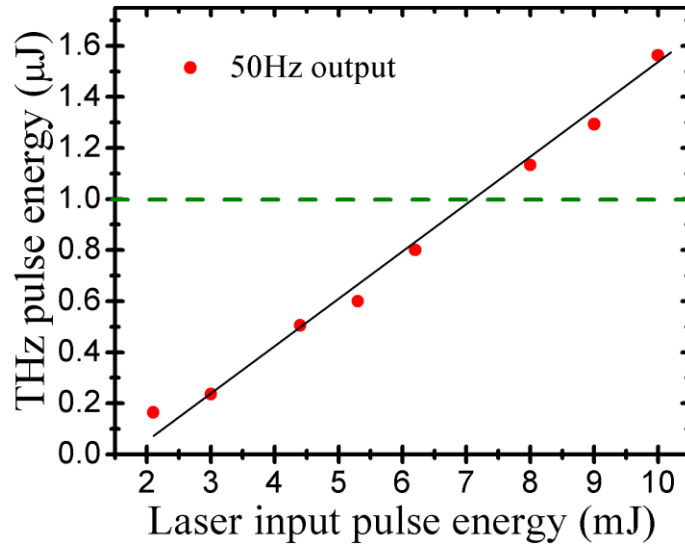


**Figure 88: Extended energy scaling, measured with pyroelectric detector.**

As presented in Figure 88, it is possible to increase the THz pulse energy further while using the 50 Hz output which may offer the possibility to yield higher level of electric fields. Thus, we have tried to obtain bigger distortions on the electro-optic signal. Our attempt using 50 Hz output has been unsuccessful in observing distortions. This may result from the fact that the laser pulse duration is not optimized once it reaches the spectrometer. Contrarily to Figure 88, where the yielded THz pulse energy was measured right at the output of the 50 Hz laser, in the case of the electric field measurement the laser pulse had to propagate over few meters in order to reach the spectrometer. Consequently, the laser pulse time duration and spectral phase can be dramatically changed along the propagation, which in turn limits the amount of yielded THz radiation. Further experiments and optimization are needed towards this objective.

## VI.5/ Chapter conclusions

In this chapter, we have shown the new opportunities offered by an intense ultrashort THz source. We have shown that the high THz electric-field level can allow the direct electro-absorption of the radiation and the resonant excitation of phonons within an intrinsic semiconductor lattice. This work may lead to the utilization of intense THz pulses for the selective excitation of specific modes. Furthermore, we have shown the diverse nonlinearities appearing during the measurement of our THz electric field. Self-phase modulation of the THz pulse within the detection crystal has been identified. Electro-optic signal distortions in thin crystals have also been observed. Finally, we have shown the possibility to obtain THz pulses with energy in the  $\mu\text{J}$  range. This shall open the way to investigate nonlinear phenomena such as Kerr self-focusing, which could in turn lead to THz beam self-localization. This level of THz pulse energy also offers the possibility to perform THz pump / THz probe experiments, which is an emerging field of research.

## References

1. A. Sell, A. Leitenstorfer, and R. Huber, "Phase-locked generation and field-resolved detection of widely tunable terahertz pulses with amplitudes exceeding 100 MV/cm," *Opt. Lett.* 33, 2767-2769 (2008).
2. J. Hebling, K. L. Yeh, M. C. Hoffmann, B. Bartal, and K. A. Nelson, "Generation of high-power terahertz pulses by tilted-pulse-front excitation and their application possibilities," *Journal of the Optical Society of America B-Optical Physics* 25, B6-B19 (2008).
3. F. Blanchard, L. Razzari, H. C. Bandulet, G. Sharma, R. Morandotti, J. C. Kieffer, T. Ozaki, M. Reid, H. F. Tiedje, H. K. Haugen, and F. A. Hegmann, "Generation of 1.5  $\mu$ J single-cycle terahertz pulses by optical rectification from a large aperture ZnTe crystal," *Opt. Express* 15, 13212-13220 (2007).
4. K. Y. Kim, A. J. Taylor, J. H. Glowina, and G. Rodriguez, "Coherent control of terahertz supercontinuum generation in ultrafast laser-gas interactions," *Nature Photonics* 2, 605-609 (2008).
5. T.-J. Wang, Y. Chen, C. Marceau, F. Theberge, M. Chateauneau, J. Dubois, and S. L. Chin, "High energy terahertz emission from two-color laser-induced filamentation in air with pump pulse duration control," *Applied Physics Letters* 95, 131108-131103 (2009).
6. P. Gaal, K. Reimann, M. Woerner, T. Elsaesser, R. Hey, and K. H. Ploog, "Nonlinear Terahertz Response of n-Type GaAs," *Phys. Rev. Lett.* 96, 187402-187404 (2006).
7. H. Wen, M. Wiczer, and A. M. Lindenberg, "Ultrafast electron cascades in semiconductors driven by intense femtosecond terahertz pulses," *Physical Review B* 78, 125203 (2008).
8. Y. Shen, T. Watanabe, D. A. Arena, C. C. Kao, J. B. Murphy, T. Y. Tsang, X. J. Wang, and G. L. Carr, "Nonlinear cross-phase modulation with intense single-cycle terahertz pulses," *Phys. Rev. Lett.* 99, 4 (2007).
9. M. C. Hoffmann, N. C. Brandt, H. Y. Hwang, K.-L. Yeh, and K. A. Nelson, "Terahertz Kerr effect," *Applied Physics Letters* 95, 231105-231103 (2009).
10. J. Chen, P. Han, and X. C. Zhang, "Terahertz-field-induced second-harmonic generation in a beta barium borate crystal and its application in terahertz detection," *Applied Physics Letters* 95, 011118-011113 (2009).
11. J. Hebling, K. L. Yeh, M. C. Hoffmann, and K. A. Nelson, "High-power THz generation, THz nonlinear optics, and THz nonlinear spectroscopy," *Ieee Journal of Selected Topics in Quantum Electronics* 14, 345-353 (2008).
12. J. R. Danielson, Y. S. Lee, J. P. Prineas, J. T. Steiner, M. Kira, and S. W. Koch, "Interaction of strong single-cycle terahertz pulses with semiconductor quantum wells," *Phys. Rev. Lett.* 99, 4 (2007).
13. A. Srivastava, R. Srivastava, J. Wang, and J. Kono, "Laser-Induced Above-Band-Gap Transparency in GaAs," *Phys. Rev. Lett.* 93, 157401 (2004).
14. K. B. Nordstrom, K. Johnsen, S. J. Allen, A. P. Jauho, B. Birnir, J. Kono, T. Noda, H. Akiyama, and H. Sakaki, "Excitonic Dynamical Franz-Keldysh Effect," *Phys. Rev. Lett.* 81, 457 (1998).
15. L. Razzari, F. H. Su, G. Sharma, F. Blanchard, A. Ayeshehshim, H. C. Bandulet, R. Morandotti, J. C. Kieffer, T. Ozaki, M. Reid, and F. A. Hegmann, "Nonlinear ultrafast modulation of the optical absorption of intense few-cycle terahertz pulses in n-doped semiconductors," *Physical Review B* 79, 193204 (2009).

16. M. C. Hoffmann, J. Hebling, H. Y. Hwang, K.-L. Yeh, and K. A. Nelson, "Impact ionization in InSb probed by terahertz pump---terahertz probe spectroscopy," *Physical Review B (Condensed Matter and Materials Physics)* 79, 161201 (2009).
17. D. R. Killelea, V. L. Campbell, N. S. Shuman, and A. L. Utz, "Bond-Selective Control of a Heterogeneously Catalyzed Reaction," *Science* 319, 790-793 (2008).
18. D. R. Killelea, V. L. Campbell, N. S. Shuman, and A. L. Utz, "Isotope-selective chemical vapor deposition via vibrational activation," *J. Phys. Chem. C* 112, 9822-9827 (2008).
19. Z. Liu, L. C. Feldman, N. H. Tolk, Z. Zhang, and P. I. Cohen, "Desorption of H from Si(111) by Resonant Excitation of the Si-H Vibrational Stretch Mode," *Science* 312, 1024-1026 (2006).
20. M. Foerst, M. Nagel, M. Awad, M. Waechter, T. Dekorsy, and H. Kurz, "Coherent and ultrafast optoelectronics in III-V semiconductor compounds," *Phys. Status Solidi B-Basic Solid State Phys.* 244, 2971-2987 (2007).
21. O. V. Misochko, "Coherent phonons and their properties," *Journal of Experimental and Theoretical Physics* 92, 246-259 (2001).
22. T. Dekorsy, G. C. Cho, and H. Kurz, "Coherent phonons in condensed media," in *Light Scattering in Solids VIII* (Springer-Verlag Berlin, Berlin, 2000), pp. 169-209.
23. R. Merlin, "Generating coherent THz phonons with light pulses," *Solid State Communications* 102, 207-220 (1997).
24. L. Dhar, J. A. Rogers, and K. A. Nelson, "Time-resolved vibrational spectroscopy in the impulsive limit," *Chem. Rev.* 94, 157-193 (1994).
25. H. J. Zeiger, J. Vidal, T. K. Cheng, E. P. Ippen, G. Dresselhaus, and M. S. Dresselhaus, "Theory for displacive excitation of coherent phonons," *Physical Review B* 45, 768-778 (1992).
26. A. Othonos, "Probing ultrafast carrier and phonon dynamics in semiconductors," *Journal of Applied Physics* 83, 1789-1830 (1998).
27. C. Thomsen, J. Strait, Z. Vardeny, H. J. Maris, J. Tauc, and J. J. Hauser, "Coherent phonon generation and detection by picosecond light-pulses," *Phys. Rev. Lett.* 53, 989-992 (1984).
28. J. M. Wiesefeld, "Acoustic phonon generation in the picosecond dynamics of dense electron-hole plasmas in InGaAsP films," *Applied Physics Letters* 47, 143-145 (1985).
29. G. C. Cho, W. Kutt, and H. Kurz, "Subpicosecond time-resolved coherent-phonon oscillations in GaAs," *Phys. Rev. Lett.* 65, 764-766 (1990).
30. D. Vonderlinde, J. Kuhl, and H. Klingenberg, "Raman-Scattering from non-equilibrium LO phonons with picosecond resolution," *Phys. Rev. Lett.* 44, 1505-1508 (1980).
31. F. Vallee and F. Bogani, "Coherent time-resolved investigation of LO-phonon dynamics in GaAs," *Physical Review B* 43, 12049-12052 (1991).
32. A. Srivastava, R. Srivastava, J. G. Wang, and J. Kono, "Laser-induced above-band-gap transparency in GaAs," *Phys. Rev. Lett.* 93, 4 (2004).
33. L. Perfetti, P. A. Loukakos, M. Lisowski, U. Bovensiepen, H. Berger, S. Biermann, P. S. Cornaglia, A. Georges, and M. Wolf, "Time evolution of the electronic structure of 1T-TaS<sub>2</sub> through the insulator-metal transition," *Phys. Rev. Lett.* 97, 4 (2006).
34. P. A. Loukakos, M. Lisowski, G. Bihlmayer, S. Blugel, M. Wolf, and U. Bovensiepen, "Dynamics of the self-energy of the Gd(0001) surface state probed by femtosecond photoemission spectroscopy," *Phys. Rev. Lett.* 98, 4 (2007).

35. G. Dolling and R. A. Cowley, "The thermodynamic and optical properties of germanium, silicon, diamond and gallium arsenide," *Proceedings of the Physical Society* 88, 463 (1966).
36. Y. P. Varshni, "Temperature dependence of the energy gap in semiconductors," *Physica* 34, 149-154 (1967).
37. G. Gallot and D. Grischkowsky, "Electro-optic detection of terahertz radiation," *J. Opt. Soc. Am. B* 16, 1204-1212 (1999).
38. Q. Wu, M. Litz, and X. C. Zhang, "Broadband detection capability of ZnTe electro-optic field detectors," *Applied Physics Letters* 68, 2924-2926 (1996).
39. G. Gallot, J. Zhang, R. W. McGowan, T.-I. Jeon, and D. Grischkowsky, "Measurements of the THz absorption and dispersion of ZnTe and their relevance to the electro-optic detection of THz radiation," *Applied Physics Letters* 74, 3450-3452 (1999).
40. R. Brazis and D. Nausewicz, "Far-infrared photon absorption by phonons in ZnTe crystals," *Optical Materials* 30, 789-791 (2008).
41. J. P. Caumes, L. Videau, C. Rouyer, and E. Freysz, "Kerr-Like Nonlinearity Induced via Terahertz Generation and the Electro-Optical Effect in Zinc Blende Crystals," *Phys. Rev. Lett.* 89, 047401 (2002).
42. G. Rodriguez and G. L. Dakovski, "Scaling behavior of ultrafast two-color terahertz generation in plasma gas targets: energy and pressure dependence," *Optics Express* 18, 15130-15143 (2010).



# *Conclusions and perspectives*

## Conclusions

The work presented in this thesis was focused on the generation and detection of coherent THz pulses, as well as their applications. The basic requirements, in order to build a THz time domain spectrometer, have been introduced. We have shown a classic example of coherent emission from optical rectification in a 500  $\mu\text{m}$  ZnTe crystal and the coherent detection with an electro-optic technique within a 1 mm ZnTe crystal. To demonstrate the advantage of time domain spectroscopy, we have shown the possibility to obtain the dielectric parameters of various known samples. Nevertheless, the results presented in chapter I have been established since a long time and did not use the full capacity of our laser system.

Consequently, we have upgraded our THz-TDS system by using a new source of THz radiation. This source, extensively described in chapter II, is based on a time-dependent macroscopic dipole-moment induced within a plasma channel in air. We have first investigated the radiation pattern emitted from a single color filament. For the first time to our knowledge, we have shown the presence of an on-axis emission. Few experimental observations let us presume of the photocurrent nature of this emission. The strength of the radiation emitted from a plasma channel can be dramatically boosted when introducing a frequency doubling crystal in the optical path prior to the filament. Our experimental data have verified the photocurrent nature of the emission, by demonstrating the direct influence of the dispersion between  $\omega$  and  $2\omega$  on the polarization of the emitted THz field [1]. While characterizing the properties of our time domain spectrometer, we have shown that it is ultra-broadband (8 THz bandwidth) with electric field reaching 200  $\text{kV}\cdot\text{cm}^{-1}$ . The 2 color filament based THz source is now well established as one of the most powerful THz table-top sources.

Due to its highly nonlinear nature, filamentation is a physical process that can be tailored by the use of external means. A detailed study on the effect that plasma tailoring has on the emission of THz pulses was presented in chapter III. The possibilities to optimize the duration of the emitted THz pulses [2], to enhance the strength of the emitted THz pulses [3] and to produce various polarization states [1] have been demonstrated. All these findings bring valuable information to the community for a better understanding of the physical mechanisms involved. Clearly, they suggest the introduction of new parameters within theoretical models in order to accurately describe the THz emission from filaments.

The last three chapters of this thesis have been devoted to the applications of this intense ultrashort THz source. In chapter IV we presented our pioneering work on the use of THz radiation within the field of art conservation [4]. Various spectroscopic data and the possibility to obtain an image of a hidden painting have been reported. The use of THz radiation for the dynamic characterization of metamaterials has been presented in chapter V [5]. Different attributes of the SRR sample linked to the variations of its conductivity or of its substrate complex index have been identified. Finally in chapter VI, the new opportunities offered by an intense ultrashort THz source have been introduced. The possibility to directly and resonantly couple THz radiation to an intrinsic semiconductor has been shown. Diverse nonlinearities which occur during the measurement of the THz radiation in an electro-optic crystal have also been reported. Finally the possibility to obtain even higher intensities was shown, with THz pulse energies reaching the  $\mu\text{J}$  level.

## Perspectives

Due to its characteristics, the 2-color filament source overcomes the other intense table-top THz sources. Indeed, in the contrary to the tilted pulse wavefront approach in  $\text{LiNbO}_3$  [6], it covers a much wider band of the spectrum. As a consequence, the pulse duration is much shorter, reaching hence higher electric field levels. The 2-color filament source can also be directly compared with the new approach of difference frequency mixing in GaSe [7]. Such source reach higher levels of electric field but is rather centered in the mid-infrared region, and not able to access the low frequency THz region (0.1 to 10 THz). Furthermore, the implementation of the technique seems rather difficult. Finally and as we demonstrated it, a direct coherent control of the THz pulse polarization is available with the 2-color filament source. This in combination with the possibility to obtain circular polarization offers a clear advantage for spectroscopic measurements.

Nevertheless, important improvements can be brought to our time domain spectrometer. Two major axes of development have been identified. First, as mentioned in chapter II, the detection technique can be considerably enhanced. A recent study has shown the possibility to detect frequencies up to 30 THz from a 2-color filament THz source [8]. The detection scheme is based on the use of a plasma channel as the detection medium. Once a THz pulse is temporally and spatially overlapped with a probing filament, a THz-field-induced-second harmonic (TFISH) is generated. Then, by applying an AC bias voltage ( $\sim 2$  kV, 500 Hz) to the probing medium, heterodyne coherent detection is possible. The measurement of the modulated second-harmonic via a photomultiplier tube (PMT), allows the direct reconstruction of the emitted THz electric field. This approach is very promising and overcomes the

electro-optic sampling technique drawbacks since no phonon modes are present within the sensing medium.

Second, the emission can be significantly enhanced if great care is taken on various parameters. As already demonstrated in chapter II, the control of the phase is a crucial point. In chapter VI, we have shown the importance of the temporal walk-off by showing the influence of the BBO crystal thickness on the emission. Another point that is of main importance concerning the increase of the THz energy is the respective laser fields' polarization. Typically, with the classic approach using a type I BBO crystal, the  $\omega$  and  $2\omega$  laser field are orthogonally polarized. A recent report as claimed a clear THz radiation enhancement when the polarization of the two laser fields is parallel [9]. This has been achieved with the use of an in-line attosecond phase controller. This optical arrangement tackles the three previously enumerated problems at the same time. A birefringent plate ( $\alpha$ -BBO) is used to compensate for the temporal walk-off between  $\omega$  and  $2\omega$ . A dual-band waveplate is placed to flip the polarization of the  $\omega$  field, leaving the  $2\omega$  field polarization unchanged. Finally, a wedge pair is used to obtain the fine control of the two fields' relative phase, with one of the wedge mounted on a step motor. Thus, an accurate control of the source is obtained and dramatic increase of the source strength can be foreseen.

Therefore, the applications of the improved THz time domain spectroscopy can also be divided in two categories. One category of applications based on the strength of the source, aiming for the observation of non-linear phenomena in various materials. Experiments of THz pump- THz probe in semiconductors could also be subject of investigations. Another field of growing interest is the application of THz radiation to biological systems. A strong and ultrafast source of THz radiation could potentially be used for inducing conformational changes in DNA or simply follow the dynamical processes occurring in living organisms. The second category of applications could take advantage of the wide band of frequency available. Various spectroscopic measurements could be done, along with the use of a cryogenic installation. Imaging applications could also be considerably improved, with an increased temporal resolution, revealing the presence of even thinner layered materials.

references

1. J.-M. Manceau, M. Massaouti, and S. Tzortzakis, "Coherent control of THz pulses polarization from femtosecond laser filaments in gases," *Opt. Express* 18, 18894-18899 (2010).
2. J. M. Manceau, A. Averchi, F. Bonaretti, D. Faccio, P. Di Trapani, A. Couairon, and S. Tzortzakis, "Terahertz pulse emission optimization from tailored femtosecond laser pulse filamentation in air," *Opt. Lett.* 34, 2165-2167 (2009).
3. J. M. Manceau, M. Massaouti, and S. Tzortzakis, "Strong terahertz emission enhancement via femtosecond laser filament concatenation in air," *Opt. Lett.* 35, 2424-2426 (2010).
4. J. M. Manceau, A. Nevin, C. Fotakis, and S. Tzortzakis, "Terahertz time domain spectroscopy for the analysis of cultural heritage related materials," *Applied Physics B-Lasers and Optics* 90, 365-368 (2008).
5. J. M. Manceau, N. H. Shen, M. Kafesaki, C. M. Soukoulis, and S. Tzortzakis, "Dynamic response of metamaterials in the terahertz regime: Blueshift tunability and broadband phase modulation," *Applied Physics Letters* 96, 021111-021113 (2010).
6. J. Hebling, K. L. Yeh, M. C. Hoffmann, B. Bartal, and K. A. Nelson, "Generation of high-power terahertz pulses by tilted-pulse-front excitation and their application possibilities," *Journal of the Optical Society of America B-Optical Physics* 25, B6-B19 (2008).
7. A. Sell, A. Leitenstorfer, and R. Huber, "Phase-locked generation and field-resolved detection of widely tunable terahertz pulses with amplitudes exceeding 100 MV/cm," *Opt. Lett.* 33, 2767-2769 (2008).
8. I. C. Ho, X. Guo, and X. C. Zhang, "Design and performance of reflective terahertz air-biased-coherent-detection for time-domain spectroscopy," *Opt. Express* 18, 2872-2883 (2010).
9. J. Dai, N. Karpowicz, and X. C. Zhang, "Coherent Polarization Control of Terahertz Waves Generated from Two-Color Laser-Induced Gas Plasma," *Phys. Rev. Lett.* 103, 023001-023004 (2009).



### List of relevant publications

1. J. M. Manceau, A. Nevin, C. Fotakis, and S. Tzortzakis, "Terahertz time domain spectroscopy for the analysis of cultural heritage related materials," *Applied Physics B-Lasers and Optics* 90, 365-368 (2008).
2. J. M. Manceau, A. Averchi, F. Bonaretti, D. Faccio, P. Di Trapani, A. Couairon, and S. Tzortzakis, "Terahertz pulse emission optimization from tailored femtosecond laser pulse filamentation in air," *Opt. Lett.* 34, 2165-2167 (2009).
3. J. M. Manceau, N. H. Shen, M. Kafesaki, C. M. Soukoulis, and S. Tzortzakis, "Dynamic response of metamaterials in the terahertz regime: Blueshift tunability and broadband phase modulation," *Applied Physics Letters* 96, 021111-021113 (2010).
4. J. M. Manceau, M. Massaouti, and S. Tzortzakis, "Strong terahertz emission enhancement via femtosecond laser filament concatenation in air," *Opt. Lett.* 35, 2424-2426 (2010).
5. J.-M. Manceau, M. Massaouti, and S. Tzortzakis, "Coherent control of THz pulses polarization from femtosecond laser filaments in gases," *Opt. Express* 18, 18894-18899 (2010).
6. J.-M. Manceau, P.A. Loukakos and S. Tzortzakis, " Direct acoustic phonons excitation by intense and ultrashort THz pulses", submitted to *Applied Physics Letters*.
7. N.-H. Shen, M. Massaouti, M. Gokkavas, J.-M. Manceau, E. Ozbay, S. Tzortzakis, M. Kafesaki, T. Koschny, and C. M. Soukoulis, "Experimental metamaterial broadband blue-shift switch in the terahertz regime with all optical implementation", under review in *NanoLetters*.

### List of conference abstracts:

J.M. Manceau and S. Tzortzakis

Invited talk "Femtosecond filamentation and THz science".

LPHYS'08, June 30 to July 4, 2008, Trondheim, Norway.

J. M. Manceau, A. Averchi, F. Bonaretti, D. Faccio, P. Di Trapani, A. Couairon, and S. Tzortzakis, Oral presentation, TOM 2, "Intense THz pulse generation from filaments in air and THz pulse shortening via plasma string tailoring"

EOS annual meeting, September 29 – October 2 2008, Paris, France

J. M. Manceau, M. Kafesaki, C. M. Soukoulis, and S. Tzortzakis

Poster presentation, TOM 2 045 1138, "Metamaterials THz resonance amplitude and position tunability by injection of photocarriers"

EOS annual meeting, September 29 – October 2 2008, Paris, France

J. M. Manceau, A. Nevin, C. Fotakis, and S. Tzortzakis,

Poster presentation, TOM 2 042 783, "Filamentation driven Terahertz time-domain-spectroscopy for the analysis of cultural heritage related materials"

EOS annual meeting, September 29 – October 2 2008, Paris, France

J.-M. Manceau, P.A. Loukakos and S. Tzortzakis

Oral presentation, IThC2, "Direct Phonon Excitation in Semiconductors by Ultrashort Intense THz Radiation"

CLEO/IQEC, May 31- June 5 2009, Baltimore, Maryland, USA

J. M. Manceau, A. Nevin, C. Fotakis, and S. Tzortzakis,

Oral presentation, AT6, Symposium S, "Filamentation driven Terahertz time-domain spectroscopy for the analysis of Cultural Heritage related materials"

EMRS Spring meeting, June 8 – 12 2009, Strasbourg, France

J.-M. Manceau, P. A. Loukakos, and S. Tzortzakis

Oral presentation "Direct Phonon excitation with intense ultrashort THz pulses".

COLA 2009, 22-27 November 2009 Singapore.

J.-M. Manceau, C. Fotakis, S. Tzortzakis

"Filamentation driven terahertz time-domain-spectroscopy for the analysis of cultural heritage related materials".

TECHNART 2009, 27 - 30 April 2009, Athens, Greece.

M. Massaouti, J.-M. Manceau and S. Tzortzakis

"Experimental metamaterial broadband blue-shift switch in the terahertz regime"

COFIL 2010, May 31- June 5 2010, Aghia Pelaghia, Crete, Greece

J. M. Manceau, M. Massaouti, and S. Tzortzakis,

"Strong terahertz emission enhancement via femtosecond laser filament concatenation in air,"

COFIL 2010, May 31- June 5 2010, Aghia Pelaghia, Crete, Greece

J.-M. Manceau, M. Massaouti, and S. Tzortzakis,

"Coherent control of THz pulses polarization from femtosecond laser filaments in gases,"

COFIL 2010, May 31- June 5 2010, Aghia Pelaghia, Crete, Greece

